Experimental Measurements and Numerical Modeling of Fast-ion Distributions in the Alcator C-Mod Tokamak

by

Aaron Craig Bader

Submitted to the Department of Nuclear Science and Engineering
in partial fulfillment of the requirements for the degree of
Doctor of Philosophy in Applied Plasma Physics
at the
MASSACHUSETTS INSTITUTE OF TECHNOLOGY
February 2012

Author .. ..
Department of Nuclear Science and Engineering
October 25, 2011

Certified by.. .....
Robert S. Granetz
Principal Research Scientist, MIT Plasma Science and Fusion Center
Thesis Supervisor

Certified by..... .....
Ronald R. Parker
Professor, Department of Nuclear Science and Engineering
Thesis Supervisor

Certified by..... .....
Ian H. Hutchinson
Professor, Department of Nuclear Science and Engineering
Thesis Reader

Certified by. .....
Paul T. Bonoli
Senior Research Scientist, MIT Plasma Science and Fusion Center
Thesis Reader

Accepted by.. .....
Mujid S. Kazimi
Chair, Department Committee on Graduate Theses

Experimental Measurements and Numerical Modeling of Fast-ion Distributions in the Alcator C-Mod Tokamak

by

Aaron Craig Bader

Submitted to the Department of Nuclear Science and Engineering
on October 25, 2011, in partial fulfillment of the
requirements for the degree of
Doctor of Philosophy in Applied Plasma Physics

Abstract

In this thesis we discuss measurements and modeling of minority heated fast-ion distributions in the Ion Cyclotron Range of Frequencies (ICRF) on the Alcator C-Mod tokamak. Analysis of fast-ions $>100T_e$ is important for both ITER and a future fusion reactor as both will have a significant population of 3.5 MeV alpha particles generated in fusion reactions. Fast particles in this energy range can drive unstable modes such as Toroidal Alfvén Eigenmodes (TAEs) and Reversed Shear Alfvén Eigenmodes (RSAEs). Furthermore, energetic ions may display plasma properties that differ from the bulk plasma. It is crucial to benchmark current simulation codes with measurements from highly energetic fast-ions on current devices. This thesis will focus on measurements of the fast-ion distribution made on C-Mod with an upgraded Compact Neutral Particle Analyzer (CNPA). Measurements of the fast-ion distributions will reveal strong dependences of the fast-ion effective temperature on both electron density and plasma current. For further analysis, we use the simulated distributions generated by the coupled full-wave spectral solver AORSA, with the zero orbit-width bounce-averaged Fokker-Planck code CQL3D. A new synthetic diagnostic integrated into CQL3D is used to make direct comparisons with the CNPA. We find that for plasmas that have a steady-state fast-ion distribution ($df/dt = 0$) the simulation and the experiment have good agreement. However, in simulations where the fast-ion distribution is evolving in time ($df/dt \neq 0$) we find a discrepancy between the simulation and the experimental results. The simulation is seen to evolve much slower than the experiment. Various reasons for the discrepancy are explored, including the possibility of a violation of the quasi-linear theory used in CQL3D.

Thesis Supervisor: Robert S. Granetz
Title: Principal Research Scientist, MIT Plasma Science and Fusion Center

Thesis Supervisor: Ronald R. Parker
Title: Professor, Department of Nuclear Science and Engineering

Thesis Reader: Ian H. Hutchinson
Title: Professor, Department of Nuclear Science and Engineering

Thesis Reader: Paul T. Bonoli
Title: Senior Research Scientist, MIT Plasma Science and Fusion Center

Acknowledgments

The number of personages that has contributed to the completion of my doctoral thesis are far too numerous to name in full, but I will attempt anyway.

First, I'd like to thank my friends and family who have provided support during my thesis research. Thank you Mom and Dad and thank you Scott, Joseph and Rachel and your menagerie of children. Also, thanks goes to floor 4E of the East Campus dormitary, who provided me with a home for the bulk of my graduate career. Living with you guys was a great experience and one that I will remember fondly.

I also wish to acknowledge my fellow graduate students who have suffered alongside me through the trials and tribulations of MIT, and have mostly tolerated my company. In a particular order, thank you Harold Barnard for abiding my presence in our office, Brock Bose for what's it called; Michael Churchill for not destroying Austria; Antoine Cerfon, merci; Arturo Dominguez, gracias por su cabello fabuloso; Nathan Howard for not graduating before me; Noam Katz, todah rabba; Ko Jinseok, kamsa hamnida; Ken Marr for advice on women no sane person would ever take and for proofreading assistances; Roman Ochoukov for being impervious to distraction; Yuri Podpaly for enduring my company even outside the lab; Jason Sears for possessing actual electronics expertise; Matt Reinke for never turning off the plasma-physics part of his brain; Andrea Schmidt for distracting other scientists with cute kids; Noah Smick for disposing of all my (un)desired food; Kelly Smith for tolerating my impudence; Vincent Tang for getting me up to speed on the CNPA; Naoto Tsujii for testing my hearing; and Greg Wallace for always knowing the answer, sometimes even the correct one. Thanks as well to Alex Boxer, Igor Bespamyatnov, Dan Brunner, Istvan Cziegler, Eric Edlund, Paul Ennever, Ian Faust, Marco Ferrara, Will Fox, Mike Garrett, Christian Haakonsen, Zach Hartwig, Alex Ince-Cushman, Flopper Lamantin, Cornwall Lau, Ken Liao, Liang Lin, John Liptac, Yunxing Ma, Rachael Mcdermott, Orso Meneghini, Bob Mumgaard, Geoff Olynyk, Alex Parisot, Leonardo Pattacchini, Peng Xu and Kirill Zhurovich.

Thank you Jessica Coco, Corinne Fogg and the entire C-Mod and PSFC administrative team. Without you, we would all be paralyzed by inscrutable forms and procedures. Thank you Gary Dekow, Rui Vieira and the C-Mod engineers for keeping everything running smoothly. Thank you Ed Fitzgerald, Mark Ivey and the C-Mod machinists. Without your help and advice, the CNPA would only exist as a dream in a scientist's mind. Thank you Tom Toland, Ron Rosati and the C-Mod vacuum team for immeasurable assistance. Without your help, the CNPA would be sitting on a shelf shrouded in dust. Thank you Josh Stillerman, Tom Friedman, Brandon Savage and the C-Mod computing team for all your aid with data management and digitization woes. Thank you Bill Parkin, Maria Silviera and the electronics shop for all your help with the C-Mod electronics and power supplies.

Thank you to all the C-Mod scientists who make the Alcator project a veritable forum where the currency is ideas. Thank you Amanda Hubbard, Jerry Hughes, Jim Irby, Brian LaBombard, Yijun Lin, Bruce Lipschultz, Earl Marmar, Miklos Porkolab, Abhay Ram, John Rice, Bill Rowan, Steve Scott, Joseph Snipes, Jim Terry and Graham Wright. An additional thanks to the Nuclear Science and Engineering Faculty, Jeff Freidberg, Anne White and Dennis Whyte. Special thanks to Ian Hutchinson for being a thesis reader, and for your valuable critiques. Thank you to the RF-SCIDAC group who have assisted me in getting familiar with the computation codes. Thank you Lee Berry, Don Batchelor, Fred Jaeger, Bob Harvey and John Wright.

Lastly, I'd like to thank Robert Granetz, my supervisor. It has been a pleasure to work with you for these years. I'd like to thank Paul Bonoli, who's input and assistance has been invaluable. I would not have been able to progress as far as I have on simulations and theory without your advice and encouragement. And I'd like to thank Ronald Parker who has assisted both in the lab and in academics. It's been an enlightening experience to work with you both in research and in the classroom.

Contents

List of Figures

List of Tables

Chapter 1

Introduction

In 1946, Sir George Paget Thomson and Moses Blackman of Britain patented a design for a fusion reactor. Patent GB817681 includes many features recognizable on fusion experiments today. Among these features are a toroidal chamber, a strong toroidal guide field, a toroidal plasma current, a deuterium gas species and auxiliary heating by electromagnetic waves. At the time of the patent, fusion research was classified, both in the United States and abroad, and research was pursued by various countries independently. Fusion research and development remained independent until 1958, when a worldwide agreement would declassify all magnetic confinement fusion energy research. Thomson and Blackman's patent, along with parallel research in the United States, the Soviet Union and various other countries would be released to the public shortly after. Fusion energy became a scientific research project with collaborators around the entire world and remains so today [1].

In Thomson and Blackman's patent, they recognized the need to reach a very high temperature in a plasma in order to produce a sustained fusion reaction. Their chosen method for achieving this temperature was to heat the plasma with electromagnetic waves. This thesis will discuss one of the methods of heating by electromagnetic waves, Ion Cyclotron Resonance Heating (ICRH). In more detail, it will examine the resulting distribution of heated ions using both new detection diagnostics on the

Alcator C-Mod tokamak, and with advanced simulation techniques. A main focus of this thesis is the benchmarking and validation of current simulation techniques with experimental results.

The layout of this thesis is as follows. The remainder of this chapter describes the Tokamak reactor concept and some of the basic plasma physics properties that are relevant to the thesis. Chapter 2 discusses the Compact Neutral Particle Analyzer (CNPA) diagnostic used to make measurements of fast-ions heated by ICRH. This chapter also includes a description of previously built, similar diagnostics both on C-Mod and on other tokamaks. Chapter 3 describes experimental results and the analysis routines used to interpret them. Among the results, we find that the fast-ion distribution has a strong dependence on plasma current, and this encourages simulation focus on this area. Chapter 4 introduces AORSA and CQL3D, two plasma simulation codes, and a new synthetic diagnostic that allows for direct comparison between these codes and experimental measurements. The second half of Chapter 4 discusses simulations of steady-state, $df/dt = 0$, fast-ion distributions with comparisons to experimental results. We find good agreement between simulation and experiment for plasma currents ranging from 0.6 MA to 1.2 MA, indicating that the simulation codes can correctly predict the fast-ion distribution function for steady-state minority-heated plasmas. Chapter 5 discusses time-dependent simulations which focus on the evolution of the fast-ion distribution during the periods of time immediately after the ICRF heating turns on and turns off. The time-dependent results reveal a discrepancy between simulation and experiment and the reasons for the discrepancy are explored. One of the possible reasons for the discrepancy is a violation of quasi-linear theory, and there is some supporting evidence, both from analytic theory and from improved simulation techniques. Chapter 6 discusses the conclusions of the research and points to future paths that are fertile ground for further inquiry.

This is not the first attempt at measuring the fast-ion distribution with a CNPA or comparing the results with AORSA-CQL3D simulations [2]. However it is the first

Table 1.1: Physical parameters of tokamaks worldwide. Starred entries have yet to be built[3, 4, 5, 6, 7, 8, 9].

Name	Location	Years of Operation	Maj. Rad (m)	Min. Rad (m)
Alcator C-Mod	MA, USA	1991 - pres.	0.67	0.22
Alcator C	MA, USA	1978 - 1986	0.64	0.16
Alcator A	MA, USA	1972 - 1978	0.54	0.10
DIII-D	CA, USA	1986 - pres	1.66	0.67
NSTX	NJ, USA	1999 - pres	0.85	0.67
TFTR	NJ, USA	1982-1997	2.4	0.8
PLT	NJ, USA	1975-1986	1.32	0.4
JET	England	2000-pres	2.96	1.0
ASDEX-U	Germany	1991-pres	1.65	0.5
Tore Supra	France	1988-pres	2.25	0.7
JT-60 U	Japan	1990-pres	3.4	1.0
ITER*	France	2020-??	8.14	2.8
ARIES-AT*	??	??	5.2	1.3

time that fast-ion data has been obtained over a large ensemble of plasma discharges. It is also the first time that comparisons with simulations have been made over a range of plasma currents and at energies > 350 keV. The thesis compares the absolute value of the neutral flux to a synthetic diagnostic, which has not been attempted with any minority-heated plasma. Lastly, this thesis outlines the initial attempt to simulate a time-evolving discharge, and indicates that there are discrepancies with the simulation in plasmas with evolving fast-ion distributions.

1.1 Tokamaks

The first tokamak was built in 1956 by Russian scientists at the Kurchatov Institute in Moscow. The word 'tokamak' is a Russian acronym that loosely translates to toroidal chamber with a magnetic field. Since then, the tokamak has been the most successful controlled fusion device and many tokamaks can be found around the world (see Tables 1.1 and 1.2). Tokamaks use strong magnetic fields to confine hot plasmas. There

Table 1.2: Operating parameters of tokamaks worldwide. Starred entries have yet to built [10, 4, 5, 6, 7, 11, 9].

Name	TF (T)	I_p (MA)	n_e ($\times 10^{20} m^3$)	T_e (keV)	Pulse Length
Alcator C-Mod	≤ 8	0.4-2	1-2	1-8	2
Alcator C	≤ 14	≤ 0.5	≤ 7	2	0.4
Alcator A	≤ 10	≤ 0.2	≤ 5	1	0.2
DIII-D	2.1	3	$\leq$1.0	$\sim$10	10
NSTX	0.3	1	0.6	2	0.9
TFTR	6	3	$\sim$0.5	12	2-3
PLT	4	0.5	$\sim$0.5	$\sim$2	1
JET	3.8	$\leq$7	0.7	10	$\sim$20
ASDEX-U	3.1	1.2	$\sim$1.0	$\sim$5	$\sim$7
Tore Supra	4.5	1.7	≤ 0.5	$\sim$5	330
JT-60 U	4.5	5	0.5	$\sim$12	$\sim$10
ITER*	5.7	27	$\sim$1	$\sim$10	1000
ARIES-AT*	5.8	13	2.15	18	months

are three main magnetic fields in the tokamak, and these are shown in Figure 1-1. The dominant field is toroidal (long way around the torus) and is created by conducting coils wrapped around the vacuum chamber. This field alone is insufficient for charged particle confinement. In addition to the strong toroidal field, a considerably weaker poloidal field (short way around the torus) is necessary. Unfortunately, creating this field is more difficult. A conducting loop through the center of the plasma would create a suitable field, but the plasma will melt any loop placed there. Therefore, it is necessary to use the plasma's conductivity itself to create the poloidal field. To drive a toroidal plasma current, tokamaks use a strong central solenoid that passes through the hole in the middle of the torus. By increasing the current through this coil, an electric field is created in the plasma in the toroidal direction in accordance to Faraday's Law. The plasma is an excellent conductor of electricity and a current is driven in response to this electric field. An additional benefit is that the plasma is also heated through the same process. The downside of using a central coil is that driving current in the plasma requires a continual increase of current in the central

solenoid. Because this cannot happen indefinitely, it limits the amount of time a plasma can be sustained. Alternative methods of driving current with RF waves or neutral beams is a heavily researched topic on present-day devices.

Other coils situated about the machine provide lesser fields for various stability and plasma shaping concerns. The most important of these is a vertical field, usually created by toroidal loops on the top and bottom of the vessel. The vertical field is required for plasma equilibrium. Additional coils are often used to provide feedback control and correct for slight alignment errors in the main coils.

Tokamaks are axisymmetric by design. This means that there is negligible variation in the toroidal direction. Axisymmetry simplifies plasma diagnosis because measurements taken at one toroidal location of the tokamak can be assumed to be valid at any other toroidal location.

1.1.1 Single particle motion

Characterizing the motion of charged particles in the magnetic fields of the tokamak is essential for many of the concepts discussed in this thesis. The relevant physics of charged particle motion will be discussed in this section.

Charged particles feel a force perpendicular to both their direction of motion and the magnetic field lines,

$$\vec{F} = q\vec{v} \times \vec{B}. \tag{1.1}$$

Here, q is the particle charge, $\vec{v}$ is the particle velocity and $\vec{B}$ is the magnetic field. Therefore, in a constant magnetic field, a charged particle feels no force in the direction of the magnetic field, but exhibits circular motion perpendicular to the field. Thus, the total particle motion is helical. The motion of a single particle about a magnetic field line can be calculated by setting the LHS of Eq. 1.1 to $md\vec{v}/dt$ and solving the differential equation. The result gives unconstrained motion along the field line and circular motion perpendicular to the field line with frequency and radius given

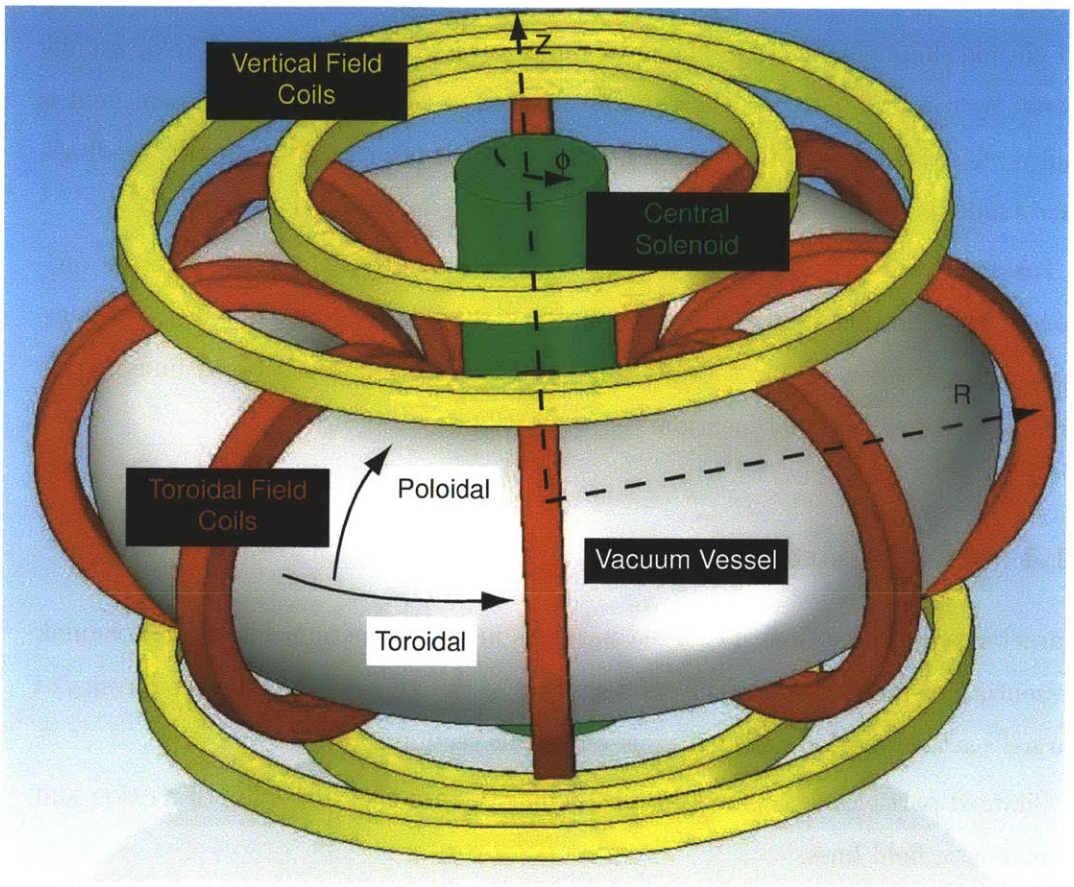

Figure 1-1: A toroidal vacuum vessel is shown along with the standard tokamak magnetic coils. A vacuum vessel with a cylindrical cross-section is chosen for simplicity. The toroidal field coils are shown in red, the central solenoid is green, and the vertical field coils are yellow. Also shown is the standard coordinate system used in this thesis with the R, Z, and ϕ axes.

by,

$$\omega_c = 2\pi f_c = \frac{qB}{m};\ \rho_L = \frac{v_\perp}{\omega_c}. \tag{1.2}$$

Here f_c is the cyclotron frequency, ρ_L is the radius of the circular motion (the Larmor radius). $v_\perp$ is the perpendicular velocity of the particle, B is the magnetic field strength and m is the particle mass. Note that because q is signed, the electrons and the ions will gyrate around the field in opposite directions.

To zeroth order a particle will trace out a helical orbit along a field line. However, if we account for the presence of electrical fields, field line curvature or changes in magnetic field strength, the particle will drift off the field lines. For a torus with a circular cross-section the particle motion can be described analytically. However, for more complicated magnetic field topologies, the calculations need to be done numerically.

Motion in a field of changing strength

A particle in a plasma may undergo collisions with other particles or may lose energy to radiative emission of photons. However, first we will consider particle orbits in the absence of these two energy loss mechanisms, i.e. orbits of particles that conserve total kinetic energy. Another constant of motion is the first adiabatic invariant,

$$\mu = \frac{mv_\perp^2}{2B} = \text{const}, \tag{1.3}$$

which is constant if the gradient length of the magnetic field is large compared to the particle's Larmor radius. From Equation 1.3, we infer that if a charged particle is moving into a region of increasing field strength, the velocity perpendicular to the magnetic field, $v_\perp$ must also increase. Since the total particle energy is conserved, the velocity along the field line $v_\parallel$ decreases. It is possible that $v_\parallel$ reaches 0, at which point the ion will reflect and begin traveling in the opposite direction. This is the magnetic mirror effect. For a given field gradient, the point of reflection is determined

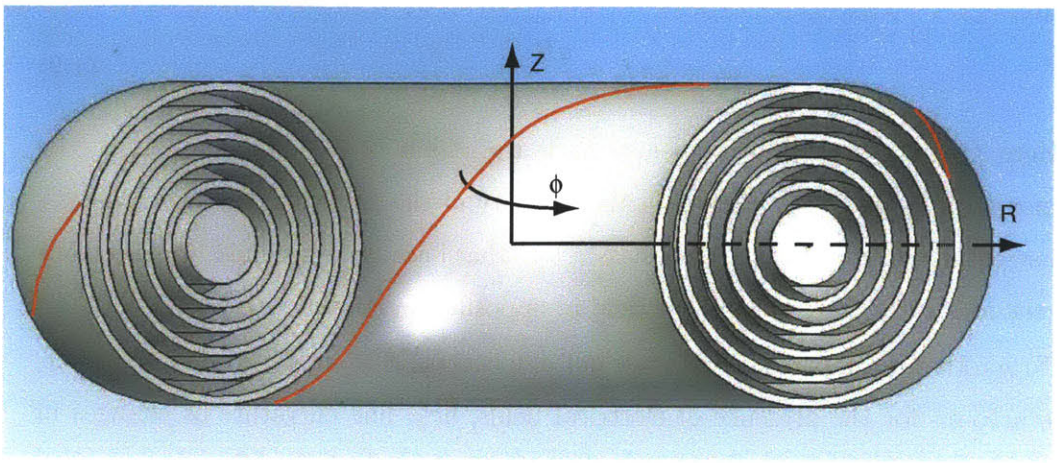

Figure 1-2: In this plot, several flux surfaces of a plasma with a cylindrical cross-section are shown. The red line on the outermost flux surface represents an arbitrary magnetic field line. Also shown is the standard coordinate system used in this thesis with the R, Z, and ϕ axes.

by the pitch-angle, $\vartheta = v_{\|}/v$. Particles with low values of ϑ will be reflected with only a small gradient in magnetic field strength.

1.1.2 Magnetic fields in a tokamak

If a field line is followed around the tokamak, it will trace out a 'flux surface' (see Figure 1-2). To zeroth order, particles are confined to flux surfaces. Therefore, flux surfaces delineate natural boundaries in the plasma. Often a measurement made in the plasma at a specific location can be generalized to any location on the same flux surface. This is an improvement on axisymmetry, and allows measurements taken along a single radial chord to determine some plasma properties throughout the entire plasma. However, plasma properties display more variation in the poloidal direction than they do in the toroidal direction, and we note that some properties, such as magnetic field strength, are not the same over the entire flux surface.

A note on coordinate systems

Before describing how the magnetic fields inside the plasma are determined, it is important to describe the coordinate systems that we will use both now and for the rest of the thesis. As shown in Figures 1-1 and 1-2, the general cylindrical system can be used to describe the tokamak geometry. However, this geometry is inconvenient for many calculations. Often a pseudo-toroidal system is used instead, and both systems are used interchangeably in this thesis.

Figure 1-3 shows both the pseudo-toroidal coordinate system and the cylindrical coordinate system. The coordinate systems are shown overlaid on a cross-section of the plasma. The flux surfaces are shown in blue. Magnetic lines in this region lie on closed flux surfaces. The last closed flux surface is shown in red. Outside this flux surface, all magnetic field lines terminate on a vessel wall. The radial coordinate r represents the distance from the magnetic axis of the plasma and the poloidal angle θ represents the angle from the outboard midplane. Often, the coordinate r is not as useful as the normalized radial coordinate $\rho = r/a$, where a is the distance between the magnetic axis and the last closed flux surface on the outboard midplane.

Magnetic field calculations

It is difficult to get actual measurements of the magnetic fields in the plasma. However, these magnetic fields are absolutely vital for both tokamak operation and analysis. Not only do they determine the flux surfaces used for applying diagnostic measurements throughout the plasma, it is impossible to control a plasma without knowledge of its shape. Instead of direct measurements inside the plasma core, measurements are taken at the edge of the plasma and are used as boundary conditions for the Grad - Shafronov equation which governs magnetic field topology [12].

$$R\frac{\partial}{\partial R}\left(\frac{1}{R}\frac{\partial \psi}{\partial R}\right) + \frac{\partial^2 \psi}{\partial z^2} = -\mu_0 R^2 \frac{dp}{d\psi} - F\frac{dF}{d\psi}, \tag{1.4}$$

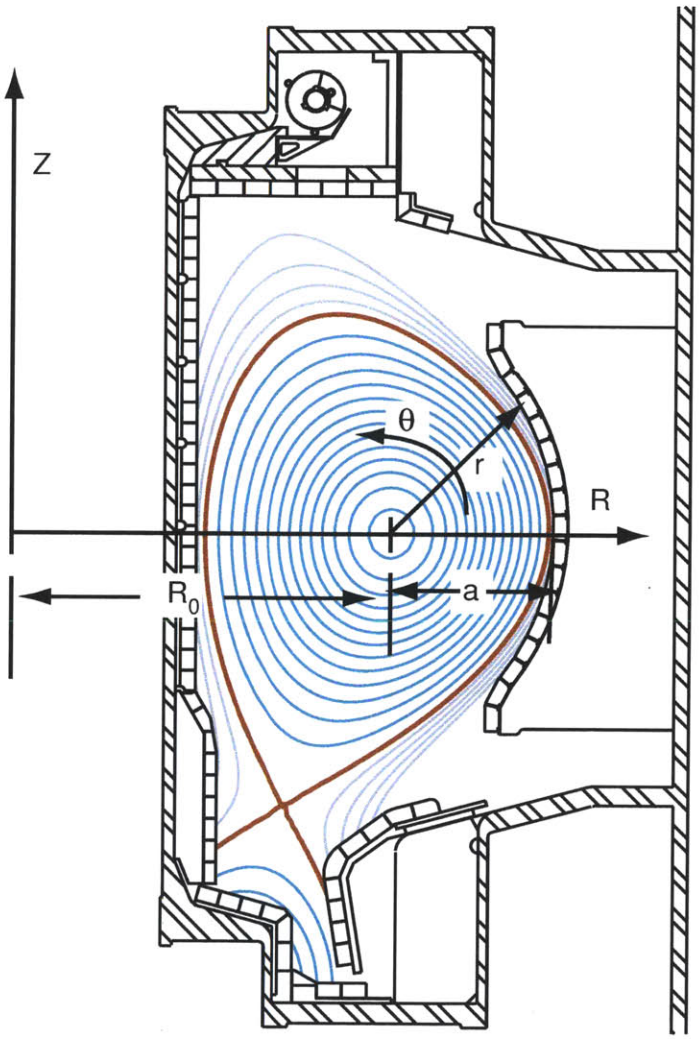

Figure 1-3: Shown are the various coordinate systems used in this thesis overlaid over a poloidal cross-section of the plasma.

where

$$\vec{B} = \frac{1}{R}\nabla\psi \times \hat{\phi} + \frac{F}{R}\hat{\phi},$$

$$\mu_0 \vec{J} = \frac{1}{R}\frac{dF}{d\psi}\nabla\psi \times \hat{\phi} - \frac{1}{R}\frac{\partial}{\partial R}\left(\frac{1}{R}\frac{\partial\psi}{\partial R}\right)\hat{\phi} + \frac{\partial^2\psi}{\partial z^2}\hat{\phi}.$$

Here, a cylindrical coordinate system is used (see Figure 1-2) and ψ represents the magnetic flux that passes through a surface,

$$\psi = \int \vec{B} \cdot \vec{n} dS.$$

The relationship between ψ and the magnetic fields are given by,

$$B_R = -\frac{1}{R}\frac{\partial\psi}{\partial z},$$

$$B_z = \frac{1}{R}\frac{\partial\psi}{\partial R}.$$

In order to determine the plasma equilibrium, we use boundary conditions imposed by measurements to place conditions on the free functions $p(\psi)$ and $F(\psi)$. These boundary conditions alone are insufficient and additional conditions are necessary to uniquely specify an equilibrium [13].

1.1.3 Trapped and passing particles

The toroidal magnetic field strength in vacuum can be calculated from Ampere's Law by considering a circular path at radius R:

$$\mu_0 I_{\mathrm{TF}} = 2\pi R B_\phi;\ \mathrm{B}_\phi \propto \frac{1}{R}. \tag{1.5}$$

Here, I_{TF} is the current that passes through all the toroidal field coils. Thus the toroidal field strength varies inversely with major radius and is stronger on the inside of the torus than on the outside. For normal field configurations, a particle will

experience the lowest magnetic field where the orbit intersects the outboard midplane. At this point $v_{\|}$ is maximal. For this reason, it is convenient to express particle orbits in terms of the pitch angle at the outboard midplane, $\vartheta_0 = \sin(v_{\|,0}/v)$, where 0 subscripts denote that the value is taken at the outboard midplane.

There are two classes of particle orbits in a tokamak magnetic field, trapped orbits and passing orbits. Trapped particles have a low ϑ_0 and reach a point along their orbit where $v_{\|} = 0$ causing them to be reflected by the magnetic mirror. Passing particles never reach a point where $v_{\|} = 0$ and thus do not get reflected. Figure 1-4 shows various trapped particle orbits projected onto a single poloidal plane. Because of their shape, these particle orbits are called 'banana' orbits.

The radial difference between the inner location and the outer location of a banana orbit at the midplane is the 'banana width'. The banana width varies inversely with current, and is given by [5],

$$\Delta_b = \frac{v_{\|,0}}{\omega_{c,\theta}};\ \omega_{c,\theta} = \frac{qB_\theta}{m}. \tag{1.6}$$

Here, $v_{\|,0}$ represents the parallel velocity at the outboard midplane. $\omega_{c,\theta}$ represents the poloidal cyclotron frequency, the frequency of gyration about the poloidal magnetic field. The integrated poloidal field can be obtained from Ampere's law integrated around a flux surface,

$$\oint B_\theta ds = -\mu_0 \int_{FS} J_\phi dA.$$

The areal integral determines the total toroidal current contained by the flux surface and the surface integral gives the integrated poloidal field. Most importantly for this thesis, Equation 1.1.3 shows that the banana width scales proportionally to the parallel velocity and inversely with plasma current,

$$\Delta_b \propto \frac{v_{\|}}{I_p}. \tag{1.7}$$

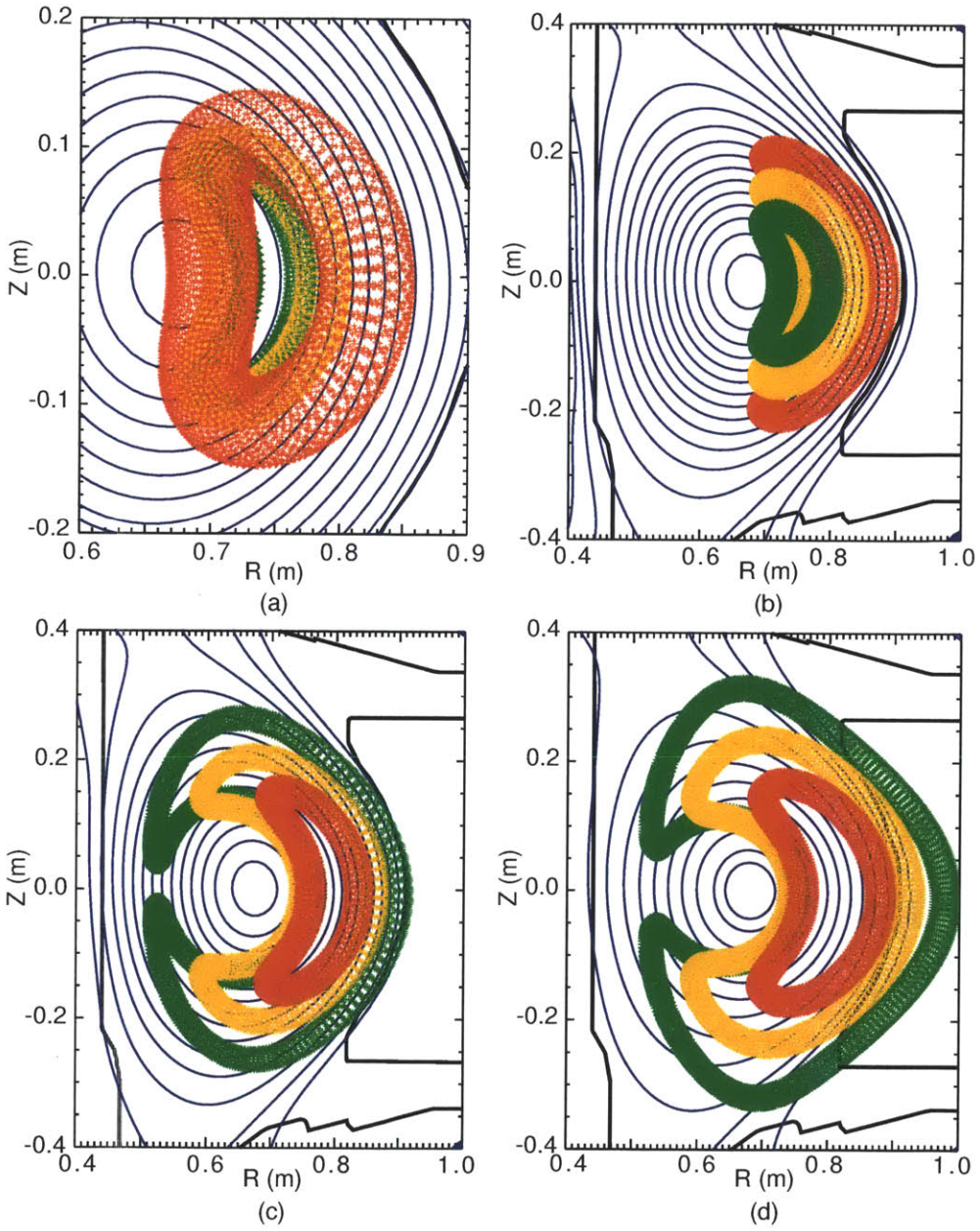

Figure 1-4: Orbits for trapped protons with various initial conditions are shown. (a) shows 300 keV (green) 1 MeV (yellow) and 3 MeV (red) ions with banana tips at the same location. (b) shows 1 MeV ions with banana tips at the same R location but different z locations. (c) shows 1 MeV ions with banana tips on the same flux surface but with different $v_{\|}/v_{\perp}$ ratios. (a), (b) and (c) are all for 1 MA plasmas. (d) shows the same ions as in plot (c) but in a 600 kA plasma.

Figure 1-4 shows various banana orbits calculated for plasmas on the Alcator C-Mod tokamak. Plots (c) and (d) show the effects of parallel velocity and plasma current on banana orbit width. Several of these orbits intersect the plasma limiter. Any particle with an orbit that intersects a vessel component is unconfined. From these figures it is shown that highly energetic, barely trapped particles in plasmas with low plasma currents are least likely to be confined.

1.2 Alcator C-Mod

The experimental work presented in this thesis was carried out on the Alcator C-Mod tokamak. Alcator is an acronym for Alto Campo Torus or "High Field Torus", and the Alcator project studies high magnetic field, high density, compact tokamaks. C-Mod is the third tokamak in the Alcator family and is larger, hotter, has similar high plasma density and lower magnetic field than its predecessors (see Tables 1.2 and 1.1). This section will describe in more detail the geometry and operating regime of C-Mod.

1.2.1 C-Mod vessel and geometry

Alcator C-Mod has a major radius of 67 cm and a minor radius of 22 cm. Plasmas do not have circular cross-sections but are elongated vertically and shaped triangularity. Alcator plasmas can run with elongation values, $\kappa = b/a$, of up to 1.8 [14], where b represents the distance from the center to the vertical plasma edge, and a represents the distance from the center to the horizontal edge. Typical plasma shapes can be seen in Figures 1-3 and 1-4.

C-Mod can run both limited and diverted plasmas. A limited plasma is one where the last closed flux surface (LCFS) has a field line that intersects a vessel surface. A diverted plasma is one where there is an 'x-point,' where the poloidal magnetic field is zero. The LCFS field lines pass through the x-point and intersect a vessel structure,

called a divertor specially designed to handle the incident heat load. For example, the plasma in Figure 1-3 is a Lower Single Null (LSN) plasmas, where the x-point is at the bottom of the plasma. Upper Single Null and Double Null plasmas are also often made in C-Mod. Figure 1-4 includes cross-sections for Upper Single Null plasmas.

C-Mod has 10 horizontal ports and 20 vertical ports (see Figure 1-5. Each port is lettered from A-K (skipping I). Each horizontal port is ~20 cm wide and ~60 cm tall. Of the 10 horizontal ports, 3 are devoted to ICRF heating (see Section 1.3), one is devoted to Lower Hybrid Current Drive, one is occupied by Thomson Scattering (see Section 2.3) and one is devoted to the Diagnostic Neutral Beam. This leaves 4 horizontal ports for various other diagnostics.

The 20 vertical ports are distributed evenly between the top and the bottom of the machine. These ports are all teardrop shaped, ~ 20 cm long and ~8 cm wide at their widest point. The port's access point is located far away from the plasma midplane. The distance between the upper or lower divertor and the end of the vertical port is ~1.5 m. Some of the lower ports are 'closed', i.e. they are covered by a divertor plate. These closed ports are mainly used to bring cables and fibers out of the vessel. The remaining bottom ports allow a line of sight to the plasma from below the vacuum vessel. The upper ports all have a line of sight to the plasma, although most of them are partially occluded due to the presence of the cryopump. Details of the vertical ports that are important to this thesis are discussed in more detail in Section 2.2.3

Outside the vacuum vessel are the 20 copper toroidal field bundles, each with 6 turns. These are held into place by a steel cylinder with 66 cm thick plates on the top and the bottom. The entire structure is housed in a cryogenic shell that keeps the magnets at liquid nitrogen temperature. Beyond the shell is a concrete shield to block the escape of neutrons from fusion reactions. The total vertical height of the machine, including the concrete shell is 6.63 m and the total diameter is 4.9 m.

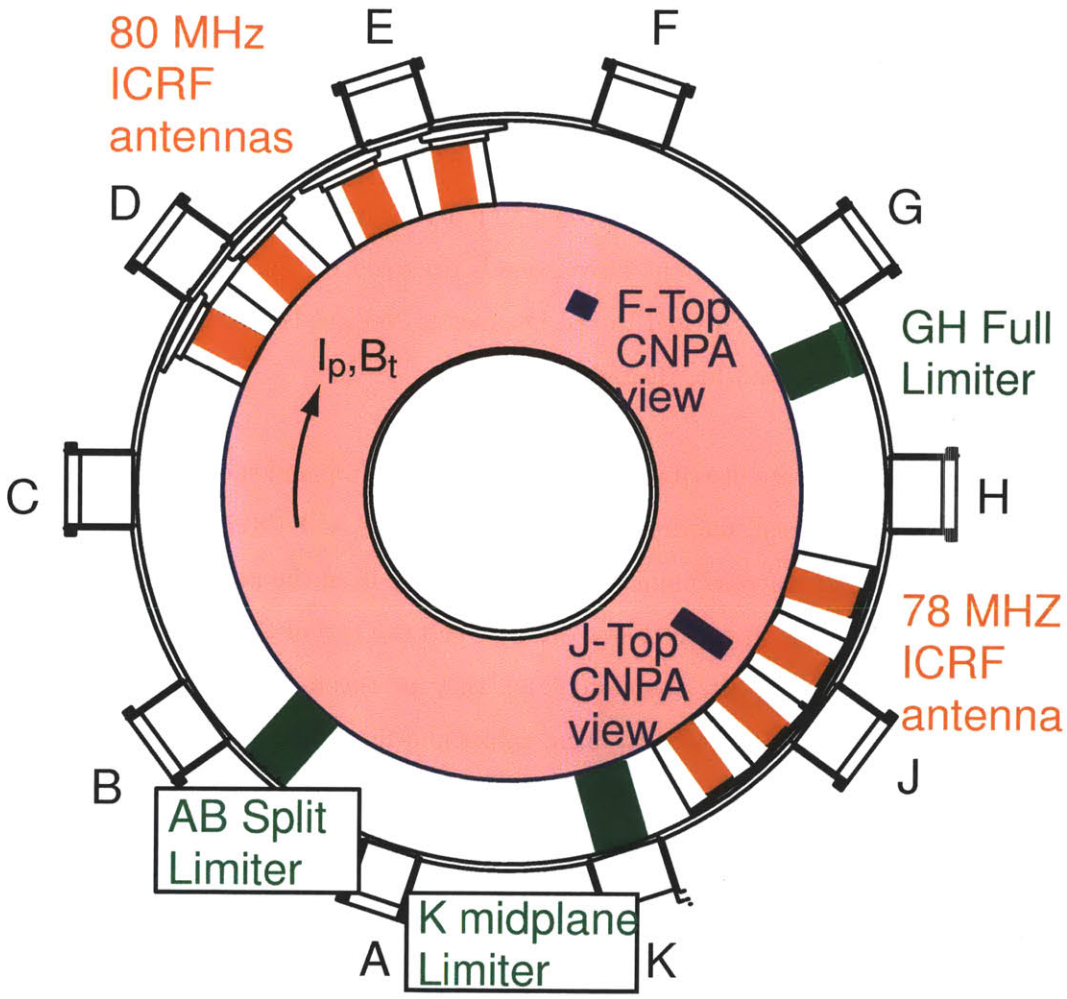

Figure 1-5: Schematic of top view of Alcator C-Mod tokamak showing the locations of the 10 horizontal ports, the RF antennas, the plasma limiters and the location viewable with the Compact Neutral Particle Analyzer.

1.2.2 Operating parameters of Alcator C-Mod

As mentioned before, C-Mod is designed to be a high density, high field, compact tokamak. The central toroidal field can reach 8 T. However, for the majority of the discharges studied in this thesis, toroidal fields between 5 and 6 T are used.

Plasma current in C-Mod also has a wide range of operation. Typical operating plasma current is between 800 kA and 1 MA. However, operating up to 2.0 MA or as low as 400 kA is also possible. The plasma current on C-Mod is mainly driven inductively through the central solenoid. Lower hybrid driven current is also a possibility, although most of the discharges in this thesis do not have Lower Hybrid Current Drive present.

C-Mod mainly operates with deuterons as the dominant plasma ions. Plasmas are generally 90-95% deuterons with the remainder consisting of various impurity species. Of the impurity species, the dominant ones are hydrogen (5-10 %) and boron ($\sim$1 %). Other impurities are present in trace quantities. These include molybdenum, nitrogen, oxygen, argon and tungsten. C-Mod sometimes operates with bulk helium plasmas, and there are experiments where He^3 is injected as a impurity to be heated by ICRF waves. The thesis will on deuterium majority plasmas with a hydrogen minority and with boron as the other dominant impurity.

Electron temperatures in ICRF heated plasmas are between 3-5 keV. Throughout this thesis, we will assume $T_i = 0.8T_e$, although relaxing this assumption has negligible effect on the analysis.

C-Mod's pulse length is limited by heating in its toroidal field magnets and the flux swing of the central solenoid. The total plasma pulse length is typically 2 s at normal field strength (5.4 T). The first 500 ms are devoted to ramping up the plasma current. Similarly, the last 500 ms are devoted to ramping down the current. As such, there is a 1 s long flattop region over which plasma parameters can be maintained at a constant level.

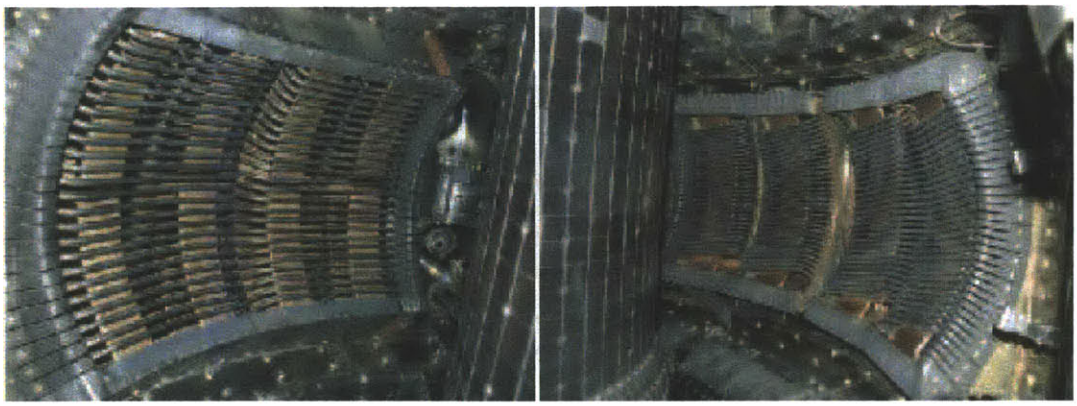

Figure 1-6: View of the ICRF antennas on Alcator. The 2, 2-strap antennas on D-port and E-port are on the left and the 4-strap antennas at J-port is on the right.

1.3 ICRF heating

C-Mod uses ICRF (Ion Cyclotron Range of Frequencies) for its bulk auxiliary heating. A derivation of the wave dispersion relation has been included in Appendix A. This section will describe the physical antenna setup and the results of the fast-ion heating. C-Mod has 3 ICRF antennas located in D, E and J-ports. The D and E antennas have two straps each and the J antenna has 4 straps. The system is capable of supplying 6 MW of power into the plasma. Nominal operating frequencies are 78 MHz for J, 80 MHz for E and 80.5 MHz for D, although it is possible to alter the J antenna to operate at 70 or 50 MHz. Antenna phasing is typically 0 π for each of the two-strap antennas and 0 π π 0 for the four-strap antenna. The toroidal wave structure created by the antennas can be decomposed into a spectrum of discreet toroidal modes, N_ϕ. These modes are peaked at $N_\phi \approx 10$ for all antennas at the above phasings [15]. The antennas are shown in Figure 1-6.

C-Mod employs both a minority heating scheme and a mode conversion heating scheme. This thesis will focus mainly on results from plasmas with minority heating. In this scheme, the antennas heat at the fundamental ion cyclotron frequency of the minority hydrogen species. The bulk plasma is deuterium, and typically ~5% of the

plasma are protons. Depending on the strength of the field, the resonance location can vary in the plasma. At normal operating frequencies ($\sim$ 80 MHz) and toroidal field (5.4 T) the resonance location is located at the center of the plasma, $R \approx 67$ cm.

1.3.1 Fast-ion distribution

Because only the hydrogen minority ions are being directly heated by the ICRF antenna, a very energetic tail can be generated in the minority distribution function. This thesis is mainly interested in this energetic tail, also referred to as the 'fast-ion distribution'. The salient features of the fast-ion distribution are that it is very energetic relative to the main ions ($\sim$100 times more energetic) and it is highly anisotropic. The anisotropy arises because the resonance interaction between the ICRF waves and the minority ions imparts energy only in the perpendicular direction. The result is that the fastest ions are the ones that are in trapped orbits whose banana tips are near the resonance layer. A minority species distribution function from a simulation is shown in Figure 1-7.

Figure 1-7 shows a simulated distribution function at the outboard midplane. At the outboard midplane, a particle experienced the minimal value of toroidal field, and thus $v_\parallel/v$ is maximal. The axes represent the energies parallel and perpendicular to the magnetic field. Particles with $W_\parallel \gg W_\perp$ are passing particles. As these particles travel along flux lines they will gain more perpendicular energy, but provided that $W_\parallel > 0$ at all points, they will not undergo mirror reflection. Particles with $W_\perp \gg W_\parallel$ are trapped particles. These particles will be mirror reflected at some point on their orbits. The solid red line represents the trapped-passing boundary. Particles below this line are passing, particles above it are trapped. Directly above the solid red line there is a region bounded by solid green lines. The fast-ions that would normally inhabit this region are calculated to have orbits that take them outside the last closed flux surface and are hence lost from the plasma and removed from the distribution.

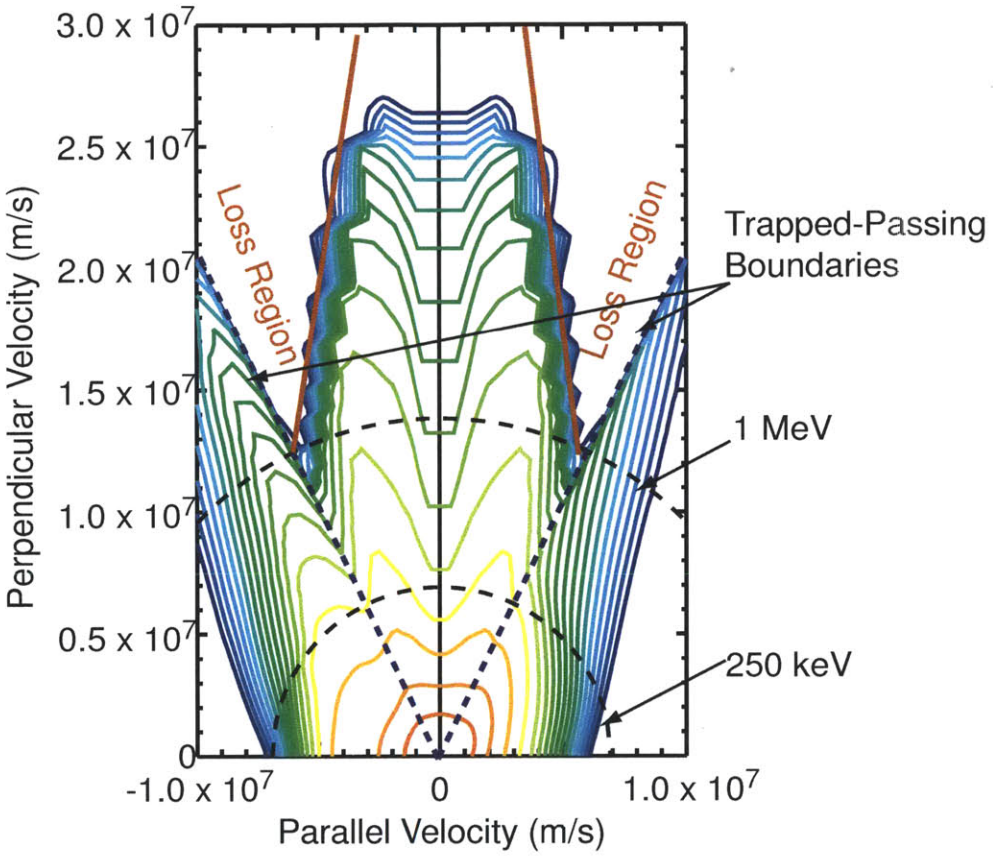

Figure 1-7: The minority ion distribution for a 600 kA plasma, calculated by the simulation code CQL3D is plotted in velocity space. The distribution is taken at the midplane, with $\rho = 0.3$, $\theta = 0$. Contours represent constant levels of the distribution function. Also shown are the trapped passing boundaries, the regions where ions are lost due to orbits, and contours representing constant energies at 0.25 and 1 MeV.

In the presence of ICRF heating, the distribution becomes distorted. Ions gain energy in the perpendicular direction each time they pass through the resonance layer. This distortion is easily seen in Figure 1-7. There are two 'rabbit ears.' indicating energetic ions at a specific range of pitch angles. Specifically, these are the previously mentioned energetic trapped particles that have banana tips on the resonance layer. The estimation of lost orbits will be discussed in more detail in Section 4.5.4.

Equilibrium and time dependence

The distribution shown in Figure 1-7 is an equilibrium distribution with a constant supply of ICRF power. As the fast-ions are heated, they undergo collisions with other ions and electrons. The energy deposited in the fast-ion tail by the ICRF balances the energy dissipated due to collisions with the bulk plasma. A full calculation is very difficult and requires numerical simulations, and these will be discussed in Chapter 4. However, here we will present classical estimates for various collisional processes as given in [16, 17].

When examining the time dependence of the fast-ion tail, we are interested in two things. The first quantity of interest is how long it takes for a fast-ion to slow down and equilibrate to the main plasma temperature. The second quantity of interest is how long it takes for an anisotropic distribution of fast-ions to relax to a Maxwellian distribution. We will examine the first quantity by estimating the slowing down time for the fast-ions, τ_s. In other words, if the ICRF power was turned off, the fast-ion energy is given by,

$$W(t) = W_0 e^{-t/\tau_s}. \tag{1.8}$$

In general, the ions we are interested in, move much faster than the bulk ion species but slower than the bulk electrons. In these limits we can write down the time it takes for fast-ions to slow down by considering collisions with both ions and electrons. For collisions with fast moving electrons, the slowing down time is given

by

$$\tau_s^{ie} = 1.98 \times 10^{19} \frac{\mu T_e^{3/2}}{n_e Z^2 \Lambda_{ie}}, \tag{1.9}$$

where the ion-electron Coulomb logarithm is

$$\Lambda_{ie} = 37.8 - ln\left(\frac{n_e^{1/2}}{T_e}\right).$$

For collisions with slow moving ions,

$$\tau_s^{ii'} = 3.5 \times 10^{17} \frac{\mu\mu'}{\mu^{1/2}(\mu+\mu')} \frac{W^{3/2}}{n_{i'} Z^2 Z'^2 \Lambda_{ii'}}, \tag{1.10}$$

where the ion-ion Coulomb logarithm is given by

$$\Lambda_{ii'} = 40.3 - ln\left[\frac{ZZ'(\mu+\mu')}{\mu T_{i'} + \mu' T_i}\left(\frac{n_i Z^2}{T_i} + \frac{n_{i'} Z'^2}{T_{i'}}\right)^{1/2}\right].$$

In the above equations T_s represents the plasma species temperature in keV. n_s represents the species density in m^{-3}. Z represents the atomic charge; $\mu = m_i/m_p$ represents the mass ratio relative to a proton mass, and W represents the fast-ion energy, also in keV. Primes indicate different ion species.

The Coulomb logarithm is a weakly varying function across the relevant range of plasma parameters. $\Lambda_{ie} \approx 15$ and for proton-deuteron interactions, $\Lambda_{ii'} \approx 20$.

Evaluating some of the constants for proton-electron and proton-deuteron reactions and taking $n_e \approx n_D$ gives us:

$$\tau_s^{ie}/\tau_s^{ii'} \approx 50 T_e^{3/2}/W^{3/2}. \tag{1.11}$$

The critical energy above which fast-ions slow down predominantly on electrons can be found by setting the ratio of the slowing down times to 1 and the result is that

$$W_{crit} \approx 13.5 T_e. \tag{1.12}$$

All of the fast protons studied in this thesis have energies above this critical value. Therefore, the primary damping mechanism we are concerned with is slowing down on electrons.

Lastly we will consider the time constant for temperature isotropization. For particles with a perpendicular temperature higher than the parallel temperature, this is given by [16],

$$4.4 \times 10^{17} \frac{T_{\|}^{3/2} A^2}{n_i \Lambda_{ie}} \left(-3 + (A+3) \frac{\tan^{-1}(\sqrt{A})}{\sqrt{A}} \right)^{-1}, \tag{1.13}$$

where

$$A = T_{\perp}/T_{\|} - 1.$$

Because of the strong heating in the perpendicular direction, the fast ion distribution is highly anisotropic (see Figure 1-7). Shown in Figure 1-8 is the isotropization time constant as a function of the dimensionless parameter A, for a plasma with electron density = 1.0×10^{20} m^{-3} and temperature of 3 keV. Also shown is the time constant for slowing down on electrons for reference. Chapter 5 will discuss the experimentally measured slowing down times and provide comparisons with these classical quantities.

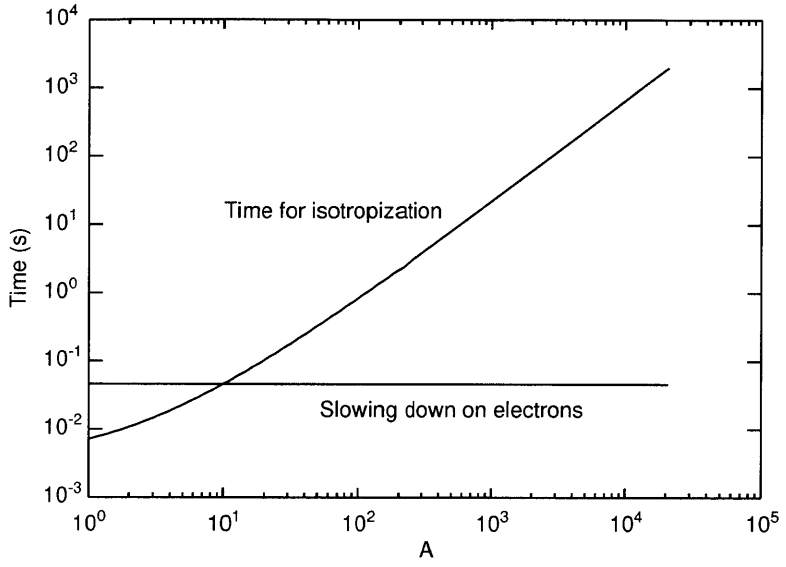

Figure 1-8: Time constants for slowing down on electrons and isotropization. Calculations are for a plasma with $T_{||} = T_e = 3$ keV and $n_e = 1.0 \times 10^{20}$ m^{-3}

Chapter 2

Diagnostics

Many different devices have been used on tokamaks to characterize the fast-ion distributions. There are several indirect methods that involve inferring the fast-ion distributions from other macroscopic plasma parameters such as sawtooth reheat times, temperature anisotropies, and neutron flux rates [18]. However, there are diagnostics that allow for direct measurements of fast-ions, and these direct measurements will be the focus of this chapter.

Measuring fast particles directly in the plasma is difficult. It is impossible to put a collector inside the plasma, because solid materials cannot survive the harsh environment. In lieu of direct measurements, diagnostics often attempt to reconstruct the fast particle distribution by considering those that escape the plasma. For example. neutrons produced from fusion reaction will not be confined by magnetic fields and escape immediately. However, a charged particle, such as an alpha particle created in D-T fusion or a fast proton heated by ICRF minority heating, will need to undergo a neutralization process before it can escape the magnetic fields. Measuring these charged particles requires knowing both the processes that give rise to them and the processes that permit them to exit the plasma. Fortunately, common neutralization processes, such as charge exchange and recombination have negligible effect on the energies of the reactants. Therefore, measuring these neutrals can be a good proxy

for direct measurement of the fast-ion species.

Alternatively, it is possible to directly measure the radiation from confined fast particles. With the increased resolution of spectrometers some measurements have recently become possible with this technique.

In this chapter, Section 2.1 describes some of the diagnostics on previous and contemporary tokamaks that provide the basis for the research described in Section 2.2. Section 2.3 provides information on other diagnostics unrelated to fast-ions that contribute to the results of this thesis.

2.1 Fast-ion diagnostics and experiments

2.1.1 History of neutral particle analysis diagnostics

The progenitors of the fast-ion neutral particle analyzers of today were built for some of the first fusion plasma experiments. Interestingly, many of the features on the first neutral particle analyzer, operated on the Soviet Union tokamak Alpha [19], still exist on diagnostics today. Dubbed an "atom analyzer," the diagnostic sought to characterize the fast ion distribution in the plasma by measuring the fast-ions that underwent a neutralization process and escaped the plasma. The fast neutrals passed through a gas-filled stripping cell and were ionized. The particles with a desired energy were then selected by applying an adjustable DC electric field. The chosen ions then impinged on a scintillator detector, creating a single count for each ion.

While the first atom analyzer could only measure a single energy point at a time, later devices had multiple detectors providing for multiple channels. Also, soon afterward, the diagnostics employed magnetic fields to separate out different ion species. All these features of the diagnostic would be staples for fast particle detection in the succeeding years

CENA on PLT

The Charge Exchange Neutral Analyzer (CENA) built for the Princeton Large Torus (PLT) is a convenient device to continue the history of neutral particle diagnostics. The diagnostic was referred to as a "charge-exchange" diagnostic, because charge-exchange was the dominant process by which ions neutralized and escaped the plasma. In CENA, like in the "atom analyzer," neutrals exiting the plasma passed through a helium filled stripping cell, where they would be ionized [20]. After exiting the chamber they would pass into a D-shaped detection chamber where parallel electric and magnetic fields separated the ions into different species and energies. Ions of the same species but different energies would experience a different radius of curvature from the magnetic field. Ions of different charge to mass ratios would be deflected differently from the electric field. These ions would then impinge on an electrically biased chevron microchannel plate. A diagram of the diagnostic can be seen in Figure 2-1.

The CENA design, like almost all analyzers before it, used electromagnetic fields to create energy and mass resolution. However, it did have drawbacks. The most obvious drawback was its large size. Both the stripping cell and the field region were very large. The additional neutron shielding that would be required for operation on TFTR made this design prohibitively large for use on that tokamak. [21]. Nevertheless, the diagnostic techniques appear on many future neutral particle analysis diagnostics. Even the CENA diagnostic itself would be reused on other tokamaks.

HENPA on TFTR

TFTR was a large D-T tokamak that was operated from 1982-1997. For this tokamak, a new charge-exchange neutral analyzer was required. Two changes were proposed in order to reduce the size of the neutral particle analyzer. The stripping cell was replaced by a foil and the B-field coils were replaced by rare-earth permanent magnets. The drawback of the foil was that there was now a non-negligible energy loss

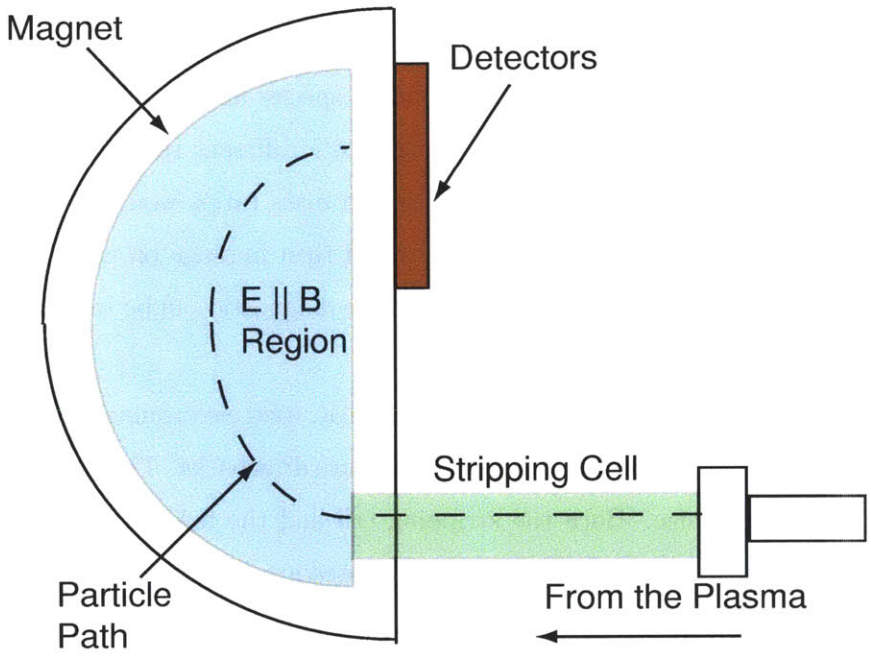

Figure 2-1: Cartoon of the CENA diagnostic installed on PLT.

when the fast neutral traveled through it. The only downside to the permanent magnets was their cost. The new diagnostic was called HENPA (High Energy Neutral Particle Analyzer) and not only provided information about fusion products [22] but also provided first results showing that magnetohydrodynamic induced modes were responsible for ejection of fast-ions [23, 24]. Ion losses due to these modes are still studied today [25].

CENA on Alcator C-Mod

After CENA ended its service in Princeton, it was donated to MIT's Alcator group for use on the Alcator C-Mod tokamak and renamed as the NPA (Neutral Particle Analyzer). As mentioned in Chapter 1, C-Mod uses ICRH for its main auxiliary heating, and it was thought that the NPA would be ideal for benchmarking the performance of the ICRF antennas. However, there was an inherent difficulty with using the diagnostic on C-Mod. The large size of the the diagnostic prohibited any viewing line besides a straight in view at the horizontal midplane. This is a nonideal viewing angle for the fast ion distribution. A horizontal view at the midplane will only detect deeply trapped particles on the outboard half of the plasma, and barely trapped particles on the inboard half.

While the NPA never produced results for the the fast-ion distribution in the plasma center, it did produce measurements of the ICRF power deposited outwards of $r/a = 0.4$ [26] and in the plasma edge [27]. The NPA was not long-lived on C-Mod and it was removed and replaced with a diagnostic neutral beam (DNB).

NDD on TFTR

Towards the end of its experimental lifetime, TFTR employed Natural Diamond Detectors (NDDs) to measure fast-ion spectra [28]. These detectors showed that there was a possibility to shrink the size of neutral particle analyzers considerably. These detectors are currently in use on the Large Helical Device in Japan [29].

CNPA on C-Mod

The CNPA (Compact Neutral Particle Analyzer) will be described in more detail in the next section, but its history will be briefly described here. Originally built by Vincent Tang in 2003-2005 [30], it made use of a novel detection technique that reduced the size of the device considerably. In the new diagnostic, the large electromagnetic chamber was exchanged for considerably smaller photodiodes. The main advantage of the size reduction is that the diagnostic could now be moved to a vertical port. The sightline on the vertical port was far superior for measuring the tail of the fast-ion distribution, and the measurements Tang made were central to his doctoral thesis [2].

Tang's research focused on the characterization of the fast-ion distribution between 60 and 300 keV. The distribution results were calculated by comparing active and passive measurements. Active measurements include the use of a diagnostic neutral beam, passive measurements do not. Comparing the active and passive spectra one can, in principle, determine the fast-ion distribution.

The main results of Tang's research were an estimation of the fast-ion 'effective' temperature and a theory that charge-exchange of the fast protons with hydrogen-like boron was the dominant neutralization method for higher energy fast-ions. Effective temperature calculations are discussed in more detail in Chapter 3. Tang also simulated a low-power plasma with an advanced full-wave/Fokker Planck simulation model, AORSA-CQL3D, and obtained reasonable agreement with CNPA results. These simulation codes, Tang's results, and new and improved simulations will be discussed in Chapter 4.

2.1.2 Alternative fast-ion diagnostic techniques

Spectroscopic diagnostics

The FIDA (Fast-Ion D-Alpha) detector is a spectrometer that focuses on the $n = 3$ to $n = 2$ transition in deuterium [31]. For an equilibrium Maxwellian distribution, the

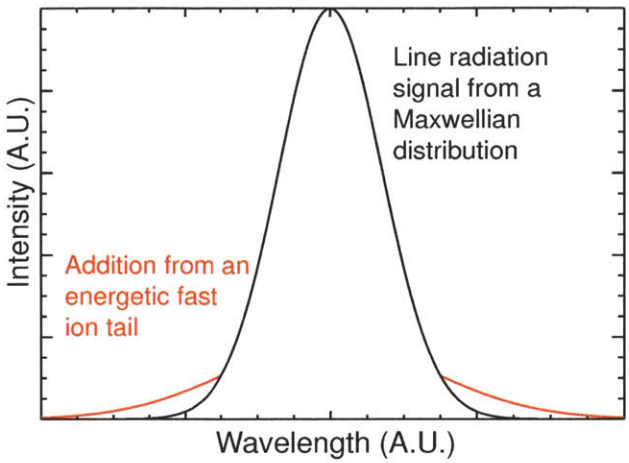

Figure 2-2: The intensity of line radiation is plotted against wavelength in arbitrary units. The Gaussian signal of a spectroscopic line of a species in an equilibrium Maxwellian distribution is shown in black and the deformation of the spectrum due to a energetic fast-ion tail is shown in red

shape of the line will be Gaussian. However, with a large energetic tail, the Gaussian will be deformed and the spectrum broadens, as shown in Figure 2-2.

The main challenge for the FIDA diagnostic is extracting the fast-ion signal from the various sources of noise, including radiation from the plasma edge, radiation from excited-state beam neutrals, and background bremsstrahlung radiation. Furthermore, energetic neutralized hydrogen my travel several cm from the point of neutralization before emitting a photon. Despite these difficulties, the diagnostic has had success in measuring the fast-ion distribution on DIII-D, NSTX and JET and a similar diagnostic is being built for C-Mod. As of the completion of this thesis, the fast-ion diagnostic, called FICX (fast-ion charge-exchange) has demonstrated the ability to measure ^{3}He fast-ion distributions [32].

Lost-ion detectors

So far all the diagnostics mentioned have attempted to measure confined fast-ions. However, it is also useful to measure the population of unconfined ions that have

orbits intersecting the vessel walls [33]. A common methodology is to have a box with a small slit in it. Along one of the walls of the box is a detector. Ions that enter the slit impinge on the detector at different places depending on their incoming energy and pitch angle, analogous to the way that a E || B detector works.

Lost-ion diagnostics appear on several other tokamaks including ASDEX-Upgrade [34], NSTX [35], JET [36] and DIII-D [37]. No lost ion detectors are operable on C-Mod, but a new lost ion detector is schedule for installation in 2011-2012.

Gamma Ray Spectroscopy

A new technique used on the JET tokamak employs Gamma Ray Imaging to determine information from fast-ions [38]. Highly energetic fast-ions ($\sim$ 5 MeV) can collide with impurity ions and excite energetic nuclear states which then decay and emit a gamma ray. This diagnostic has been used to verify the existence of highly energetic ions on JET.

2.1.3 Contemporary diagnostics and experimental results

Fast-ion diagnostics, including neutral particle analysis, are found on many tokamaks. This section will discuss some of the other diagnostics that currently exist on tokamaks around the world. In addition, we will outline some of the research results of these diagnostics.

Fast-ion experimental results on NSTX and DIII-D

NSTX, (National Spherical Tokamak Experiment) is a spherical tokamak located at the Princeton Plasma Physics Laboratory in Princeton, NJ. DIII-D is a tokamak at General Atomics in San Diego, CA. Neither tokamak employs ICRF minority heating, but both experiments use neutral beam heating and High Harmonic Fast Wave (HHFW) heating [39]. Neutral beam injection (NBI) produces fast ions up to 8 to 10 times the electron temperature, and HHFW can interact strongly with energetic

ions that are present in NBI-heated devices. Both machines have multiple diagnostics to study fast ions.

NSTX has several diagnostics to measure the fast-ion population including the lost ion detectors mentioned above. The $E \parallel B$ detector that was first used on TFTR [40, 41] is now used on NSTX. In addition to this detector there are solid state detectors similar to the ones used on C-Mod. Both NPA diagnostics have horizontal views into the plasma.

The SSNPA (Solid State Neutral Particle Analyzer) compliments the $E \parallel B$ NPA on NSTX providing measurements at additional viewing angles. The diagnostic uses a 1 mm $\times$ 1 mm silicon diode detector made by IRD [42]. The main advantage of the solid-state detector is its small size, allowing for many spatial channels. The main disadvantage is its high noise susceptibility, degrading energy resolution. On NSTX, the SSNPA has a nominal energy resolution of 10 keV. NSTX and C-Mod were pioneers in using solid-state silicon semiconductor detectors to measure fast neutral particles in tokamaks.

DIII-D is well equipped to measure beam-heated and HHFW heated fast particles. In addition to previously measured FIDA diagnostics and lost particle detectors it also has vertical viewing NPA chords that can measure energies from 5-75 keV [43]. There are currently plans to install solid state detectors on DIII-D as well.

Research on DIII-D and NSTX has focused mainly on measuring the way fast-ions affect and are affected by MHD activity such as TAEs and sawteeth crashes.

NPA on JET

The Joint European Torus (JET) in Culham, England is currently the world's largest tokamak. Like C-Mod, JET uses a minority ICRF heating scheme for auxiliary plasma heating, in addition to other sources of heating [44]. JET employs an $E \parallel B$ NPA detector that views vertically from the top of the tokamak. Therefore, despite having a different detector, the JET detector's viewing geometry and associated plasma physics

are similar to C-Mod's. In addition to the NPA, JET also has lost-ion diagnostics and gamma ray spectroscopy, as describe above. These diagnostics constitute the most complete diagnostic suite for fast-ion measurements. However, despite the excellent diagnostic coverage, no attempt has yet been made to compare experimental results to simulations (see also, Chapter 4) [45].

2.2 The F-top and J-top CNPAs on Alcator C-Mod

Alcator C-Mod currently has two NPA diagnostics that use semi-conductor diode detectors. Both diagnostics have vertical views looking down from the top of the vessel (see Figure 2-4). This section will focus on the physical hardware of these diagnostics. A schematic of the J-Top detector is shown in Figure 2-3.

2.2.1 Diagnostic hardware

Both CNPAs use the same technique for fast-neutral detection. Fast-ions that are neutralized through some process in the plasma exit the plasma in the direction they were traveling immediately prior to neutralization. A small fraction of these neutrals pass through an aperture en-route to the biased photodiode detectors. A thin, $\sim$150 nm, aluminum foil covers the detectors. The foil blocks low energy photons, a main source of noise for the detectors. Additionally, the foils re-ionize the fast neutral, although the fast neutral would ionize immediately at the surface of the detectors if the foil were not present. It is important to note that since an ion will be deflected by the strong magnetic field present near C-Mod, the foil must be close to the detectors.

The fast-ion creates charge-hole pairs as it travels through the active region of the semiconductor diode detector slowing down the fast-ion. Provided that the ion slows down completely in the detector, the number of charge-pairs created is directly proportional to the ion's initial energy. However, if the impinging ion is too energetic it

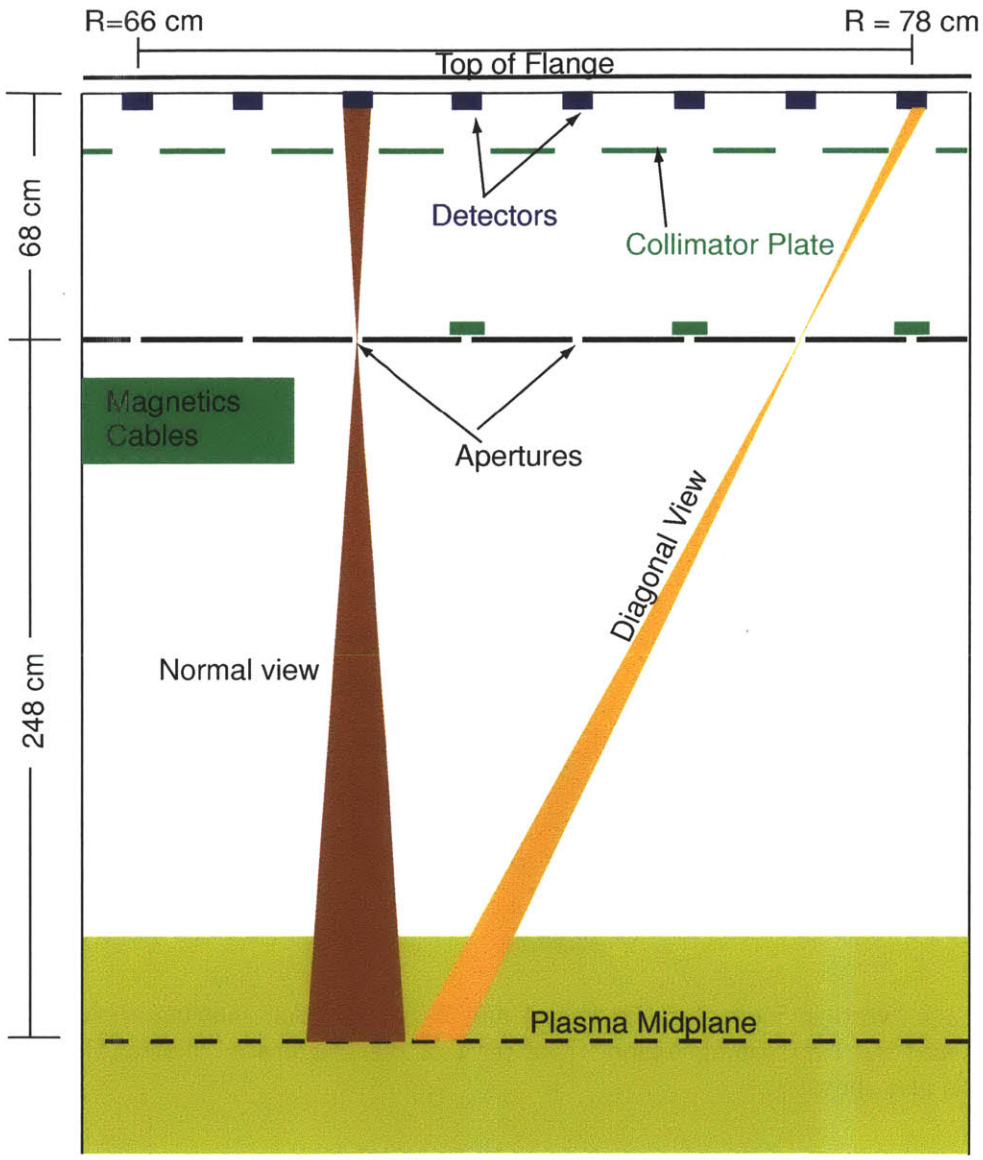

Figure 2-3: Schematic of the J-Top CNPA

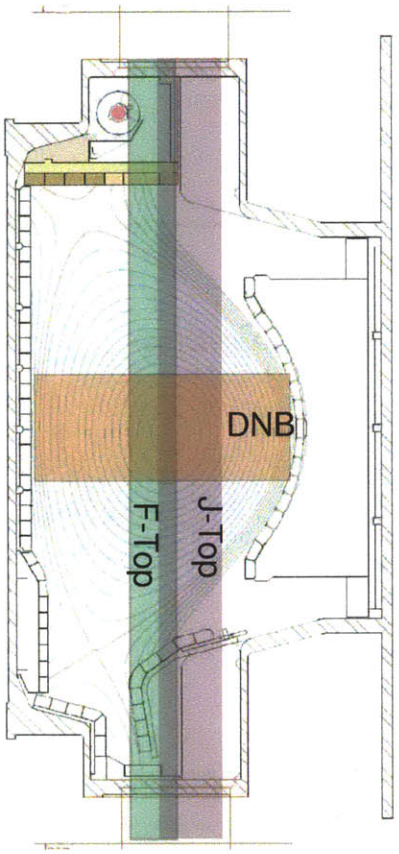

Figure 2-4: Vertical views for the F-Top and J-Top CNPAs, showing their radial extents and the overlapping region. The path of the Diagnostic Neutral Beam at F-Port is also shown.

can pass through the entire active region before depositing all of its energy. Therefore, there is a ceiling for the maximum detectable ion energy. This ceiling is dependent on the depth of the active region. The F-top detectors have a shallower active region of 30 μm and thus a lower maximum detectable energy. The J-Top detectors have an active region of 100 μm and their ceiling is proportionally higher. C-mod produces many fast-ions that are above the F-top maximum energy (600-700 keV) but still below the J-top maximum energy, which is estimated to be around 2 MeV. Fast-ions above 600 keV will still appear on both diagnostics, but in the F-Top signal they will be placed in energy bins near 600 keV.

For each impinging ion, the detector outputs a charge pulse, the magnitude of which is directly related to the particle energy. The output of the detector is then processed in the electronics shown in Figure 2-5. The processing electronics provide amplification and shaping. The preamp used is a Cremat CR-110 rev. 2 preamplifier. The preamp changes the incoming charge pulse to a sharp edge in voltage with a magnitude of a few mV. The shaper board is a custom made board adapted from one developed by John Liptac for the Hard X-Ray Diagnostic on C-Mod. The adapted circuit design for the shaper board is shown in Figure 2-6. The original design can be found in Liptac's thesis [46]. The important alterations in the shaper board design involve lowering the gain and sacrificing resolution to extend the operating range of the electronics. The J-Top detectors, with a 100 μm active region and the extended operating range in the electronics, can detect fast ions up to 2 MeV.

The output of the shaper is digitized by a CPCI digitizer at 10 MHz. Typical shaper pulses are Gaussian-shaped with full-width half maxima around 1 μs, so the 10 MHz digitization rate provides adequate temporal resolution. A plot of a typical pulse at the output of the shaper is shown in Figure 2-7.

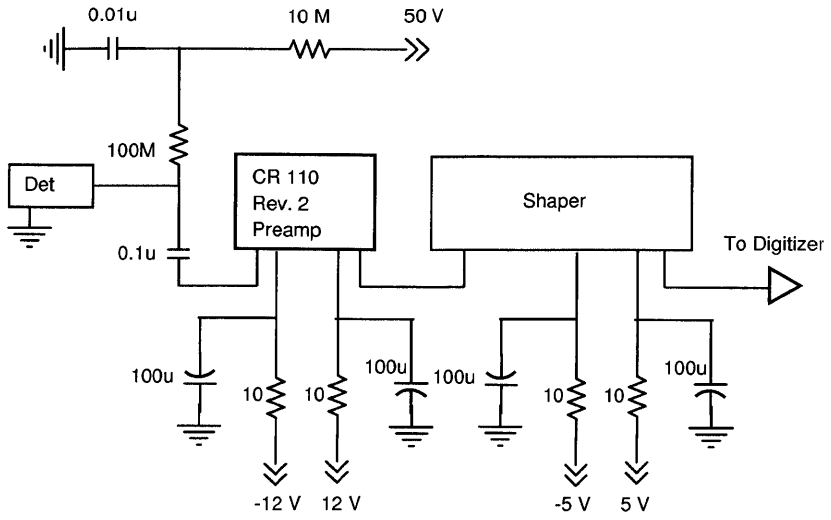

Figure 2-5: Circuit diagram for the processing electronics of the CNPA.

2.2.2 F-Top CNPA

The F-Top CNPA consists of a single 3 detector 3-ELA AXUV photodiode array manufactured by International Radiation Detectors (IRD). Each detector is 1 mm^2 and they are arranged along a radial chord of the tokamak and view vertically downward. The sightlines of the detectors pass through a single adjustable aperture. The detectors are covered by a ~170 nm thick aluminum foil, that reduces the energy of the incoming ions by approximately 20 keV.

The F-Top detectors were originally placed toroidally on the tokamak so that their sightlines intersect the diagnostic neutral beam at the plasma midplane. However, in 2006 the neutral beam was pivoted toroidally causing the new beamline to intersect the plasma at an angle. As a result the detector sightlines are now off of the beam center. The detector views and the current and former beam profiles can be seen in Figure 2-8.

The detector sightlines were calibrated after both the 2009 and 2009-2010 campaigns by having a visible camera view through a mask that was the same size as

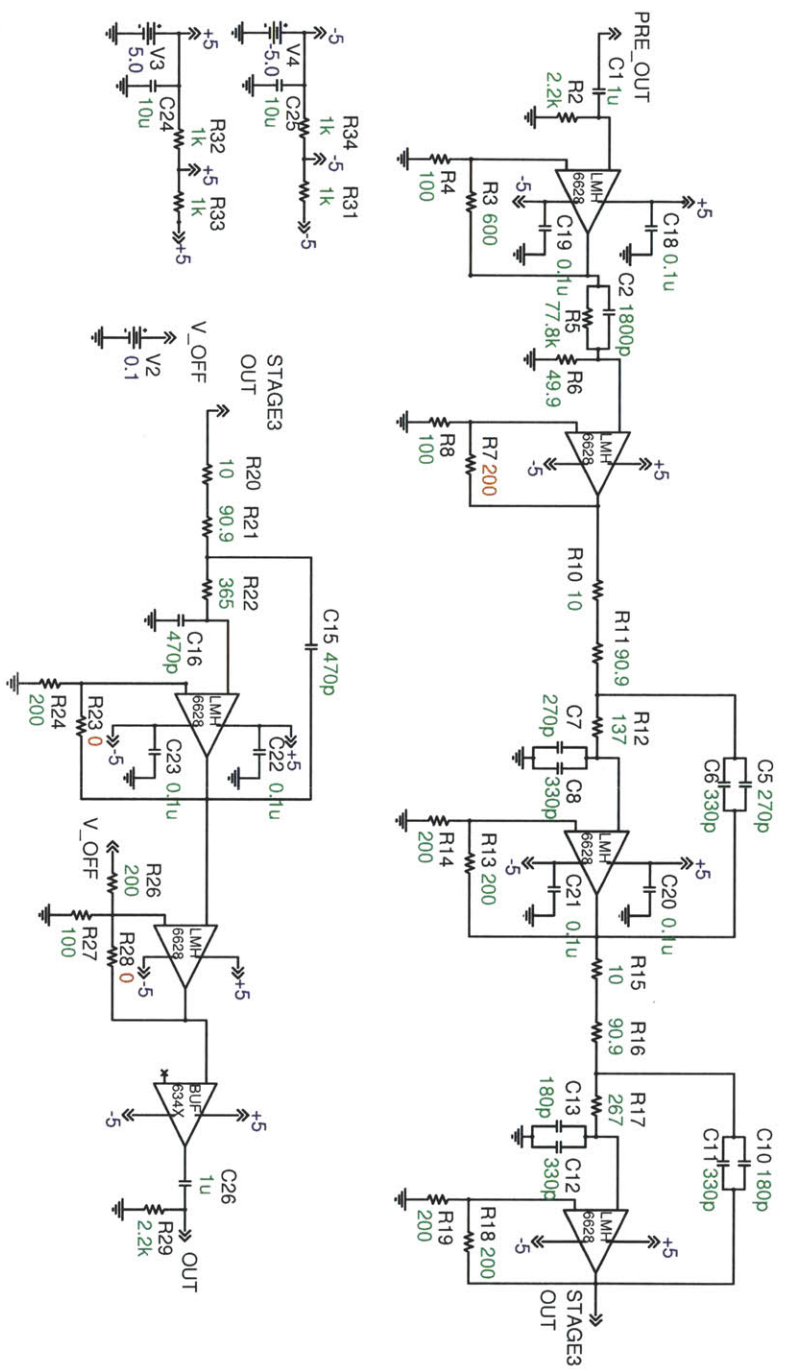

Figure 2-6: Circuit diagram for the shaper used in the CNPA. Values in red (R7, R23 and R28) have been altered to reduce the gain. In some cases this involved removing the resistors entirely. This diagram also incorporates the changes outlined in J. Liptac's thesis appendices [46].

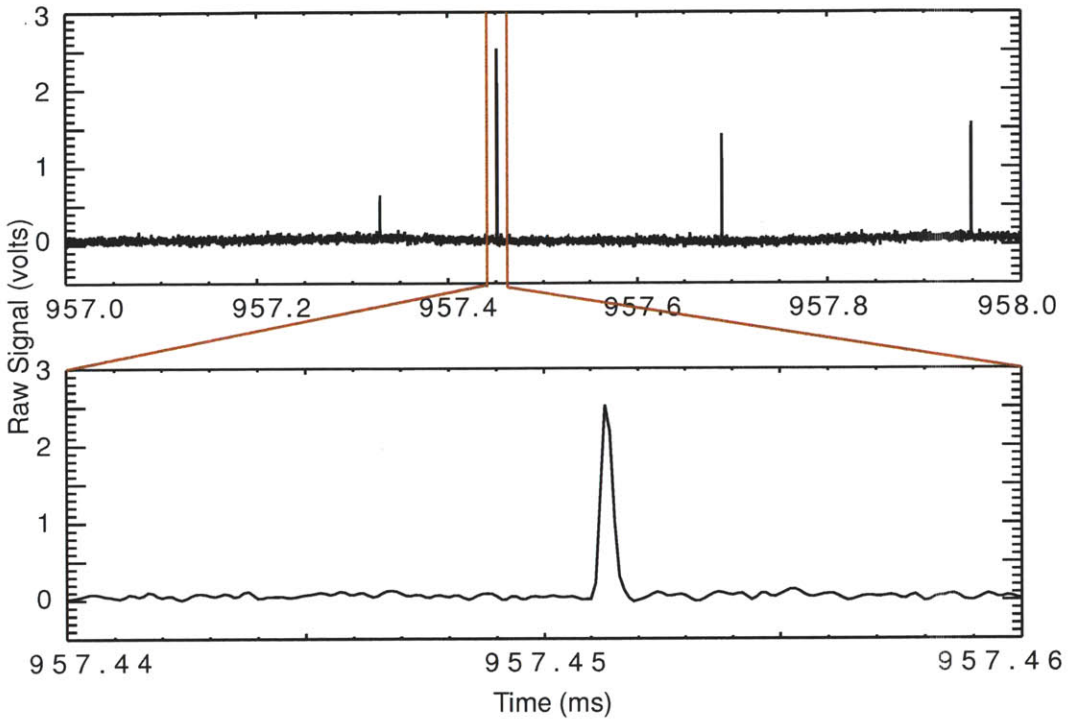

Figure 2-7: Digitizer voltage traces are plotted against time for an example single fast-ion event.

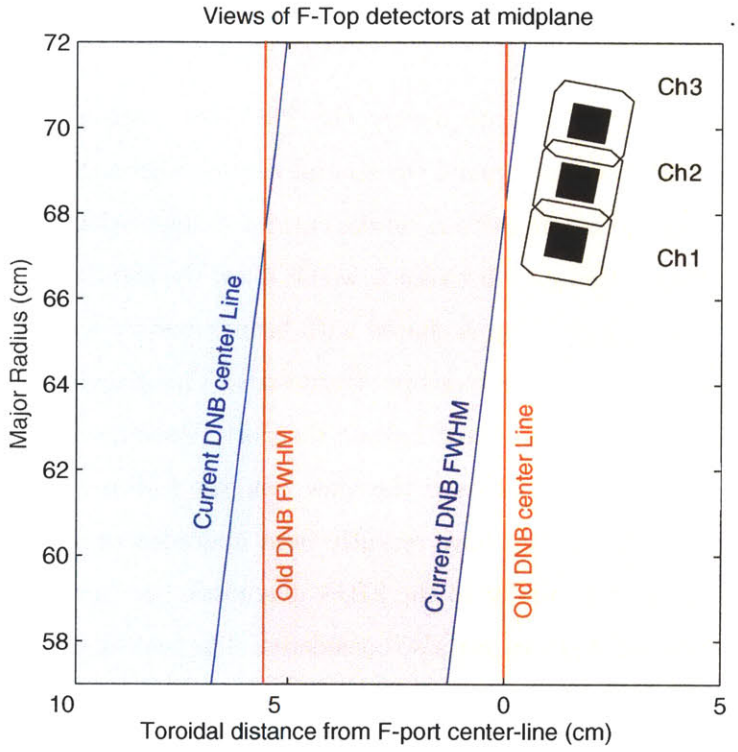

Figure 2-8: The views of the F-Top detectors are plotted looking down on the outboard midplane. The solid black regions denote the umbras while the solid line contour denote the penumbras. The shaded red region shows the path of the DNB at the midplane for the old orientation. The shaded blue region is the current DNB orientation.

the detectors. An LED was positioned at a known location in the vacuum vessel and camera images were recorded, thus giving the viewing areas for the detectors. These were found to be in agreement with a simple geometric calculation.

2.2.3 J-Top CNPA

Location

Planning for the J-Top CNPA began during the 2007-2008 campaign. The main purpose of the new CNPA was to expand the spatial viewing region. Several different geometries were considered before settling on the current configuration. An expanded view on F-Top was most desirable, because it would allow the sightlines to intersect the DNB. However, the top of F-top is shared with beam emission spectroscopy and charge exchange recombination spectroscopy diagnostics. The diagnostics are inside a periscope that occupies the outboard half of the port, leaving only the straight down view on the inner portion. This is the view that the F-Top CNPA currently uses. The spectroscopy diagnostics have recently been upgraded to include Fast-Ion Charge-Exchange diagnostics similar to the FIDA diagnostic (see Section 2.1.2 [32])

Installing a CNPA on F-bottom was also considered. The bottom port is currently occupied by a pneumatic scanning probe, a diagnostic that is not dependent on the diagnostic neutral beam. Unfortunately, it was determined that while moving the probe to another port was technically feasible, it would be extremely difficult, and there was no other open port on the bottom of the vessel to which the scanning probe could move.

Horizontal, wall mounted CNPA views were considered, but were rejected because of feasibility concerns. The signal that exits the detector is extremely small and prone to noise fluctuations. Therefore, it is extremely important to keep the wires between the detector and the preamp as short as possible. Thus, either the CNPA detectors need to be near a vacuum-air interface or vacuum compatible preamps and electronics need to be developed. Furthermore, wall mounted detectors would not

have the benefit of viewing through adjustable apertures. While, having straight radial horizontal CNPA views at various heights would be ideal, there is not sufficient port room on C-Mod to accommodate them.

For these reasons, the views at the unoccupied vertical port at J-Top were considered to be the best possible choice. This location allowed us to have an adjustable aperture, a gate valve, a ceramic break, and sufficient room between the aperture and the detectors to provide for a reasonable magnification factor. A CAD drawing of the entire diagnostic is shown in Figure 2-9.

The vertical views intersect flux surfaces at an angle near perpendicular to the magnetic field. Thus, the CNPA detects particles that have low pitch-angles at the point of neutralization. That is to say, the CNPA views particles near their banana tips.

Hardware

Vertical ports on C-Mod extend from midplane impact radii of $R = 59$ cm to $R = 78$ cm. The magnetic axis is located at about $R = 67$ cm. However in 2007 a cryopump was installed that blocked views of the inner half of vertical port. A cross-section of the cryopump can be seen in Figure 2-10. The cryopump itself blocks views with $R \leq 64$ cm. Together with associated baffling, the cryopump blocks views inboard of 70 cm. For several ports, including F-Top, the cryopump was altered to make room for vertical views of diagnostics. The cryopump was not altered on J-Top. Nonetheless, views inboard of 70 cm were desired and to accommodate this the baffling structure was modified to extend the viewing region up to $R = 64$ cm. However, because of the presence of magnetics cables, views inboard of $R = 69$ cm were still not accessible (see Figure 2-3). An image of the vertical view down J-Top with the magnetics cables is shown in Figure 2-11.

An adapter flange was constructed and placed on top of the port. This custom-made flange adapted the 10 inch diameter to an off-center 8-inch diameter. Above

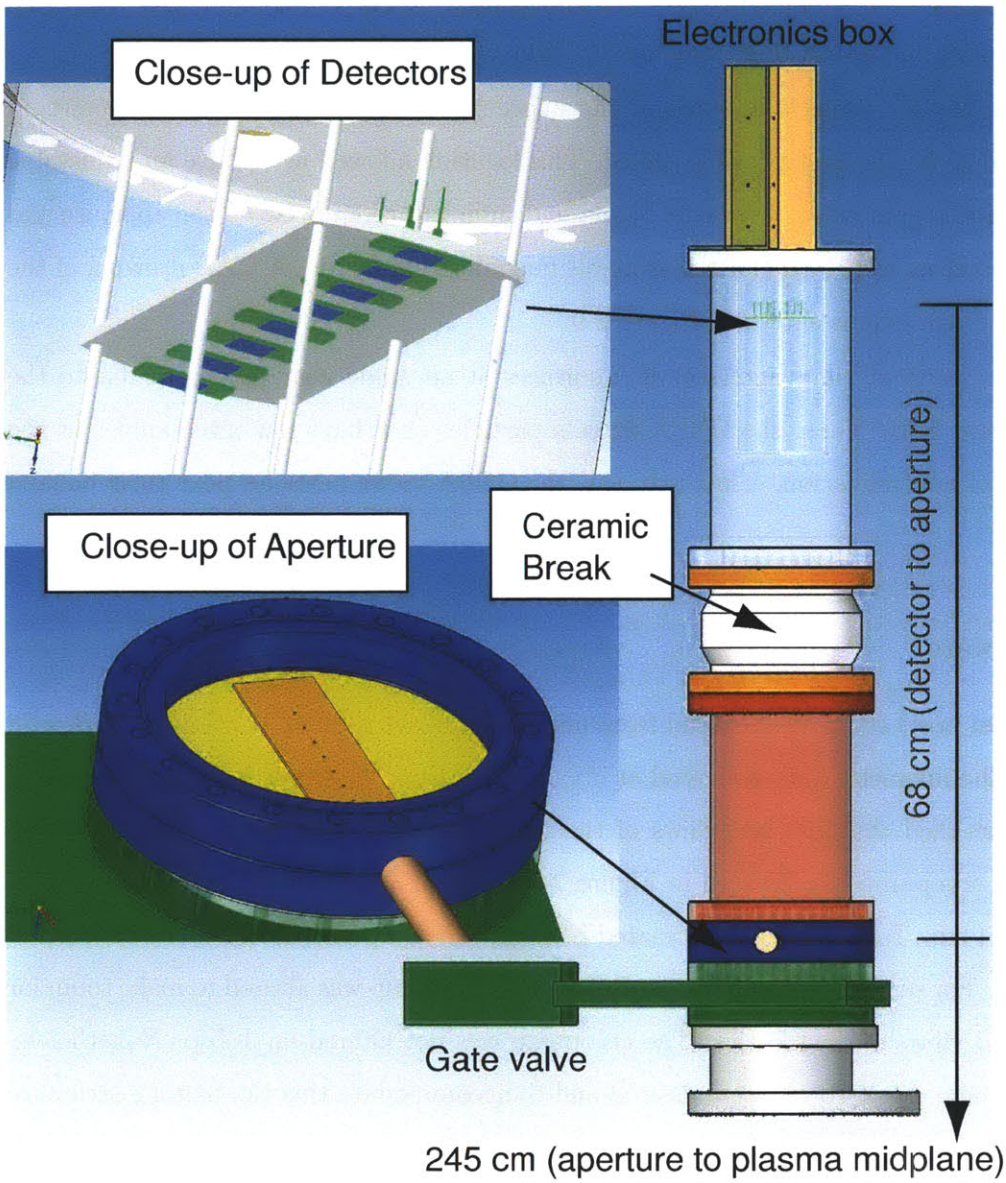

Figure 2-9: CAD drawing of the J-Top CNPA with insets to show the detector mounting structure (top left) and the aperture (bottom left). The structure is pumped out from a location on the top flange behind the electronics box.

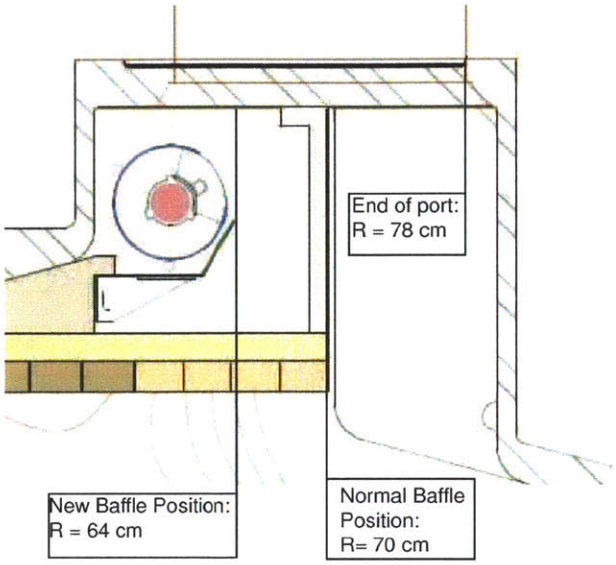

Figure 2-10: Cross-section of the top of the C-Mod vessel showing the position of the vertical port, the cryopump, and the new baffling

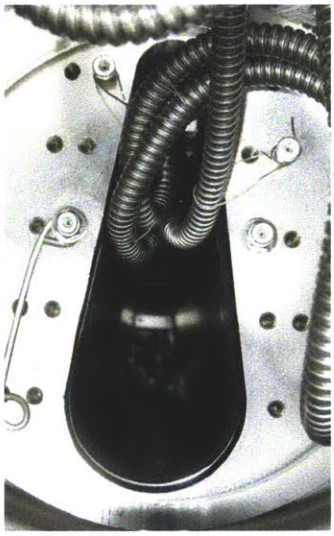

Figure 2-11: A view looking down the top of J-Top. Shown are the magnetics cables occluding the view of the inner section of the port.

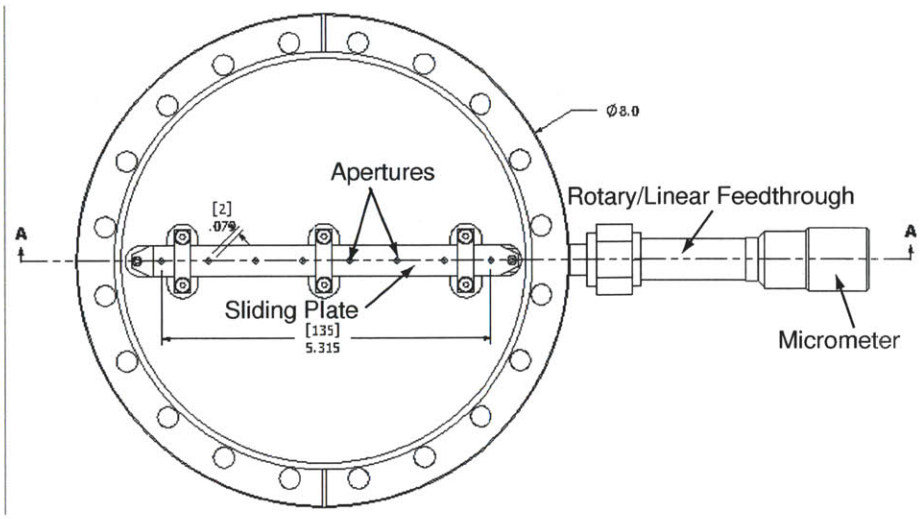

Figure 2-12: Schematic of the J-Top aperture. An adjustable micrometer allows one plate to slide over the other adjusting the size of the apertures. Aperture design and construction was done by McAllister Technical Services.

the adapter flange was a gate valve. The gate valve allowed for vacuum isolation of everything above it. This is desirable in case there was any need to adjust the detectors without disturbing the C-Mod vacuum.

An adjustable aperture built by McAllister Technical Services is located above the gate valve. Having an adjustable aperture is important for gathering data in a wide variety of conditions because the CNPA signal level depends strongly on various plasma parameters. A schematic of the aperture is shown in Figure 2-12. The aperture consists of two plates, one fixed and one sliding. Each plate has 8 diamond holes in it, 2 mm per side. Therefore, a fully open aperture has an area of 4 mm^2. The sliding plate is connected to a linear feedthrough controlled by a rotary micrometer. The plates are made from a beryllium-copper alloy which allows them to slide across each-other or across stainless steel with minimal friction. The current design does not allow for individual adjustment of each aperture. However, if different aperture values are desirable for different views, it is possible to alter one or both of plates.

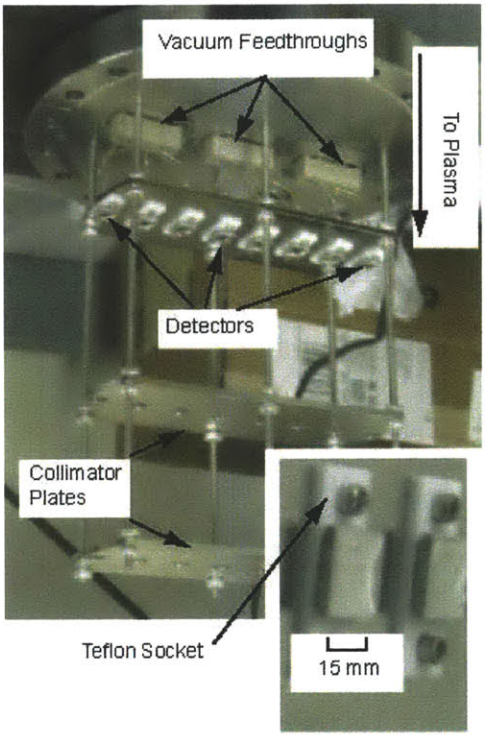

Figure 2-13: The J-Top detectors, mounted on the vacuum flange.

Detectors

The J-Top CNPA consists of 8 detectors. The detectors, manufactured by International Radiation Detectors, Inc., are individual HS20 AXUV detectors with an area of 20 mm^2. The detectors are arranged so that their sightlines intersect the midplane along a radial chord of the tokamak and are spaced 1.9 cm apart. A picture of the detectors mounted on the flange is shown in Figure 2-13. Due to the interference from magnetics cables, the two innermost detectors have occluded views. The six detectors with clear sightlines view the plasma on vertical chords that range from $R \approx 70$ cm to $R \approx 78$ cm with footprints on the midplane of $\sim$1 cm (see Figure 2-3).

To prevent detectors from viewing through adjacent apertures, collimator plates were fashioned to block diagonal lines of sight between one detector and an adjacent

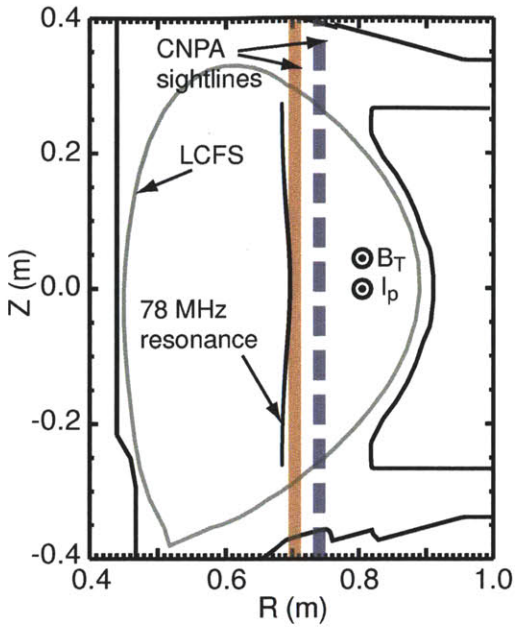

Figure 2-14: Sightlines for the J-Top detector for CNPA channels at R = 70 cm and R = 74 cm are shown. Also shown is the AORSA calculated resonance location for a typical C-Mod plasma.

aperture. Unfortunately, due to a last minute design change, the distance between the detectors and the apertures were increased and the collimator plates were rendered ineffective. There was insufficient time to fashion new collimation optics, so instead some apertures were blocked off. Therefore, there are direct lines of sight for three detectors at $R \approx$ 70,74 and 78 cm. The remaining three detectors have only the diagonal lines of sight through adjacent aperture.

Shown in Figure 2-14 are sample sightlines for two of the CNPA channels. Also shown, is the resonance locations for J-Antenna at 5.1 T. This location is similar to the location of D and E antennas at 5.4 T.

Electronics

A new electronics box was built to process the signals from the J-Top detectors. The box houses the preamps and the shapers for the 8 channels. Each preamp and shaper is electrically isolated from the others by removable aluminum plates. In the absence of these plates, there is enough interference between the components to cause large noise oscillations in the signal output. The electronics box is shown in Figure 2-15. A CAD rendering of the entire J-Top CNPA structure is shown in Figure 2-9.

2.3 Other diagnostics

Several other diagnostics are relevant to characterizing the plasma discharges analyzed in this thesis [47]. A brief description of these diagnostics is given in this section.

Two-color interferometry for electron density

Most of the density measurements in this thesis will be taken from two-color interferometry (TCI) measurements [48] [49]. The two-color interferometer measures an integrated density along several vertical chords. Line-averaged density is obtained by dividing by the path length. In general plasma density profiles are relatively flat in the plasma core, so using this measurement as an estimate of the plasma density is reasonable. Unless otherwise noted, all density measurements will be derived from this diagnostic.

Electron temperature from electron cyclotron emission

The Electron Cyclotron Emission (ECE) [47] diagnostic provides measurements of the core temperature by measuring the second harmonic cyclotron emission from plasma electrons. Unless otherwise noted, all electron temperature measurements are from the ECE diagnostic.

Figure 2-15: The box housing the J-Top electronics

Temperature and density profiles from Thomson scattering

In addition to the line-integrated interferometry measurement and the ECE temperature measurement, additional profile data for these parameters can be obtained from Thomson scattering [50]. Thomson scattering measurements are obtained by passing a very high energy pulsed laser vertically through the plasma and spectroscopically measuring the scattered light from a horizontal port. Like other spectroscopic diagnostics, the width of the line provides a temperature measurement and the area under the spectroscopic curve gives a density measurement.

The Thomson scattering diagnostic has the advantage that it is able to take measurements at specific locations in the plasma, as opposed to the line-integrated TCI measurements. Therefore it is able to obtain local temperature and density measurements at the plasma edge. However, the Thomson scattering signal is typically very small compared to a subtracted background, and the uncertainties tend to be larger than other measurements. Nevertheless, Thomson scattering data will be used as input for the simulations in Chapters 4 and 5.

Impurity measurements from spectroscopy

Spectroscopic measurements are used for a variety of parameters. Estimates of the minority fraction are obtained by two different methods. One measures the ratio of the brightnesses between the D_α line and the H_α line. Additionally, the Phase Contrast Imaging diagnostic can radially locate the ion-ion hybrid resonance layer, and from there, deduce the minority concentration [51].

Additionally, there are attempts to measure the impurity boron. Most of these measurements are made at the edge [52], however recently measuring the core boron with neutral-beam induced charge-exchange recombination spectroscopy has been attempted [53].

Magnetics and EFIT reconstruction

C-Mod is equipped with numerous coils and magnetics loops to provide measurements of the toroidal field and of the total plasma current. More detailed measurements are available at the edge from wall mounted coils [54]. Plasma equilibrium fields are obtained by solving the governing magnetohydrodynamic equations given the boundary conditions obtained by the edge magnetics [13].

Chapter 3

Analysis of CNPA detected fast-ion distributions

This chapter describes the methodology used to convert the raw signal from the CNPA electronics to a fast-ion spectrum in the plasma. In addition, we provide preliminary analysis of the fast-neutral distribution at the detector and of the fast-ion distribution in the plasma. We begin with an explanation of the routines that convert the raw data into the distribution of fast-neutrals that have reached the detector (Section 3.1). Then, we discuss the way that this spectrum at the detector depends on plasma properties (Section 3.2). Specifically, we find indications that the fast-ion distribution suffers from increased transport at low currents, and that the most energetic distributions appear at low plasma densities. These findings are independent of the amount of RF power input into the plasma. Lastly, we describe the methods used to convert the fast-neutral distribution seen at the detector to an estimate of the fast-ion distribution in the plasma (Section 3.3). We verify that the trends previously discovered in the analysis of the fast-neutral distribution at the detector are also present in the plasma distribution. Key findings are that the fast-ion distribution in the plasma exhibits a reduction in the effective tail temperature at low currents, and that there is no clear increase in effective temperature with increased

RF power after a certain power level. Many of the methods described in this chapter to calculate the fast-ion distribution in the plasma will also be used in evaluating simulation results with a synthetic diagnostic as described in Chapter 4.

3.1 Converting raw signal to fast-ion distributions at the detector

This section describes the analysis routines that take the raw data from the digitizers and convert it into a fast-ion distribution at the detector. Here, we discuss noise sources, pulse height analysis routines and automated threshold detection routines.

3.1.1 Noise sources

The digitized CNPA signal is subject to several sources of noise. The noise sets a minimum energy threshold, below which we are unable to detect incoming fast-ions. The signal to noise ratio is used as an indicator for what constitutes an acceptable measurement.

Soft X-rays, ultraviolet and visible light

Lower energy photons in the range extending from visible light up to soft x-rays provide a slowly varying current signal at the detector output. The photon induced current varies slowly compared to the fast ion impact time scale (10 μs). As described in the previous chapter (see Section 2.2.1) a thin aluminum foil is placed over the detectors, to block out most of the lower end of this spectrum. Nonetheless, significant amounts of soft x-rays do penetrate the foil. This DC signal is filtered out by the electronics. However, large enough DC signals will cause saturation of the detectors or electronics. Thus, saturation due to photons limits the operation of the CNPA in highly radiative plasmas. A thicker foil can be employed, however the foil also

attenuates the fast-ions and contributes to calibration errors. The primary purpose of the aperture is to lessen photon noise to acceptable levels.

Hard X-rays

Some plasmas on C-Mod generate runaway electrons. Runaways occur when the acceleration due to the electric field exceeds the drag due to collisions. A runaway electron emits photons in the x-ray range. These x-rays may deposit some of their energy in the active region of the detector just as a fast-ion would. Since these pulses are indistinguishable from fast-ion pulses we do not generally analyze plasmas with large hard x-ray signals. The pulses from hard x-rays often occur at the beginning of the plasma or during very low density discharges. They are loosely correlated to signals from hard x-ray detectors. An example of a discharge where considerable x-ray noise appears on the CNPA electronics output is shown in Figure 3-1. Hard x-rays are the only identified noise source that causes false counts to appear on the CNPA detectors.

Other noise sources

Because of the very large signal amplification in the CNPA electronics, any electronic pickup also gets amplified. This electronic noise determines the minimum energy fast-ions that are detectable. Much effort has been made to shield the CNPA from noise sources (see Figure 2-15). Even small holes in the electronics box can cause very large electronic pickup noise. Some sources of noise have been successfully identified, while the causes for others are as yet unknown. For example, the CNPA exhibits noise spikes when the ICRF faults. It also experiences elevated noise signals when the diagnostic neutral beam is activated. All of these sources of noise are characterized by excursions above and below the signal baseline. In some plasmas these excursions are large enough that CNPA analysis is impossible.

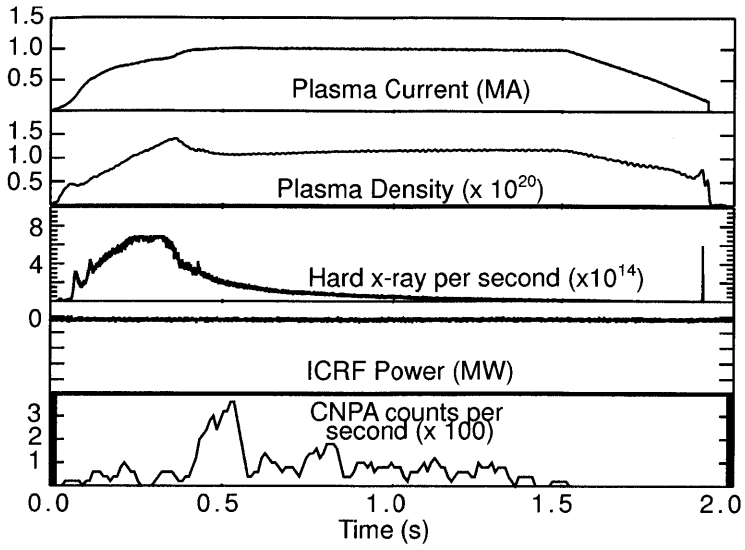

Figure 3-1: Plasma parameters and CNPA signal for a discharge with no RF power where the CNPA detects photon counts.

3.1.2 Threshold determination

A noise threshold needs to be determined in order to differentiate fast-ion impacts from noise. This threshold can either be manually set or automatically determined. In the automatic determination routine, the noise level for each time bin is determined by considering the excursions below the mean. The dominant noise sources are symmetric about the mean signal level, while all pulses from fast-ions occur above the mean. By considering only the negative excursions, we estimate the maximum noise level, and thus a suitable threshold level. However, threshold finding is not active at times when the ICRF antennas are not operating, so that the spurious spikes that often appear at plasma start-up or disruption are not included. An example showing the results of the threshold finding routine during a short ICRF pulse is shown in Figure 3-2. The discharge shown has quiescent noise. However, in noisier discharges there are often time bins with considerable noise excursions above the threshold value. These time bins are withheld entirely from the analysis.

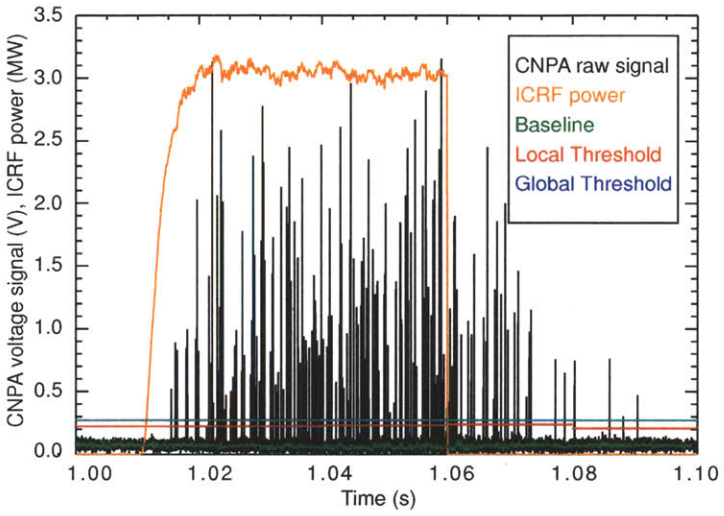

Figure 3-2: Illustration of the automatic threshold detection routine. Shown in black is the data from the digitizer. Shown in orange is the ICRF signal. The green trace is the average baseline. The red line is the noise threshold level for each 20 ms time bin. The blue line is the automated noise threshold level used for the entire discharge.

3.1.3 Peak finding routines

The CNPA signal is digitized by a D-Taq CPCI digitizer at 10 MHz for 1.5 seconds on every discharge. For 9 channels, each discharge produces ~140 MB of data per discharge. The analysis routines are designed to reduce the total amount of data by extracting the energies of incoming fast-ions and the times at which they impinged on the detectors. This is performed with a 'peak finding' routine which determines all local maxima above a threshold value while accounting for the fluctuating soft x-ray baseline.

To obtain the baseline level, all points above the noise threshold are temporarily set to the signal average, and the resulting trace is smoothed over a time region that is much larger than an individual event time, but much smaller than the baseline variation time. In all discharges presented in this thesis, we have used a smoothing time of 1 ms.

After the baseline is obtained, the original signal heights are calculated by subtracting the baseline from the values of the local maxima. These heights are then converted to energy based on the results of the energy calibrations described in Appendix B.

If two fast-ions impinge on the detector within 1 μs of each other, the two peaks will add together and each signal will contaminate the other. These "pileup" counts are rare, but when they occur, both peaks are removed from analysis. Also, there are occasional extremely energetic fast-ions that are above the maximum detectable energy level. The event signals from these ions have peaks with flattened or ragged tops. These extremely energetic fast-ions are very rare using the new modified energy range described in Section 2.2.1, but are similarly removed from the analysis.

3.1.4 Sources of uncertainty

There are several sources of uncertainty in calculating the binned energy distribution. Three of these sources of uncertainty arise from the conversion between detector signal

and fast-ion energy. The largest source of uncertainty is the systematic error from the calibration. This uncertainty is discussed in Appendix B and arises from differences in the calibration results for two separate calibrations. The other two sources of uncertainty are random errors. The dominant random error arises from the binning of the signal pulse heights in energy. Binning is necessary in both energy and time in order to obtain suitable statistics. Larger bins provide better counting statistics but also give rise to larger errors in the particle energy. In general this uncertainty is lower than the uncertainty from the calibrations. The third uncertainty arises from the pickup fluctuations. Most of the discharges analyzed in this thesis have very low uncertainty from pickup fluctuations. However, there are discharges where this uncertainty is very large. These uncertainties are all included in the horizontal error bars in the energy spectra. If the analysis routines were to forgo baseline subtraction, the introduced error would be approximately equivalent to the error due to calibration.

Typically in this chapter, vertical error bars represent the uncertainty due to counting statistics. In cases where the spectra have been smoothed for readability, these error bars show the spread in the data.

3.2 Fast-ion dependence on plasma parameters

In this section, basic results of the fast-ion distribution are presented, highlighting the correlations between the CNPA signals and various plasma parameters. Almost all of the CNPA signals presented in this section are binned distributions in both space and time. We also attempt to explain the plasma processes that govern the relationships. Characteristic error bars are included where applicable.

We attempt to bring out the dependence of the fast-ion distribution on plasma parameters by examining both direct comparisons of two discharges, and amalgamations of signals over many plasma discharges. Several of the discharges analyzed in this chapter for direct comparisons include data from discharges with modulated

ICRF. These discharges will be examined in more detail later. They are used here because the plasmas were designed to have ideal plasma conditions for fast-ion analysis. The amalgamated signals are determined by examining each 20 ms time bin over all plasma discharges with CNPA signal and classifying each time bin by density, plasma current, magnetic field and RF power. The count rates are normalized to be in units of counts per second per eV per cm^2 per steradian, in order to compare across discharges with different aperture settings. While, there are additional plasma parameters that affect the count rate, clear trends can be seen with respect to the three chosen parameters. Unless otherwise noted, all discharges presented in this chapter have magnetic fields between 5.2 and 5.4 T and have antenna operating frequencies of 80.5 MHz (E-antenna), 80 MHz (D-antenna), and 78 MHz (J-antenna).

3.2.1 Electron density

The relation between the fast-ion population and the plasma density is the simplest to understand. As discussed in Chapter 1, at energies above 13.5 T_e, ions primarily slow down on electrons. The collision frequency for hydrogen ions slowing down on electrons is the reciprocal of the slow down time given in Eq. 1.9,

$$\nu_{ie} = 5.1 \times 10^{-20} \frac{n_e \ln(\Lambda)}{T_e^{3/2}}, \tag{3.1}$$

where $\ln(\Lambda)$ is the Coulomb Logarithm and is typically around 15 for C-Mod parameters.

As can be seen from Equation 3.1, $\nu_{ie} \propto n_e$. At higher densities the collision frequency is higher, and therefore, fast-ions are less likely to become highly energetic.

Thus, we can expect two different effects from changes in electron density. At higher densities we expect to see a *lower effective temperature* of the fast-ions due to collisions with electrons. We also expect to see a *decreased number of fast-ions* that impact the detector due to both enhanced collision frequency and increased ionization

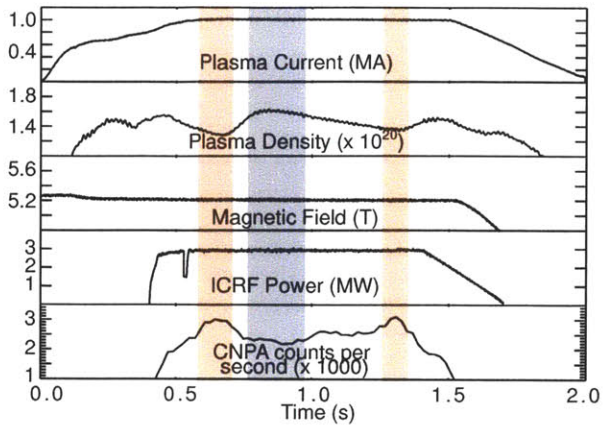

Figure 3-3: Shown is a single plasma discharge with a varying density. The CNPA count rates for ions > 200 keV are higher at low density (red shaded) and lower at high density (blue shaded)

between the location of neutralization and the detector. The ionization effect will be discussed later in Section 3.3.3.

Figure 3-3 shows a plasma discharge with a slowly varying density. As expected, the CNPA signal drops when the density increases.

To demonstrate the change in the fast neutral distribution arriving at the detector we examine the measured energy distribution from two plasma discharges with similar parameters (Figure 3-4). In order to educe the qualitative difference in the energy spectrum, we normalize the energy spectrum of the higher density discharge (dashed blue line in Figure 3-4) to the lower density discharge (solid red curve). Comparing this normalized curve to the lower density discharge, we see that the slope of the energy spectrum is steeper for the higher density discharge, indicating a lower effective temperature. This effect is more pronounced away from the resonance layer. Although the electron temperature is higher in the lower density discharge the stored energy (not shown) is the same in both discharges.

The amalgamated CNPA signals (Figure 3-5) show similar trends to the two-discharge comparison. Here we clearly see that the number of counts decrease as the

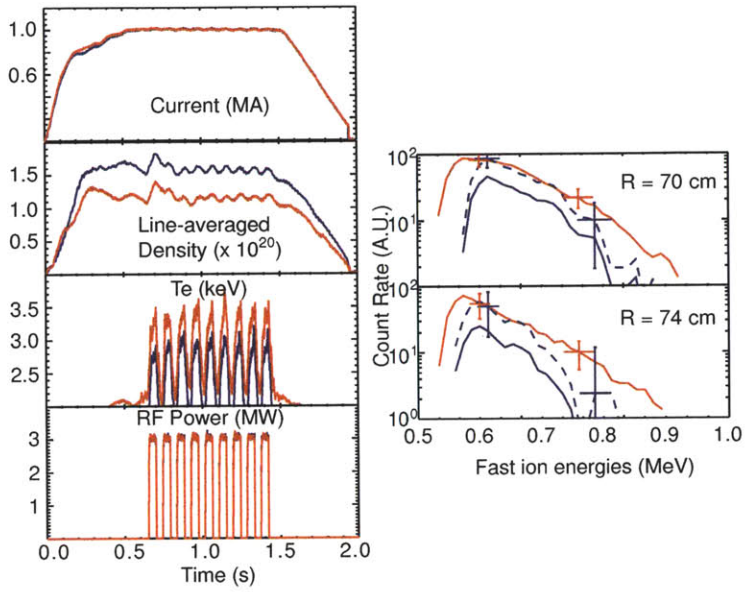

Figure 3-4: Shown are two plasma discharges with different densities. ON the right the CNPA signals are shown vs energy for two sightlines with characteristic error bars. One sightline is near the ICRF resonance ($R = 70$ cm) and one is away from the resonance ($R = 74$ cm). Normalized distributions (dashed blue) are also shown for comparison. The distributions are normalized so that the count rates for each channel are the same at 300 keV.

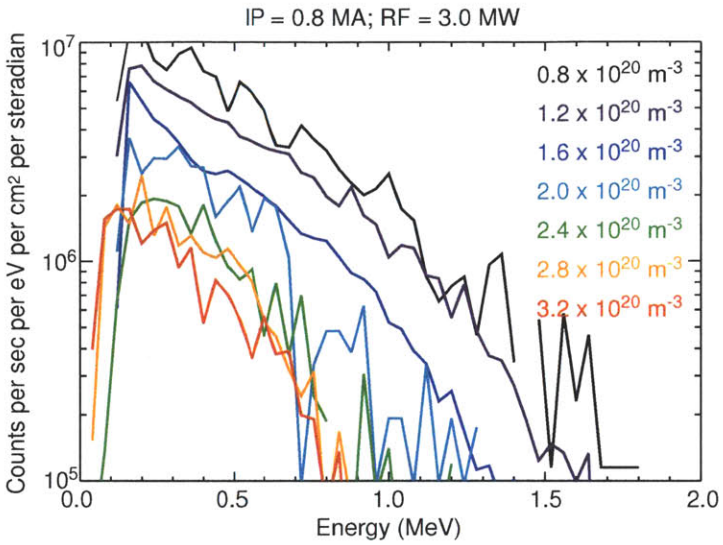

Figure 3-5: Shown are amalgamated CNPA signals summed over all time bins that had plasma currents between 0.75 and 0.85 MA and RF power between 2.75 and 3.25 MW.

electron density is raised. The relation between fast-ion temperature and electron density will be revisited later in this chapter.

3.2.2 RF power

The effect of changes in the ICRF power input into the plasma is more complicated. One might expect that increasing the ICRF power would increase both the count rate seen at the detector and the effective temperature of the fast-ions. This behavior is predicted by the standard Stix distribution [55].

Figure 3-6 shows results from two plasmas at the same density but different ICRF powers. The number of CNPA counts clearly increases when ICRF power is raised. However the fast-ion distribution appears to be significantly more energetic only on the sightline farther from the resonance ($R = 74$ cm). The sightline near resonance ($R = 70$ cm) shows a clear increase in the number of counts but a negligible difference in fast-ion energy. The relation is complicated because ICRF power tends to raise

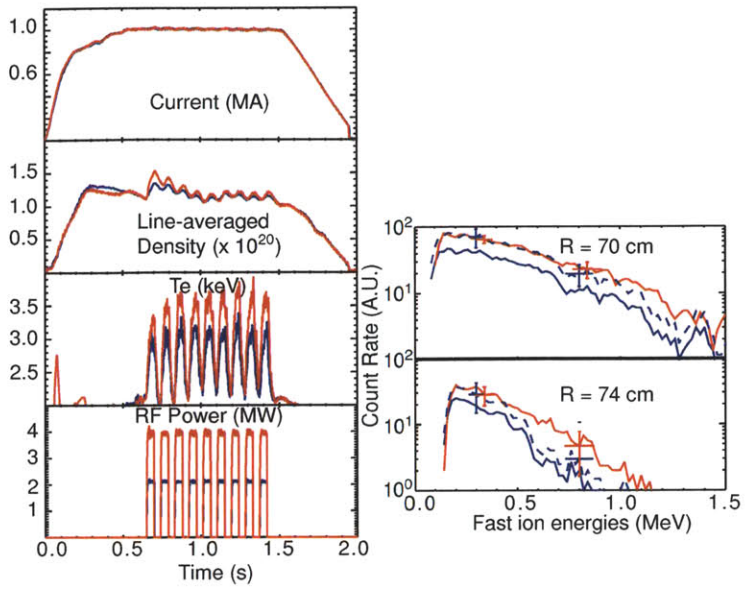

Figure 3-6: Shown are two plasma discharges with different RF powers. On the right CNPA signals are shown vs energy for two sightlines with characteristic error bars. One sightline is near the ICRF resonance (R = 70 cm) and one is away from the resonance (R = 74 cm). Normalized distributions (dashed blue) are also shown for comparison. The distributions are normalized so that the count rates for each channel are the same at 300 keV.

electron temperature significantly and the electron density slightly.

The amalgamated CNPA counts (Figure 3-7) show that the number of counts clearly increases with higher RF power, but it is less clear that the fast-ion temperature is increased. There appears to be a saturation of the signal after ~2 MW of ICRF power, with additional power not significantly increasing the tail temperature. We will revisit this result later in this chapter to determine the actual fast-ion temperature dependence on ICRF power, and again in Chapter 4, where we will examine what simulations predict as far as dependence on ICRF power.

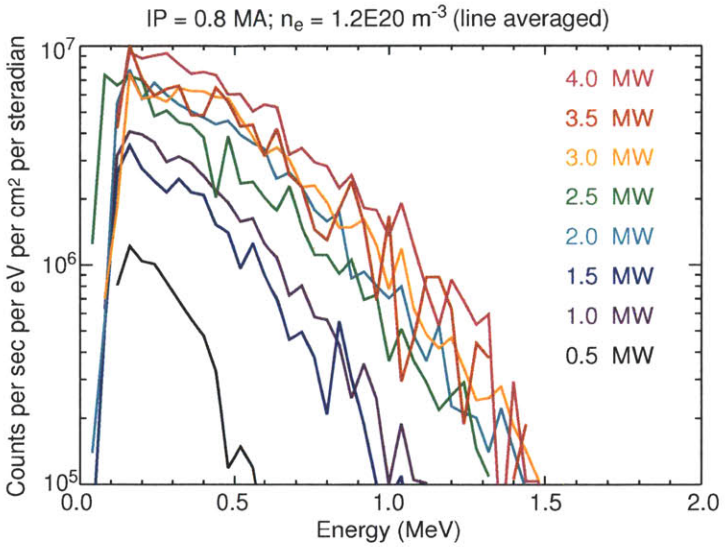

Figure 3-7: Shown are amalgamated CNPA signals summed over all time bins that had plasma currents between 0.75 and 0.85 MA and line-averaged electron density between 1.0 and 1.4 $\times$ 10^{20} m^{-3}.

3.2.3 Plasma current

As described in Section 1.1.3, the width of a banana orbit scales inversely with current. Therefore, at lower currents, we expect an increase in the fast-ion transport. Furthermore, at low currents some energetic ions may no longer be confined. Comparing discharges with similar parameters (see Figure 3-8) shows that fast-ion signal rates are indeed lower at lower currents. We also see that the lower current discharge generates less fast-ions at the higher energies, despite having a slightly lower density.

Again, the amalgamated discharges (Figure 3-9) produce the results seen on the two-discharge comparison. A clear increase of fast-temperature is seen over the current-scan. The dependence on current is an interesting result. If the dependence is due to banana widths, we might expect simulations that do not account for finite banana-widths to have difficulty reproducing the proper behavior with respect to plasma current. The fast-ion distribution's dependence on current will be exam-

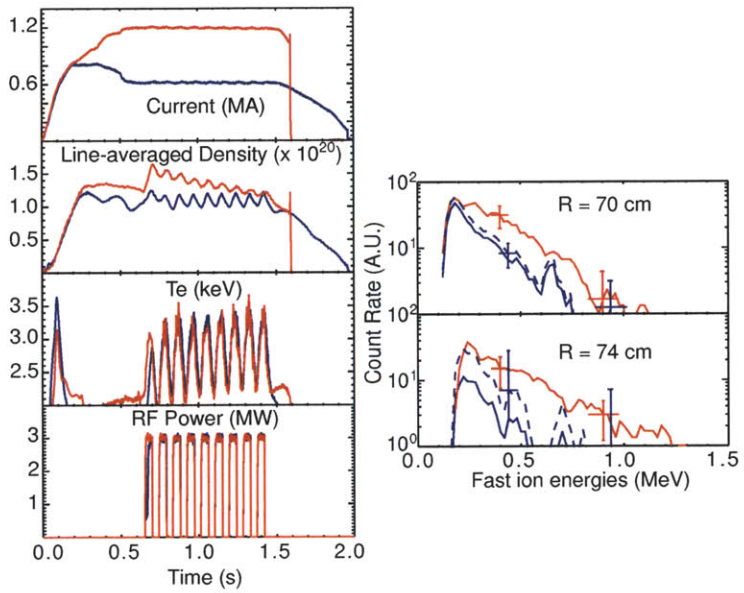

Figure 3-8: Shown are two plasma discharges with different plasma currents. On the right, CNPA signals are shown vs energy for two sightlines with characteristic error bars. One sightline is near the ICRF resonance ($R = 70$ cm) and one is away from the resonance ($R = 74$ cm). Normalized distributions (dashed blue) are also shown for comparison. The distributions are normalized so that the count rates for each channel are the same at 200 keV.

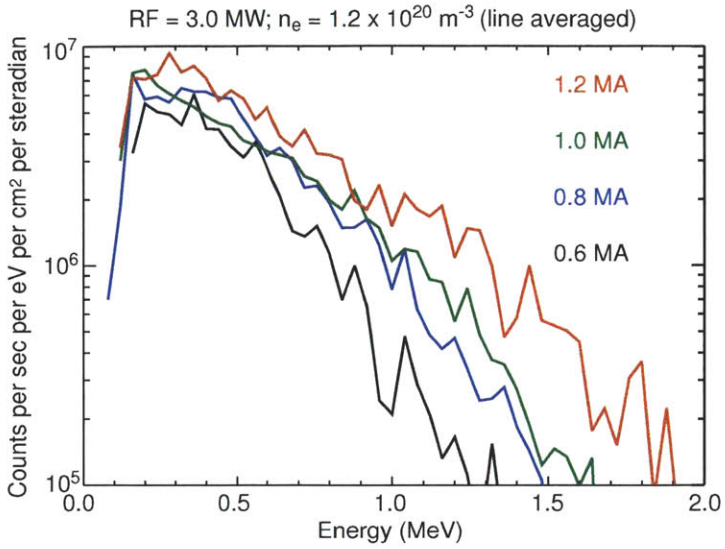

Figure 3-9: Shown are amalgamated CNPA signals summed over all time bins that had RF power between 2.75 and 3.25 MW and line-averaged electron density between 1.0 and 1.4 $\times$ 10^{20} m^{-3}.

ined in more detail later on in this chapter. Also, Chapter 4 will examine whether simulations can correctly model the dependence of the fast-ion distribution on plasma current despite zero-banana-width limitations.

3.2.4 Magnetic field

The location of the plasma resonance is dependent on the frequency of the ICRF antennas and the strength of the magnetic field. The location of the resonance in the absence of plasma is given by,

$$R_{\text{res}} = \frac{e}{m_p} \frac{B_0 R_0}{2\pi f}. \tag{3.2}$$

Where R_{res} is the location of the resonance, f is the frequency of the ICRF antenna and B_0 is the strength of the magnetic field at location R_0. By altering the magnetic field, the resonance can be moved. The location of the ICRF resonance layer in plasma

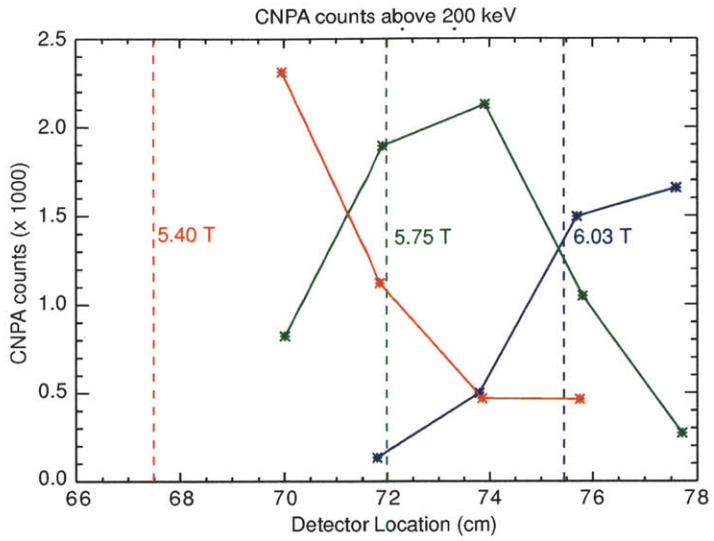

Figure 3-10: Shown here is the relation between the CNPA count rate and the magnetic field for three different magnetic field values. During this discharge only one ICRF antenna with a frequency of 80.5 MHz was operating and the location of the resonance is shown by the vertical dashed lines.

is ~1-2 cm outboard of the vacuum resonance due to the diamagnetic properties of the plasma. Figure 3-10 shows the CNPA counts on the detectors for three discharges at three different magnetic field values. The CNPA signal tends to peak slightly outboard of the resonance layer in the vacuum.

From Figure 3-10 we also see that few energetic ions have banana tips past R = ~75 cm for normal strength (5.4 T) toroidal fields. Therefore detectors that do not have a favorable line of sight (i.e. perpendicular to the magnetic field) at the resonance layer are unlikely to collect many ions. This also explains why count rates for the previous midplane horizontal NPA and CNPA views (see Section 2.1.1) were much lower in comparison to the current vertical views.

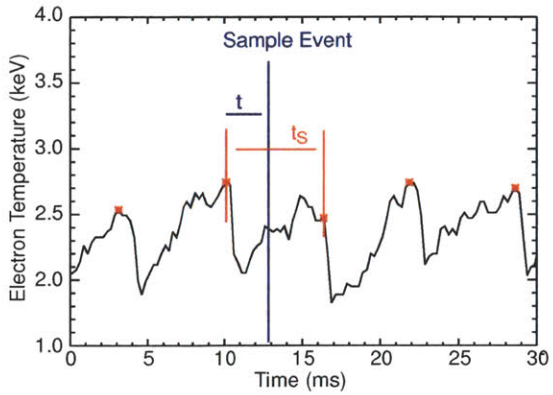

Figure 3-11: Sawtooth crash times are plotted in red and overlaid on the T_e signal. Also plotted is the location of a sample event relative to two sawteeth crashes and the relevant times for the calculations necessary in Figure 3-12.

3.2.5 Sawteeth

Previous work on PLT, TFTR and JET indicate that plasma sawteeth can cause fast-ions to be ejected from the plasma. Recent results from JET with fast-ion loss detectors indicate that the ejected ions are predominantly near the trapped-passing boundary [56]. This is a reasonable place for losses to occur because a small perturbation in pitch-angle can change a passing particle to a trapped particle, creating a large banana orbit, and causing the ion to be lost. At pitch angles far from the trapped-passing boundary, the fast-ion distribution should be relatively unaffected by the sawteeth. We can measure the CNPA dependence on sawteeth by timing each fast-ion count relative to the sawtooth crash (see Figure 3-11). That is, the event occurs at,

$$t_{\text{norm}} = \frac{t_{\text{real}} - t_i}{t_{i+1} - t_i}. \tag{3.3}$$

Here t_{norm} represents the normalized time. t_{real} is the CNPA event occurrence in real time, and t_i and t_{i+1} are the time of the sawteeth crashes such that $t_i < t_{\text{real}} < t_{i+1}$. The results shown in Figure 3-12 show that the CNPA signal is not affected by plasma sawteeth.

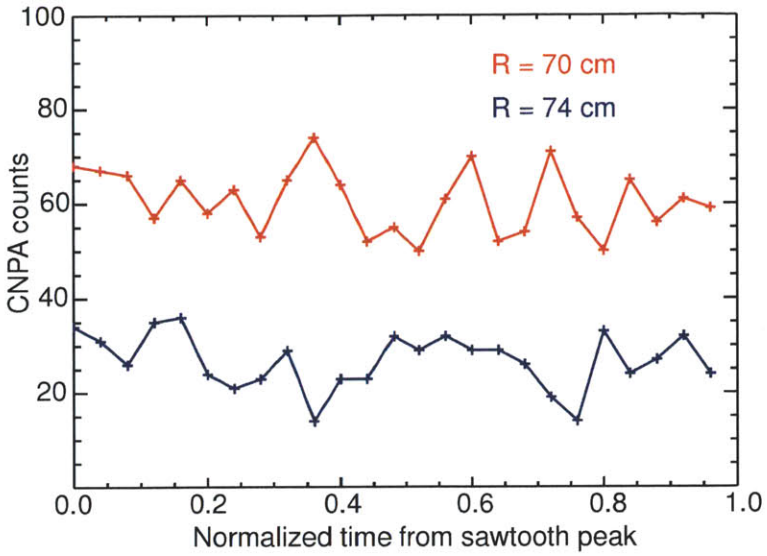

Figure 3-12: CNPA signal is plotted vs normalized time relative to sawteeth crashes. The results show no dependence of the CNPA signal on sawteeth.

3.2.6 Operating regime

H-mode (high confinement mode) is a specific operating regime accessible on C-Mod, and other tokamaks where a strong thermal and particle barrier exists at the edge of the plasma. H-mode particle transport and the associated transport and energy barriers are subjects of current research [57], but will not be explored in this thesis. However, for completeness, the behavior of the fast ion distribution during these regimes will be briefly examined.

H-mode plasmas tend to have high densities, often twice as high as L-mode (low confinement) discharges. All the discharges shown in previous sections are from L-mode plasmas. Because the signal at the CNPA detectors is anti-correlated with particle density, there are fewer energetic ions generated in H-mode plasma discharges. H-Mode plasmas also have better particle confinement. Therefore, for energy balance purposes, these plasmas have significantly higher radiation. In order to prevent saturation of the detectors from photons (see Section 3.1.1), a small aperture setting

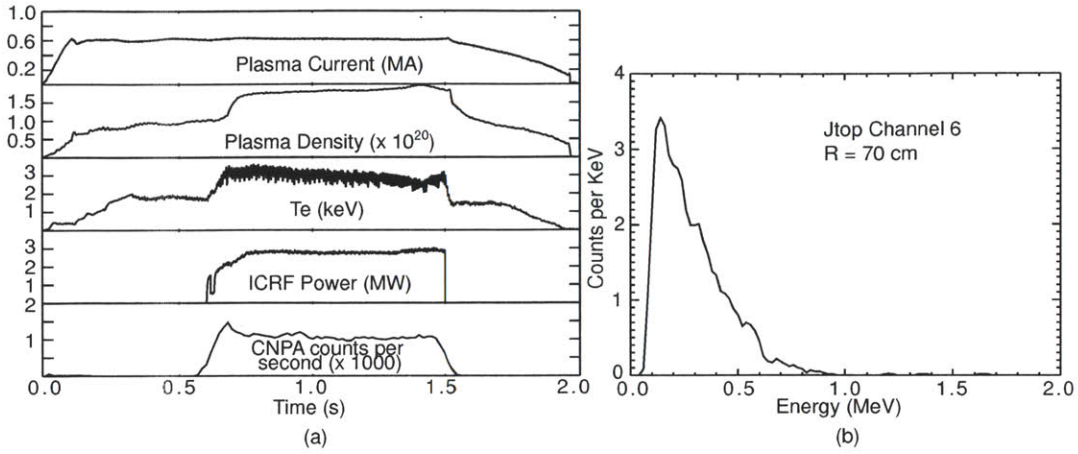

Figure 3-13: (a) The CNPA signal along with various plasma parameters are shown for an H-mode plasma. (b) The fast-ion energy spectrum for the CNPA sightline with peak signal.

must be used. The lower fast-ion energies combined with the requirement to reduce the aperture make H-Mode plasmas difficult to diagnose.

Nevertheless it is possible to obtain fast-ion signals for H-Mode plasmas that have relatively lower densities. Figure 3-13a shows the CNPA signal during a low density, low current H-mode plasma. The energy spectrum for the sightline with peak signal is shown in Figure 3-13b.

The I-mode (Improved L-Mode) regime is a recently discovered operating regime on C-Mod, where thermal confinement is the same as in H-mode but particle confinement is the same as in L-mode [58]. These plasmas do not exhibit a large density increase, and while there is some increase in radiation, I-mode plasmas are less radiative than H-mode plasmas.

I-Mode plasmas on C-Mod have created some of the highest energy fast ion tails seen to date, likely due to the large amounts of RF power coupled into the plasma without the density rise that accompanies H-Mode plasmas. Figure 3-14a shows the plasma parameters for a high performance I-mode plasma and Figure 3-14b shows the energy spectrum for the CNPA sightline of peak absorption. The very energetic fast-

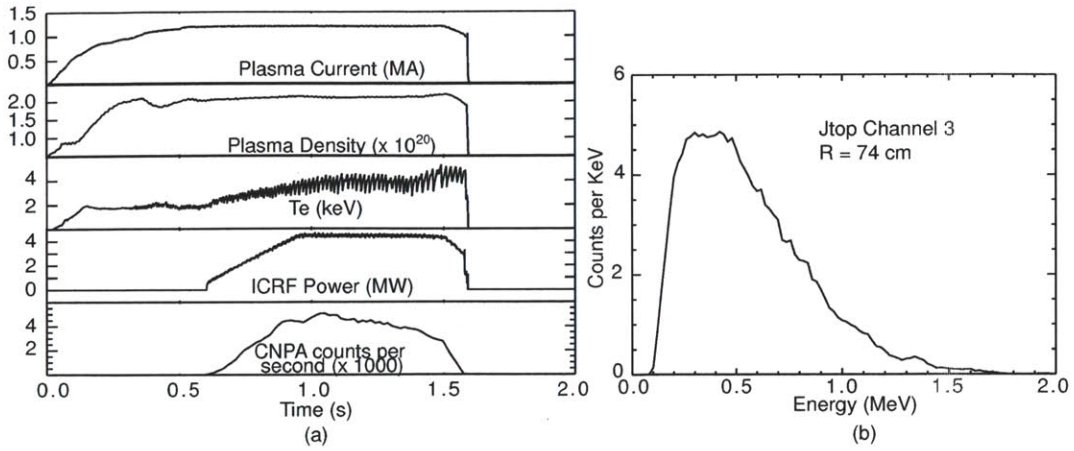

Figure 3-14: (a) The CNPA signal along with various plasma parameters are shown for an I-mode plasma. (b) The fast-ion energy spectrum for the CNPA sightline with peak signal.

ion tail in this plasma is interesting in light of the relatively high plasma densities. In general it is unclear whether there is a difference between fast-ion behavior in I-Mode and L-Mode, and this area may warrant further investigation.

3.3 Effective temperature at the detector

In Section 3.1 we discussed how to determine the energetic ion distribution at the detector. Several of these distributions have already been presented (e.g. Figures 3-13b 3-14b). We will attempt to characterize each distribution by a single parameter which we will call the effective temperature of the energetic ion tail, or T_{eff}. In order to determine trends in the effective temperature of the energetic ions we will compare the results across a range of plasma discharges.

The effective temperature at the detector is estimated assuming that the fast-ion distribution can be represented as,

$$\frac{f_{\text{det}}(W)}{T_{\text{eff}}} = \frac{df_{\text{det}}}{dW}. \tag{3.4}$$

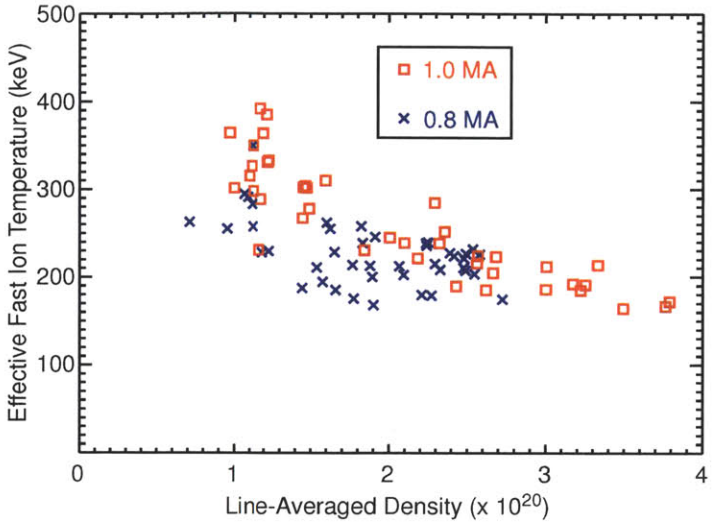

Figure 3-15: Effective fast-ion temperature at the detector as a function of electron density for two current values.

The solution for the distribution function is then:

$$f_{fi,\mathrm{det}}(W) = f_0 \exp^{-W/T_{\mathrm{eff}}}, \tag{3.5}$$

where f_{det} is the distribution of the fast-ions at the detector, and a function of energy W.

The results for the effective temperature calculated at the detector are shown below in Figures 3-15 and 3-16 as functions of electron density and plasma current respectively. These bear out the trends that we have previously noted, namely that the fast ion temperature decreases with increasing density and that the fast ion temperature increases with increasing current. Only plasma discharges at 5.4 T and normal antenna operating parameters were considered. However, these discharges covered a range of ICRF input powers.

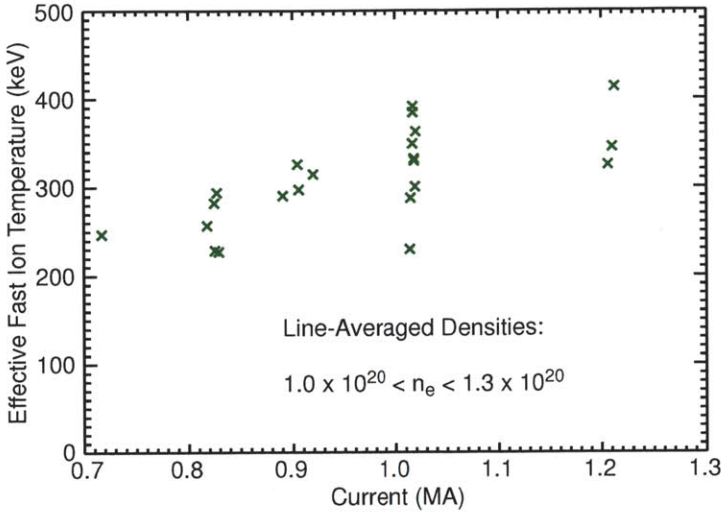

Figure 3-16: Effective fast-ion temperature at the detector as a function of plasma current for low density plasmas.

3.3.1 Fast-ion neutralization

In order to convert the fast-ion signal at the detector to the fast ion distribution in the plasma, we must correctly evaluate the relevant neutralization and re-ionization rates. Neutralization rates determine the flux of neutrals out of the plasma. Ionization rates determine the probability that the fast neutral reaches the detector. Calculating these rates requires the knowledge of cross-sections for both electron capture and ionization reactions. Unfortunately, for the energy ranges that we are interested in, there are no experimental data and often relatively few theoretical estimates. Furthermore, to calculate the total neutralization rate, the density profiles of the relevant species also need to be known. However, there are limited measurements for several of these densities, and they will need to be estimated as well. Despite these difficulties, we will attempt to calculate the neutralization and ionization rates as a function of fast-ion energy as best as possible. This section and the following two sections will deal with neutralization, density calculation, and ionization, respectively.

The first step on a fast-ion's path towards the CNPA is neutralization. The fast-ion

needs to neutralize in order to travel freely across magnetic field lines. Fast-ions are confined by the magnetic field but fast neutrals are free to move in any direction. All discharges described in this thesis have a deuterium majority, a hydrogen minority, and boron as a dominant impurity. In these plasmas, the possible neutralization reactions are,

$$H^+ + D^0 \rightarrow H^0 + D^+. \tag{3.6a}$$

$$H^+ + B^{4+} \rightarrow H^0 + B^{5+}. \tag{3.6b}$$

$$H^+ + e^- \rightarrow H^0 + \gamma. \tag{3.6c}$$

Equations 3.6a and 3.6b are charge-exchange interactions. Eq. 3.6c is electron-ion radiative recombination. Eq. 3.6a represents charge-exchange with background deuterium majority and Eq. 3.6b represents charge-exchange with the hydrogen-like state of the dominant impurity. In all three reactions there is negligible energy or momentum transfer between the reactants. Therefore, knowledge of the escaping neutral represents knowledge of the fast proton immediately prior to neutralization.

To evaluate each of the neutralization reactions for C-Mod plasmas, we need to have cross-sections for proton energies ranging from 100 keV to 1 MeV. CNPA count rates above 1 MeV are generally low, if they exist at all. In all ion-ion interactions, the charge donor can be considered to be thermal. For these charge-exchange interactions, $W_{\text{donor}} << W_{\text{H,fast}}$, and the fast proton can be considered to be moving relative to a stationary donor.

The recombination case is more complicated. However, to simplify, we use the approximation that electron velocity is much larger than fast-ion velocity, $v_e >> v_{fi}$. In this regime, the recombination cross-section is solely a function of electron temperature. This assumption is valid as long as $W_{fi} \ll (m_p/m_e)W_e$ or $W_{fi} \ll 1836 \times W_e$. Where W_{fi} is the fast-ion energy and W_e is the electron energy. In other words, for a standard C-Mod plasma with electron temperature of 2 keV, this

assumption is valid for fast-ions below about 4 MeV.

Cross-section for charge-exchange with neutral deuterium

Cross-sections for charge-exchange with neutral deuterium have not been studied in detail. Charge-exchange cross-sections are dependent on the difference between the velocity of the ion and the velocity of the bound electron. Therefore, the deuterium charge-exchange cross sections do not differ significantly from cross-sections for charge-exchange with hydrogen [59], which are well known. The sources used here for charge-exchange with neutral hydrogen can be found from Janev and Smith [60] up to 10 MeV. Although there are cross-sections available for charge-exchange into various n-states, only charge-exchange into the $1n$ state covers the full energy range of interest.

Cross-section for charge-exchange with B^{4+}

The charge-exchange cross-section of fast protons with B^{4+} is difficult to obtain. There are no experimental data in the appropriate energy range, due to the difficulty of the experiment. The estimation of the cross-section for charge-exchange with boron is given from an adjusted Strong Potential Born approximation and is described in detail in Appendix C.

Radiative recombination

In addition to the charge-exchange reactions, fast-ions can be neutralized by recombination with the bulk electrons. The dominant recombination process with electrons is radiative recombination. To calculate the reaction rate for radiative recombination, we will assume that the electrons are moving faster than the ions, as mentioned above.

In this case the reaction rate can be written from Equation 6.3.5 in Hutchinson [61]:

$$\langle \sigma_{rn} v \rangle = \bar{g}_n 5.2 \times 10^{-20} Z \left(\frac{\chi_n}{T}\right)^{3/2} \exp\left(\frac{\chi_n}{T}\right) E_1\left(\frac{\chi_n}{T}\right) \mathrm{m}^3\mathrm{s}^{-1}, \tag{3.7}$$

where

$$E_1(x) = \int_x^\infty \frac{\exp(-s)}{s} ds.$$

In Eq. 3.7, $\bar{g}_n$ is the Gaunt factor averaged over the Maxwellian electron distribution, Z is the atomic number, χ_n is the ionization energy for state n, and T is the electron temperature.

Comparison of different neutralization rates

The cross-section for charge-exchange with boron peaks at fast-ion energies around 600 keV. This is approximately where the fast-ion velocity corresponds to that of the $1s$ shell bound electron. We expect the presence of boron to play a significant role near this energy value. Exactly how much of a role the boron plays will be discussed in the next section, after we make estimations of the B^{4+} density. However, we can compare the cross-sections for the two charge-exchange processes directly (Figure 3-17). We see that the D^0 charge-exchange cross-section is significantly larger than the B^{4+} charge-exchange cross-section at energies below 1 MeV. In Figure 3-18, we compare the reaction rates for both charge-exchange processes and radiative recombination. The reaction rates for the charge-exchange processes are determined by multiplying the cross-section with the fast-ion velocity. Here we see that the recombination rate is significantly smaller than the charge-exchange rates. Thus, in order for recombination with electrons to be important there needs to be 10^7 - 10^8 more electrons in the plasma than either neutral deuterium or hydrogen-like boron (see Figure 3-21).

Principal quantum state

The energy shell that the fast-ion charge-exchanges into is important in determining the likelihood of re-ionization. Electrons in higher shells are more weakly bound and

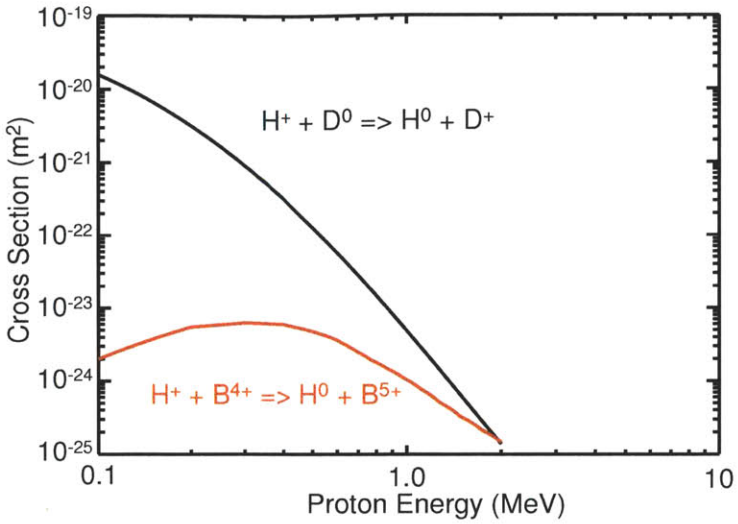

Figure 3-17: Comparison between boron and hydrogen charge-exchange cross sections. The curve for charge-exchange into D^0 is based on Janev [60]. For the cross-sections for the charge-exchange with boron see Appendix C.

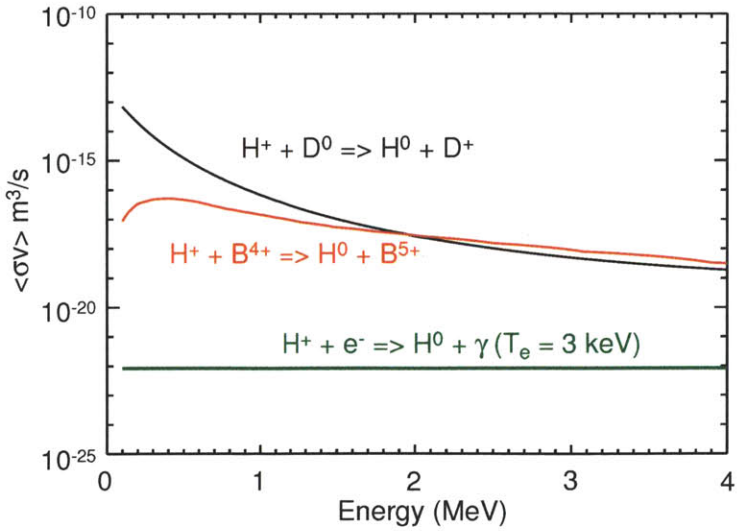

Figure 3-18: Reaction rates for charge-exchange with boron, charge-exchange with deuterium and recombination with electrons.

thus more likely to ionize.

The majority of charge-exchange ions will receive an electron into the $n = 1$ quantum state. The actual percentage varies depending on the reaction, but for the bulk of the energy range considered, $\sim 83\%$ of the fast-ions charge-exchange into the $1n$ shell [60, 62]. Similarly, using Equation 3.7 the electron will recombine into the $1n$ quantum state about 79% of the time.

3.3.2 Densities of species in the plasma

In order to calculate the rate of fast-ion neutralization, we need to have information on the densities of relevant species. In our case we need densities of neutral deuterium, D^0, hydrogen-like boron, B^{4+}, and the electrons. Only the electron density is directly measurable with the current diagnostics on C-Mod, so the neutral deuterium and hydrogen-like boron densities will need to be inferred. These results may have significant errors, but they give an order of magnitude estimate for each species.

The line-integrated electron density is one of the fundamental plasma measurements made on C-Mod. This measurement is made by two-color interferometry. (See Section 2.3). For density profiles, we use Thomson scattering for the electron density radial profile. (See section 2.3)

Although, a direct measurement of the amount of hydrogen-like boron in the plasma core is not feasible with the current diagnostic set, there are spectrometers on C-Mod that measure specific transitions of B^{4+} ions that have recently undergone a charge-exchange interaction. However, this signal is much stronger in the plasma edge than in the plasma core. Neutral beam injection can be used to enhance the core B^{4+} signal. Using neutral beam analysis techniques we can estimate the B^{5+} density by measuring the B^{4+} $n = 7 \rightarrow 6$ transition and comparing that spectral line to the D_α transition.

Nevertheless, due to weak beam penetration and highly fluctuating edge signals, it is difficult to obtain measurements of B^{5+} in the C-Mod plasma. Preliminary

analysis from active charge-exchange diagnostics on several discharges analyzed in this thesis estimate the core density at ~0.01% of n_e. Edge boron measurements on this discharge and previous discharges have estimated edge boron densities at ~1% of n_e [52]. In this chapter we assume core boron density of 1% of n_e. An upper bound on the B^{4+} is determinable from Z_{eff}. For the plasmas analyzed in this thesis, Z_{eff} ranges from 2 to 3. Using the lower estimate of $Z_{\text{eff}} = 2$ and assuming fully stripped boron is the sole impurity, the boron density is given by,

$$Z_{\text{eff}} = \frac{\sum n_i Z_i^2}{n_e} = \frac{(n_D + n_H) + Z_B^2 n_B}{n_e} = \frac{n_e - Z_B n_B + Z_B^2 n_B}{n_e}, \tag{3.8}$$

where we have invoked quasi-neutrality,

$$n_D + n_H + Z_B n_B = n_e.$$

Solving for n_B/n_e gives,

$$\frac{n_B}{n_E} = \frac{Z_{\text{eff}} - 1}{20} = 5\%. \tag{3.9}$$

Therefore, 5% should be viewed as the upper bound for the fully ionized boron density in the plasma.

Assuming we know the B^{5+} density, we estimate the B^{4+} density in the core of the plasma by calculating the ratio of $n_{B^{4+}}$ to $n_{B^{5+}}$. We assume the boron in the plasma is in coronal equilibrium. This means that the dominant mode of ionization is electron impact ionization, and the dominant mode of recombination is through radiative recombination. The ADAS database can provide reaction rates for radiative recombination and electron impact ionization [63]. These results are shown in Figure 3-19a, along with an extrapolation for the radiative recombination.

Comparing the rates gives us an estimate of the fraction of $n_{B^{4+}}$ in the plasma. The fraction is shown in Figure 3-19b as a function of the electron temperature. While it is likely that the electron impact ionization rate far exceeds any other ionization

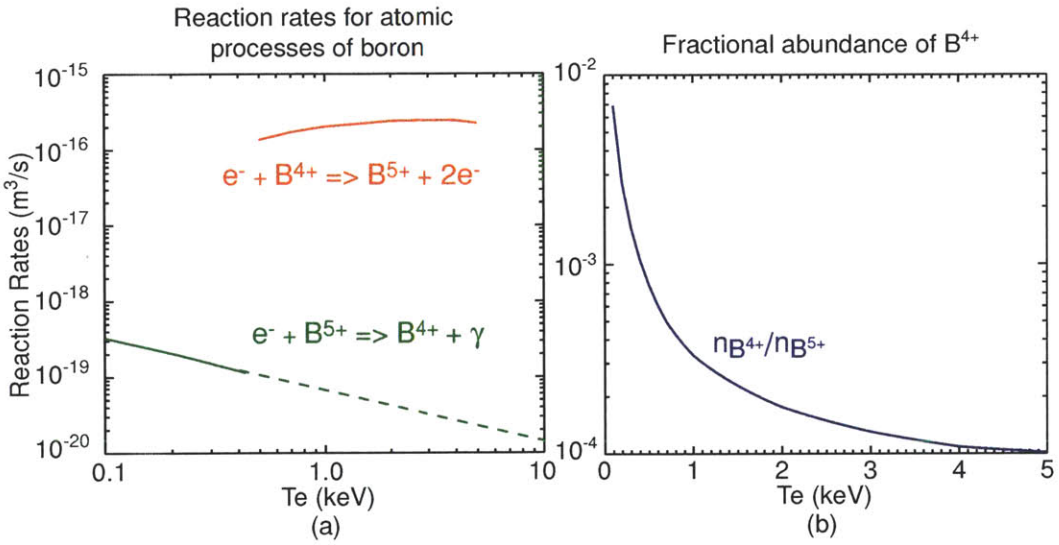

Figure 3-19: (a) Radiative recombination and ionization rates for B^{4+}. (b) Fraction of B^{4+} as a function of T_e

process, there may be other methods of recombination, for example charge-exchange. There also could be some amount of transport of B^{4+} from the edge, where it is much more abundant. The transport effect for boron should be far less pronounced than the effect from neutral deuterium because B^{4+} is charged and is thus prevented from moving directly across the magnetic field. In any case, the collisional equilibrium result given in Figure 3-19 should be seen as a lower bound, and the actual B^{4+} density may be higher.

To estimate the neutral deuterium density in the plasma, two processes need to be considered. First, we need to consider the collisional equilibrium density, as we did above for the hydrogen-like boron. Second, we need to consider the transport of neutral deuterium from the cold plasma edge. There are several models that we can use for the transport. For this thesis we use results from the FRANTIC module in TRANSP simulations [64]. These simulations provide both the collisional equilibrium density and the transport from the edge and these results are shown for a typical discharge in Figure 3-20. The transport from the plasma edge is the dominant contribution to the neutral deuterium density in the plasma, and there is some uncertainty with regards to the edge density. Nevertheless, the TRANSP estimate presented here is in agreement with previously measured neutral densities at the separatrix within a factor of 2 [65]. Computing the neutral deuterium density with TRANSP is time-consuming. Therefore, for the simple analysis presented in this chapter, we will assume a characteristic neutral density. However, all the simulations featured in Chapters 4 and 5 have full neutral density profiles from TRANSP simulations.

Reactions per second

The densities for the three species of interest (electrons, neutral deuterium and hydrogen-like boron) are shown in Figure 3-21a for a typical C-Mod plasma. The densities are given as a function of normalized major radius. The B^{4+} density is larger than the D^0 density over the majority of the plasma. This fact, along with

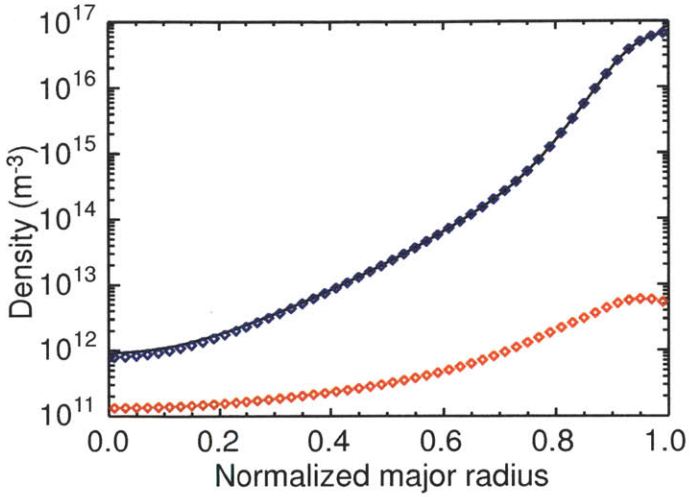

Figure 3-20: Densities of neutral deuterium from TRANSP. The transport from the plasma edge (blue) is larger than that due to collisional recombination (red).

the peaking of the B^{4+} charge-exchange reaction at ~600 keV make charge-exchange with hydrogen-like boron the dominant neutralization process above ~300 keV. This is evident in 3-21b where the reaction rates multiplied by the species density are shown for all three species. These plots show the densities for the three species at $r/a = 0.3$.

3.3.3 Ionization

Once a fast-ion is neutralized it needs to reach the detectors while still neutralized. If the fast neutral becomes re-ionized, it will be reabsorbed into the plasma and is considered 'lost.'

For ionization, we need to consider both electron impact ionization, ion impact ionization, and charge-exchange with D^+. A more detailed calculation also considers multi-step excitation-ionization processes, in which the bound electron is excited to a higher principal quantum state and subsequently ionized.

An accurate calculation of the ionization probability will take into account the

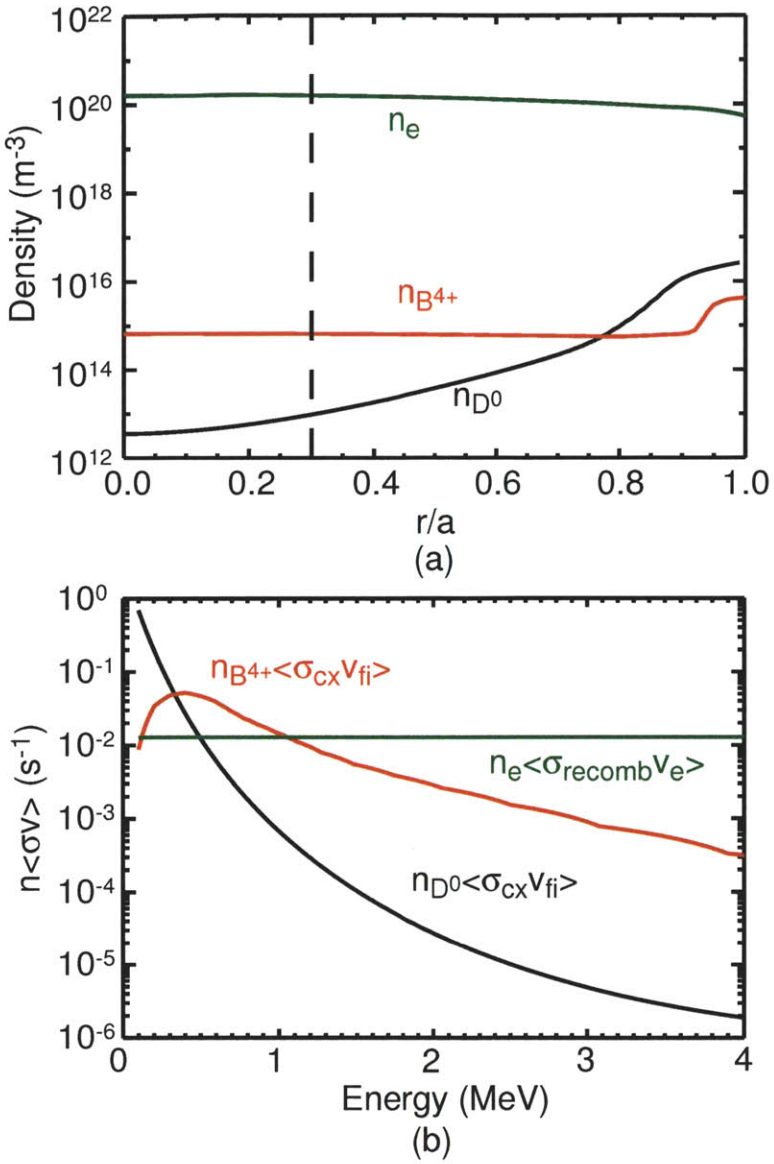

Figure 3-21: (a) Densities for e^-, D^0, and B^{4+} as a function of normalized major radius for a typical C-Mod plasma. The dashed line indicates the densities used to calculate the second plot. (b) $n\langle\sigma v\rangle$ for e^-, D^0, and B^{4+} as a function of fast-ion energy.

proper initial starting state. This is difficult to estimate properly but not impossible. However, instead of calculating the full ionization from first principles, we will use a beam attenuation model.

The ionization cross-sections used in this thesis have been taken from a paper by Janev et al. [66]. This paper provides empirical formulas for the attenuation of a hydrogen neutral beam and accounts for all the ionization processes listed previously as well as charge-exchange and ionization by impurity ions. It also accounts for excitation, and calculates the n-state distribution up to $n = 99$.

In a homogeneous plasma, the distribution of n-states will reach equilibrium after some distance. In this case, the beam intensity can be written as,

$$\frac{dI}{dx} = -n_e \sigma_S I, \tag{3.10}$$

where I is the intensity of the beam, n_e is the electron density and σ_S is the beam stopping cross-section. Janev et al. calculate σ_S for a variety of plasma species and provide empirical fitting formulas.

Janev does not give a method for calculating the characteristic distance at which the beam n-state distribution equilibrizes. However, we will use the Janev cross-sections with the caveat that the Alcator C-Mod plasma is unlikely to be slowly varying enough that the initial distribution of states is non-negligible.

Once the Janev cross-section, σ_j for ionization has been determined, we can estimate the mean free path for fast-ions in the plasma,

$$\lambda_{\text{mfp}} = \left(\sigma_j n_e\right)^{-1}. \tag{3.11}$$

The shine-through, or fraction of ions that escape the plasma is then calculated by integrating along the path from the fast-ion neutralization point, z_0 to the detection point, z_{det}.

$$A\left(W, z_0\right) = \int_{z_0}^{z_{\text{det}}} \exp\left(\frac{-z}{\lambda_{\text{mfp}}(E, z)}\right) dz. \tag{3.12}$$

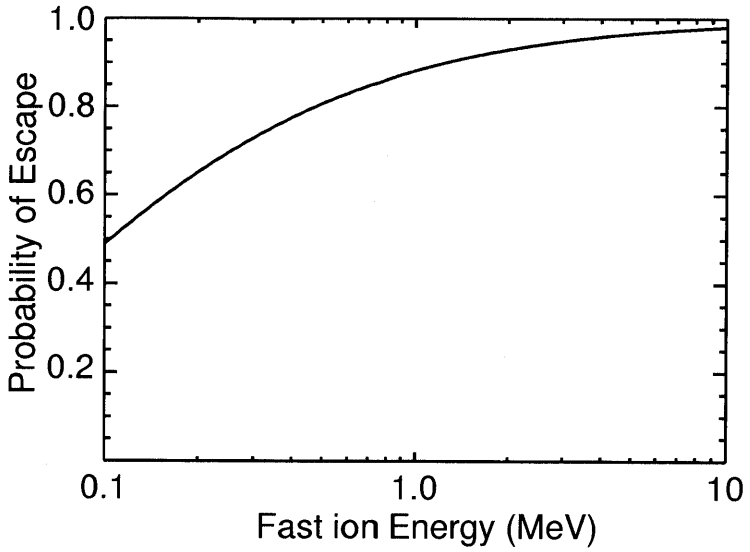

Figure 3-22: The probability of escape for a neutralized fast-ion is plotted against fast-ion energy for a 2 keV plasma with $n_e = 1.5 \times 10^{20}$.

Figure 3-22 shows the probability of escape as a function of ion energy for fast-ions in a 2 keV plasma with electron density of 1.5×10^{20}.

3.3.4 Simple fast-ion distribution calculation

Using our estimations of the neutralization of fast-ions at a given point in the plasma, and the probability of ionization of the fast ion, we can calculate the fast-ion distribution in the plasma. The flux at the CNPA detector is given by,

$$\Gamma(W)\,dW = v_0^2 dv_0 \epsilon \int_l A(x,\vec{v_0})\, f_{fi}(x,\vec{v_0}) \left[\sum_s \sigma(v_0)\, v_0 n_s(x)\right] dl. \tag{3.13}$$

In Equation 3.13, $\Gamma(W)$ represents that flux of particles per unit energy per second that arrive at the detector. This, multiplied by dW, gives the flux per second at the detector between energy W and $W + dW$. In the R.H.S. v_0 represents the velocity of the a fast-ion with energy W. $A(x,\vec{v_0})$ represents the attenuation of fast-ions. It

is a unitless factor that represents the probability that an ion moving at velocity v_0 will escape the plasma if it starts from position x. ϵ is the etendue, and is equal to the area of the aperture multiplied by the solid angle of acceptance f_{fi} is the fast-ion distribution and satisfies

$$\int f_{fi}\left(x, \vec{v_0}\right) d^3v d^3x = n_{fi}. \tag{3.14}$$

In other words, f_{fi} is the probability that a fast-ion is found at a specific energy and location. $\sigma\left(v_0\right)$ is the cross-section for one of the reactions of interest. Technically the velocity argument should be $v_{rel} = |v_{fi} - v_s|$. However, for the fast-ions studied here, the neutrals can be considered motionless compared to the fast-ions, and the fast ions are motionless compared to the electrons. For the ions we assume that $v_0 \approx v_{rel}$ and for electrons we integrate over a Maxwellian as described in Section 3.3.1. $\sigma\left(v_0\right)$ multiplied by v_0 is the rate function. Multiplying this rate by the density, n_s, of the specific species, s, gives the number of charge-exchange reactions per second with that species. Summing over all species gives the total number of charge exchange and recombination reactions, or in our case, fast-ion neutralizations. The units on both sides of the equation are time^{-1}.

Estimation of fast-ion distribution in the plasma

To calculate the distribution of fast-ions at the pitch-angle viewed by the CNPA, one needs some information about the spatial distributions of both the fast-ions and the electron-donor species. These cannot be obtained from any direct measurements because inversion procedures are impossible in the presence of highly anisotropic signals. The CNPA measurements can be used as a constraint or validation mechanism for simulation codes that can calculate the full distribution function of the fast-ions, and this is the method we use in the next chapter. However, in the remainder of this chapter, we obtain an estimate of the fast-ion tail temperature *in the plasma* by making some simplifying assumptions. First, we will assume that all the fast-ions are born near the center of the plasma. Simulations show that most ICRF energy is

deposited in the inner third of the plasma, so this is a reasonable assumption.

Assuming all fast-ions are born at a single location, the distribution function looks like,

$$f_{fi}\left(\vec{x},\vec{v_0}\right) = f_{fi}\left(\vec{v_0}\right)\delta(\vec{x}-\vec{x_0}), \tag{3.15}$$

and the integration over space can be carried out. The point x_0 is taken to be 2 cm above the midplane, although the results presented here are not sensitive to changes of x_0 on the order of 5 cm.

Solving for $f_{fi}(\vec{v_0})$ gives,

$$f_{fi}(\vec{v_0}) = \frac{\Gamma(W)dW}{\sum_s \left[n_s \sigma v_0\right] A(W)\epsilon L_c v_0^2 dv_0}. \tag{3.16}$$

where the new parameter L_c represents the size of the region over which the fast-ions are formed. Together with the etendue ϵ, these represent the volume over which the fast-ion population is integrated over. We will make one more assumption for simplicity. We assume that the dominant mode of neutralization is charge-exchange with boron over the energy range of 250 keV to 1 MeV.

Calculating an effective temperature of the fast-ion tail

We fit the fast-ion distribution between 250 keV and 1 MeV with a single exponential. It is also possible to use a Stix distribution fit [55] , but the Stix fit does not provide an improved fit over the distributions considered. A sample distribution fit is shown in (Figure 3-23). Exponential fits are convenient because they allow for an easy estimation of a fast-ion temperature. As in the detector fitting, the argument of the exponential is taken as the effective temperature (see Equation 3.5).

We first show the results of temperature fits applied to the plasma discharges previously studied in Figures 3-15 and 3-16. These are shown in Figures 3-24 and 3-25. In these figures a clear trend of T_{eff} with respect to electron density is seen. Similarly a trend with respect to plasma current is noticeable as well. However, both

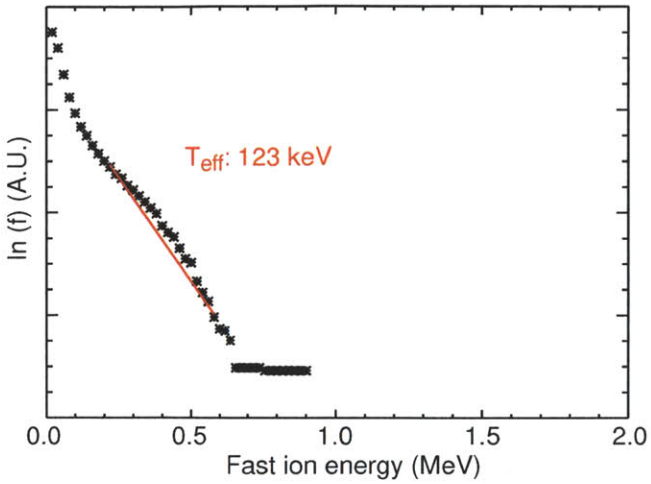

Figure 3-23: Effective temperature fits for a typical fast-ion distribution. A double exponential fit is used and the effective temperatures for the low energy and high energy regions are included. The distribution comes from a 0.9 MA plasma with line-averaged n_e of $\sim 1 \times 10^{20}$ m^{-3}.

plots show significant scatter of the temperature results indicating that there could be significant effect from other plasma parameters.

It is also possible to fit the amalgamated distributions in the same manner that we fit individual plasma discharges. In general each of these distributions have more data points in the fitting region than in individual discharges, improving statistics. Trends are shown for effective temperature scaling with respect to plasma density (Figure 3-26), plasma current (Figure 3-27), and RF power (Figure 3-28). The dependences on plasma density and plasma current are as expected, although the scatter is considerably less. There is no statistically significant trend with respect to RF power.

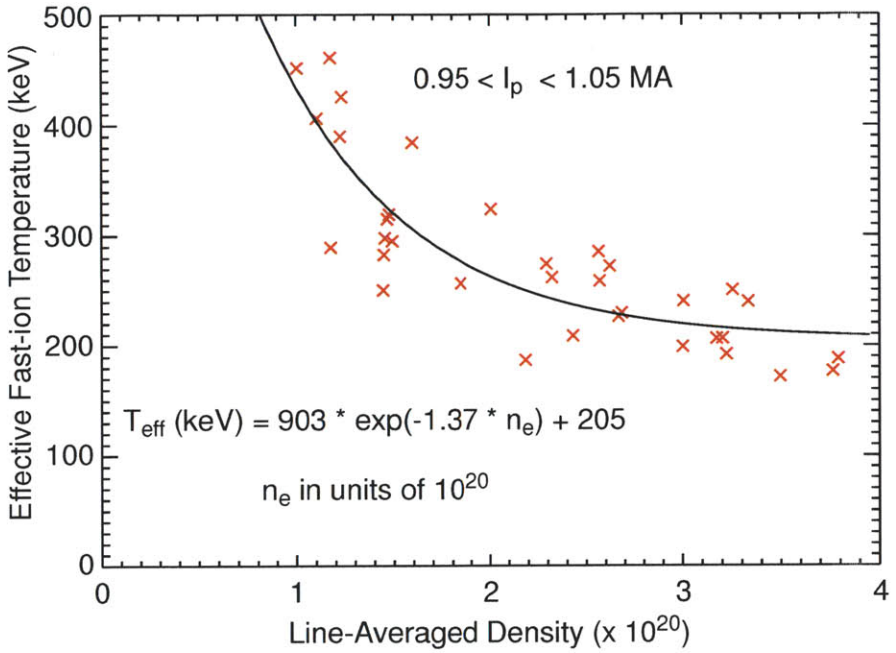

Figure 3-24: Effective temperature of the plasma as a function of plasma density for plasma currents between 0.95 MA and 1.05 MA. An exponential fit for T_{eff} as a function of density is also shown.

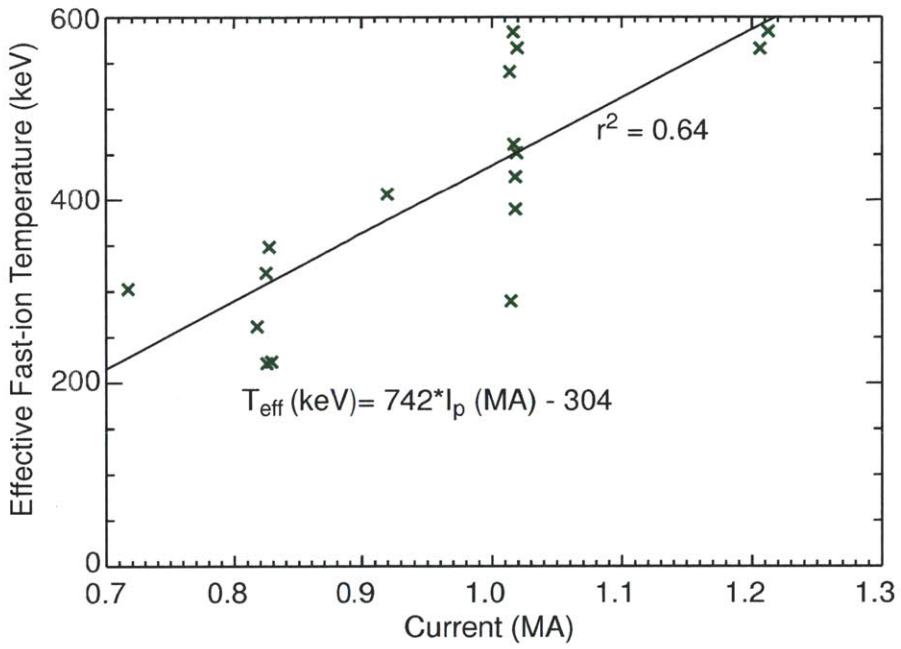

Figure 3-25: Effective temperature of the plasma as a function of plasma current for line-averaged electron density between 1.0 and 1.4 $\times$ 10^{20} m^{-3}. A linear fit for T_{eff} as a function of current is also shown.

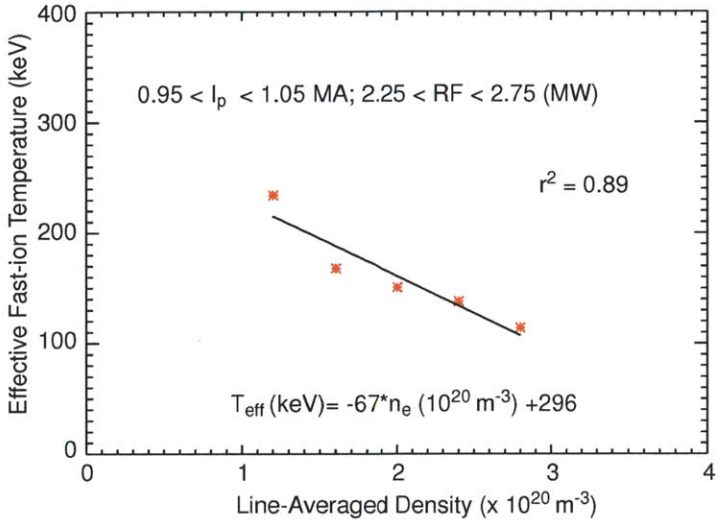

Figure 3-26: Effective temperature of amalgamated CNPA signals as a function of line-averaged electron density for plasma currents between 0.95 and 1.05 MA and RF power between 2.25 and 2.75 MW. A linear fit for T_{eff} as a function of density is also shown.

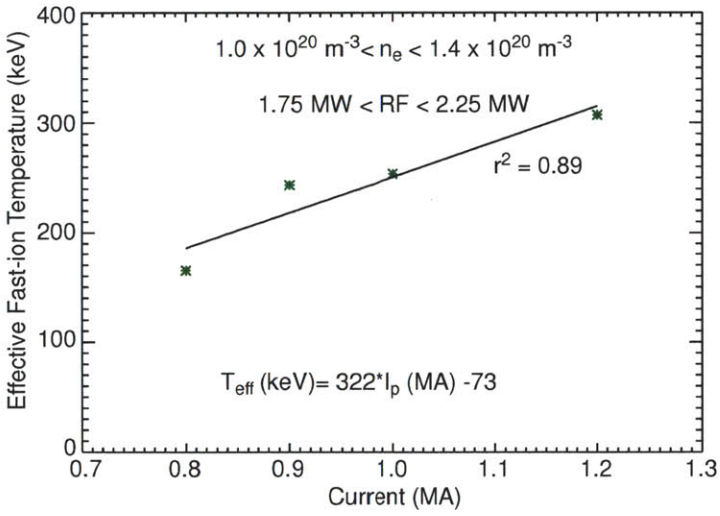

Figure 3-27: Effective temperature of amalgamated CNPA signals as a function of plasma current for RF power between 1.75 and 2.25 MW and line-averaged electron density between 1.0 and 1.4 $\times$ 10^{20} m^{-3}RF power between 2.25 and 2.75 MW. A linear fit for T_{eff} as a function of plasma current is also shown.

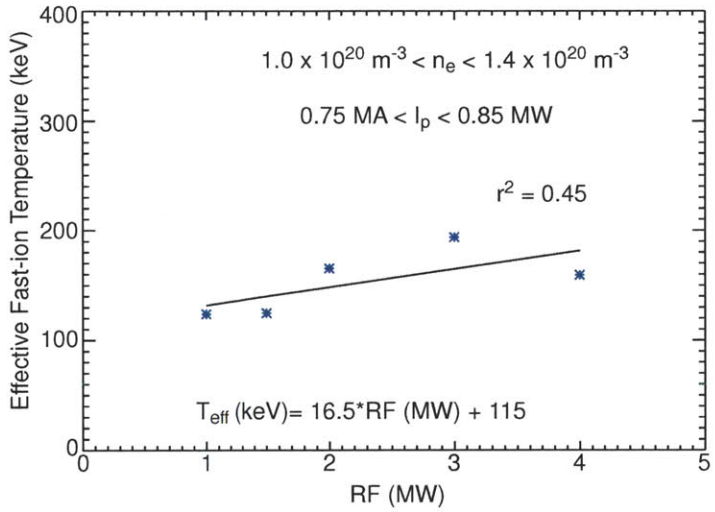

Figure 3-28: Effective temperature of amalgamated CNPA signals as a function of RF power for plasma currents between 0.75 and 0.85 MW and line-averaged electron density between 1.0 and 1.4 $\times$ 10^{20} m^{-3} A linear fit for T_{eff} as a function of RF power is also shown.

Chapter 4

Simulation: Steady-State

In the previous chapter, we qualitatively examined the fast-ion distribution and used some simplifying assumptions to estimate the fast-ion distribution in the plasma. A more thorough analysis requires the use of simulations that evolve a fast-ion distribution based on plasma and machine parameters. With these simulations we can solve for the flux at the detector directly and compare with the experimental measurements without the simplifying assumptions made in Chapter 3. Furthermore, the CNPA diagnostic can only sample specific chords in both phase space and position space, because of machine limitations. Thus, in order to obtain the minority ion distribution across the full plasma and over the full energy spectrum, we require the use of simulations. This chapter will focus on introducing these codes (Sections 4.1 - 4.3) the synthetic diagnostic (Section 4.4), and showing results for steady-state, $df/dt = 0$ (Section 4.5). Chapter 5 will focus on the evolution of the fast-ion distribution when $df/dt \neq 0$.

4.1 Simulation codes

The codes used for this simulation are the Fokker-Planck code, CQL3D, and the full-wave solver, AORSA. This section provides an overview of some of the other

simulation codes available and then describes AORSA and CQL3D in more detail.

4.1.1 History of ICRF wave-plasma simulation

The first analytic models of ICRF plasma distributions generated by ICRF waves were calculated by Stix in his seminal work on minority heating [55]. In his doctoral thesis, Hammett derived improvements to Stix's model by generalizing to two dimensions and introducing a bounce-averaged RF operator [67]. Hammett coupled his RF operator to a bounce-averaged Fokker-Planck code to create FPPRF. FPPRF was used for analysis on C-Mod and other machines for minority heating fast-ion distributions. [2, 68, 69]. Further development coupled FPPRF to the axisymmetric full-wave code TORIC [70]. This coupling was used to model mode conversion flow drive [71, 72] and internal transport barrier formation [73]. These codes were predominantly developed in the U.S., through combined efforts at Princeton, MIT and IPP-Garching.

Early research by Eriksson et al. used the wave-solver LION [74] to measure the deposition profile of ICRF heated ^{3}He in JET [75] by comparing LION predictions with neutrons from fusion events. LION employed a circular cross-section, did not include mode-conversion and enforced a constant $k_\parallel$. Results concluded that the codes accurately predicted the shape of the deposition profile, but incorrectly estimated the magnitude. Later work by Eriksson coupled the LION code to a Fokker-Planck code that allowed the fast-ion profiles to evolve in time [18]. The code compared the simulated distribution to the fast-ion distribution in JET estimated by D-D neutron products and by measuring anisotropies in stored energy. The code succeeded in predicting the rise of the neutron and anisotropy signal in the period after the ICRF turned on. Finite orbit effects were added in the Fokker-Planck code FIDO [76]. Simulations coupling FIDO and LION were used to simulate parasitic ion absorption of electron waves [77] and showed the effects of including ion transport and finite orbit effects in interactions between high harmonic fast waves and neutral beam ions.

Contemporary efforts involved coupling the Fokker-Planck code CQL3D to the

full-wave spectral solver AORSA [78], which are both described in more detail below. The simulated distributions from the coupled codes were compared to fast-ion distributions from the F-Top CNPA by V. Tang [2]. Simulations and experimental data were found to be in good agreement for low power, steady-state plasmas. At roughly the same time, a similar comparison was made on the Large Helical Device (LHD), where relative comparisons between experimental results in He plasmas from natural diamond detectors (NDDs) were compared to simulations using the GNET Monte-Carlo code coupled with the TASK/WM wave solver [29]. These results showed good relative agreement, although there was no attempt at an absolute comparison. Current efforts on LHD involve comparisons between an updated 5-D GNET code and experiments, although these have yet to be published as of the completion of this thesis [79]. With increases in computing power, Monte-Carlo codes have been developed in recent years, such as ORBIT-RF [80] and SMC [81]. These codes have been coupled to AORSA by an RF "kick" operator. Results have been obtained comparing results from ORBIT-RF and AORSA with measured distributions from DIII-D and NSTX and have indicated the importance of finite orbit effects in order to reproduce FIDA signals [82].

4.1.2 CQL3D

CQL3D (Collisional/Quasi-linear 3D) is a Fokker-Planck solver that was originally developed as the CQL code by G.D. Kerbel and M.G. McCoy [84], and later modified by R.W. Harvey and M.G. McCoy [85]. The code dates back to the mid 1980s but is continually updated. Most relevantly, the code has been updated in 2010 to include a synthetic neutral particle analyzer diagnostic.

The plasma simulated by CQL3D can include both multiple Maxwellian species as well as multiple non-Maxwellian species. In this way, CQL3D can calculate the evolution of a plasma species heated by auxiliary plasma heating. In our case, we are interested in the non-Maxwellian minority hydrogen ions heated by ion cyclotron

heating.

In order to solve for the distribution function, CQL3D makes use of several assumptions. First, the code assumes that distribution functions are evenly distributed toroidally. A second assumption is that particles have a uniform distribution in velocity space about the magnetic field lines. These two assumptions immediately change a 6D problem into a 4D problem. A third assumption is that the particle bounce time over a banana orbit is small compared to the collision time. Ions in C-Mod tend to have bounce times on the order of μs and collision times on the order of ms. However, if electromagnetic wave fields are strong enough to modify the ions significantly in a single bounce time, this condition is violated. The bounce averaging allows for another dimensional reduction to 3D. The dimensions used by CQL3D are therefore: normalized radius, $\rho = r/a$; W, the particle kinetic energy; and μ, the magnetic moment.

There is a limitation in CQL3D, in that currently all calculations except the orbit-loss calculation (Section 4.5.4) are done assuming both particle gyroradii and banana widths are zero. These assumptions are not well satisfied for the class of particles we wish to analyze (see Figure 1-4). Methods of generalizing CQL3D to finite banana widths and gyroradii are currently being developed but were unavailable for the analysis work presented in this thesis.

CQL3D solves the full Fokker Planck equation,

$$\frac{df}{dt} = \nabla_{\vec{u}} \cdot \vec{\Gamma}_{\vec{u}} + R(f) + S. \tag{4.1}$$

Writing the LHS. of Eq. 4.1 in terms of the kinetic energy and magnetic moment gives,

$$\frac{df}{dt} = \frac{\partial f}{\partial t} + \vec{v}_{\rm gc} \cdot \frac{\partial f}{\partial \vec{r}} + \frac{\partial f}{\partial \mu}\frac{\partial \mu}{\partial t} + \frac{\partial f}{\partial W}\frac{\partial W}{\partial t}, \tag{4.2}$$

where $\vec{v}_{\rm gc}$ is the velocity of the particle guiding center. By averaging over a bounce time we can reduce the 2D spatial dependence to a single dimension defined by the

point on the banana orbit where the field is minimal, ρ. The simplified Fokker-Planck equation actually solved by CQL3D is,

$$\frac{\partial f}{\partial t} + \left\langle \frac{qE_{\|}}{m} \frac{\partial f}{\partial u_{\|}} \right\rangle = \langle \mathrm{RHS} \rangle \,, \tag{4.3}$$

where q is the particle charge, $E_{\|}$ is the electric field parallel to the magnetic field, m is the particle mass, and $u_{\|}$ is the particle momentum per mass. For non-relativistic particles, $u_{\|} = v_{\|}$, the particle velocity parallel to the magnetic field. Lastly, the angled brackets, $\langle\rangle$, represent bounce averaging. Bounce averaged quantities are defined by,

$$\langle Q \rangle \equiv \frac{\oint Q ds/|v_{\|}|}{\oint ds/|v_{\|}|} \tag{4.4}$$

where the integral $\oint ds$ is taken over the particle orbit.

Turning our attention to the RHS of Eq. 4.3, we can express the divergence of the particle flux in velocity space as the sum of three variables,

$$\nabla_{\vec{u}} \cdot \vec{\Gamma}_{\vec{u}} = C(f) + Q(f) + H(f) \,. \tag{4.5}$$

Here, $C(f)$ is a Coulomb collision term, $Q(f)$ is the RF quasi-linear diffusion operator, and $H(f)$ is a term that accounts for synchrotron radiation. In the simulations presented in this thesis, the quasi-linear term is computed in AORSA, and is given in Appendix A.4. Synchrotron radiation is not relevant for ions and is not discussed further here. The other terms on the RHS of Eq. 4.1 are the radial diffusion term, $R(f)$, and the particle source/sink term, S. The RF quasi-linear term, the radial diffusion term and the coulomb collision term are the most relevant for this thesis, and we will provide a brief explanation of these terms here.

The RF quasi-linear operator describes the transfer of power from ICRF waves to plasma particles [86, 87]. The coefficients for this operator are determined with a separate full-wave solver or ray-tracing code. These coefficients are passed to CQL3D,

which evolves the distribution function by providing energy kicks to resonant particles. For minority heating, the RF operator only operates on particle orbits that pass through the ICRF resonance layer, and all the kicks increase perpendicular velocity only.

The quasi-linear approach is only valid when successive energy changes for each particle are decorrelated. This implies that the energy change for each particle is small compared to the particle energy over a bounce time. Furthermore, kicks to particle velocity must be small enough that particle orbits are not significantly perturbed over a bounce period. If these conditions are not satisfied, the quasi-linear approach is invalid. The plasma discharges presented in this thesis include regimes where quasi-linear theory may be invalid, providing a test of the code's performance (See Section A.2).

The radial diffusion operator is an adjustable parameter in CQL3D. By varying radial diffusion we can apply anomalous diffusion to the fast-ions. For radial diffusion, CQL3D includes both a diffusion term, D, and a convective term, $\vec{V}$. The general equation for particle diffusion is given by,

$$\frac{\partial f}{\partial t} = -\nabla \cdot D\nabla f + \nabla \cdot \vec{V} f. \tag{4.6}$$

In CQL3D, the diffusion term D is input into the code and can vary with particle energy and spatial location. CQL3D then calculates $\vec{V}$ so that the calculated plasma profiles are consistent with the input profiles.

The collision operator governs the classical slowing down and relaxation of the plasma species. In the absence of any radial diffusion operators or RF fields the evolution of the plasma species is governed entirely by this collision operator, and the distribution functions evolve according to the equations discussed in Section 1.3.1.

Lastly, in the CQL3D simulations presented in this thesis, particles that have orbits that take them out of the plasma boundary are considered lost. This represents a particle sink that removes very high energy particles with large banana width orbits.

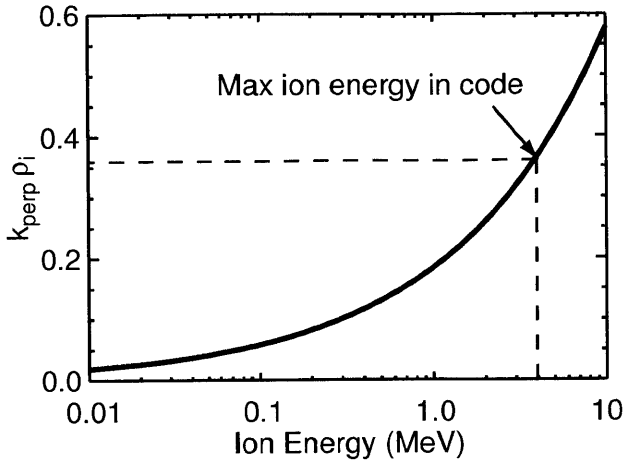

Figure 4-1: $k_\perp \rho_i$ vs. fast-ion energy.

The discussion of orbit losses is discussed in Section 4.5.4.

4.2 AORSA

AORSA (All ORders Spectral Algorithm) is a code that calculates the integral form of the solution to the wave equation in the presence of a general non-Maxwellian plasma distribution function [88]. The code is capable of solving the wave equation for arbitrary ion-cyclotron harmonic number and to all orders of $k_\perp \rho_i$, where $k_\perp$ is the perpendicular wave number and ρ_i is the ion Larmor radius. A plot of $k_\perp \rho_i$ as a function of ion energy is shown in Figure 4-1 for typical C-Mod parameters. The non-Maxwellian distribution functions simulated in this thesis includes fast-ions up to 4 MeV where $k_\perp \rho_i \approx 0.36$ and thus the finite Larmor radius assumption of $k_\perp \rho_i \ll 1$ is only marginally satisfied. Therefore, the calculation done by AORSA is an improvement over full-wave solvers which use finite Larmor radius expansions for the conductivity operator.

AORSA calculates the quasi-linear RF operator in three steps. The first step calculates the plasma conductivity kernel, $\sigma\left(f, \vec{r}, \vec{r'}, t, t'\right)$ from a user-defined distri-

bution function, f. Next the perturbed electric fields are calculated via the inhomogeneous wave equation (see Equation A.21 for comparison),

$$-\nabla \times \nabla \times \vec{E} + \frac{\omega^2}{c^2}\left(\vec{E} + \frac{i}{\omega\epsilon_0}\vec{J}_p\right) = -i\omega\mu_0\vec{J}_{\text{ant}}. \tag{4.7}$$

Here, $\vec{J}_{\text{ant}}$ represents a specified electrical current density due to RF antennas, and $\vec{J}_p$ is the plasma current that incorporates the non-Maxwellian plasma conductivity kernel,

$$\vec{J}_p(\vec{r},t) = \sum_s \int d\vec{r'} \int_{-\infty}^{t} dt' \sigma\left(f,\vec{r},\vec{r'},t,t'\right)\cdot\vec{E}\left(\vec{r'},t'\right). \tag{4.8}$$

Lastly, the code computes a quasi-linear operator from the perturbed electric fields (see Section A.4 [89]). This quasi-linear operator then gets passed to a Fokker-Planck solver (CQL3D in our case) to evolve a new distribution function.

AORSA can generalize to 3D by considering multiple toroidal modes. Simulation time scales linearly with the number of toroidal modes. Therefore, using multiple modes is costly computation-wise and the time-dependent simulations analyzed in the next chapter would have required concurrent execution of AORSA on a massively parallel platform with multiple toroidal modes, and were not feasible for this thesis. However, if the proper wave fields are desired, especially in situations where 3-D effects are important, using multiple toroidal modes is a necessity.

4.3 Iteration and convergence

As explained in a previous section, CQL3D evolves a distribution function based on quasi-linear RF coefficients obtained from AORSA. However, these coefficients are strongly dependent on the distribution function itself. Therefore, iteration between the codes is necessary to produce a self-consistent minority distribution [78]. The distribution function produced by CQL3D is passed back to AORSA where new coefficients for the RF quasi-linear operator are calculated. These coefficients are then

used to evolve a new distribution function in CQL3D. This process repeats until the distribution converges to a self-consistent solution.

There are two types of convergence. There is a convergence between consecutive iterations of each code individually and there is convergence between the outputs of both codes with each other. This second convergence requires a comparison between a parameter measured by both codes. Here, we use the power deposition profile for the convergence comparisons. Neither convergence on its own is sufficient and both need to be considered. The first convergence condition is satisfied if the nth iteration of CQL3D is the same as the $(n-1)$th iteration of CQL3D. If this is the case, further iterations will not alter the distribution functions more. Shown in Figure 4-2 are the power deposition profiles for four iterations of CQL3D. In the figure, there are significant changes between the first and second iterations, but smaller changes between subsequent iterations. Additional iterations (not shown) produce oscillatory behavior on order of the difference between the third and fourth iterations. Similar to the power deposition profiles, the plots of the synthetic diagnostic signal for sightlines near and away from the resonance displayed in Figure 4-3 show negligible difference between the third and fourth iterations.

In order to check the second convergence condition, the comparison between AORSA and CQL3D, we compare the power deposition profile as calculated by both codes. The result, shown in Figure 4-4, shows the comparison for both of these quantities for the final iteration of the coupled AORSA-CQL3D code. Here we see that for this simulation the deposited power predicted by CQL3D is slightly higher than that predicted by AORSA. It is not expected to recover better convergence between the coupled code than is shown in Figure 4-4.

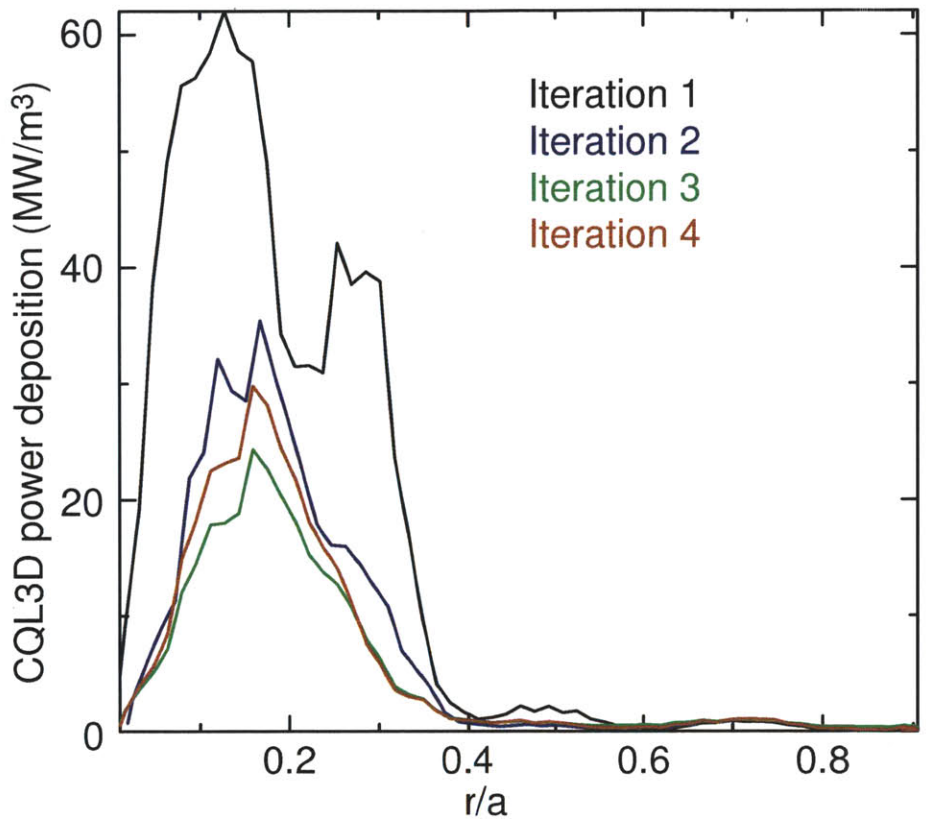

Figure 4-2: Comparison of absorbed power calculated for four iterations of AORSA-CQL3D.

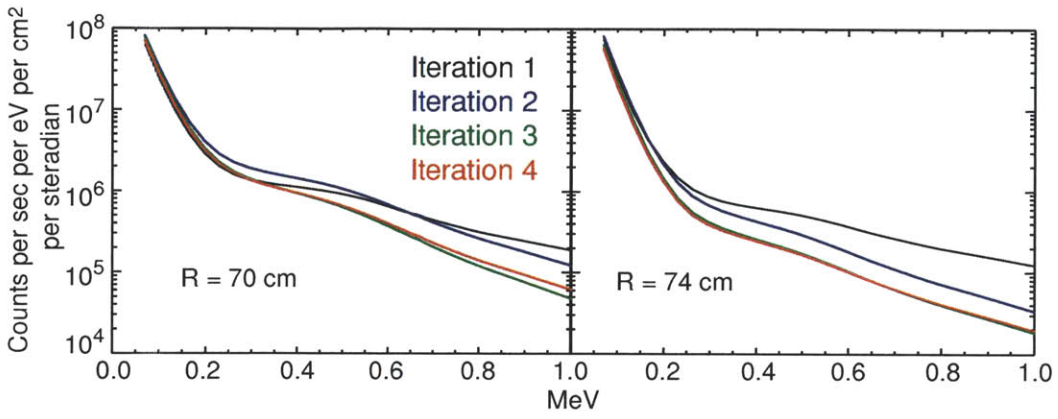

Figure 4-3: Comparison of synthetic diagnostic signals for four iterations of AORSA-CQL3D for a sightline near resonance (left) and away from resonance (right).

4.4 Synthetic diagnostic

We determine the flux to the detector by applying a synthetic diagnostic built into CQL3D to the simulated fast-ion distribution function. The defining equation to calculate the neutral flux is identical to Chapter 3. Eq. 3.13 and is repeated here for clarity,

$$\Gamma(W)\,dW = v_0^2 dv_0 \epsilon \int_l A(x,\vec{v_0})\, f_{fi}(x,\vec{v_0}) \left[\sum_s \sigma(v_0)\, v_0 n_s(x)\right] dl.$$

Unlike Chapter 3, we do not require the fast-ion distribution to be a delta function in space. Rather, we use the distribution function as calculated by the simulations and then use that distribution to calculate the flux directly. The energy dependent, absolute count rate is calculated for each synthetic diagnostic sightline and is then compared to the CNPA measurements. The inputs to the synthetic diagnostic are the CNPA sightlines and the electron donor species profiles. As discussed earlier, the species we consider are hydrogen-like boron and neutral deuterium.

The synthetic diagnostic follows a user-specified sightline through the three-dimensional

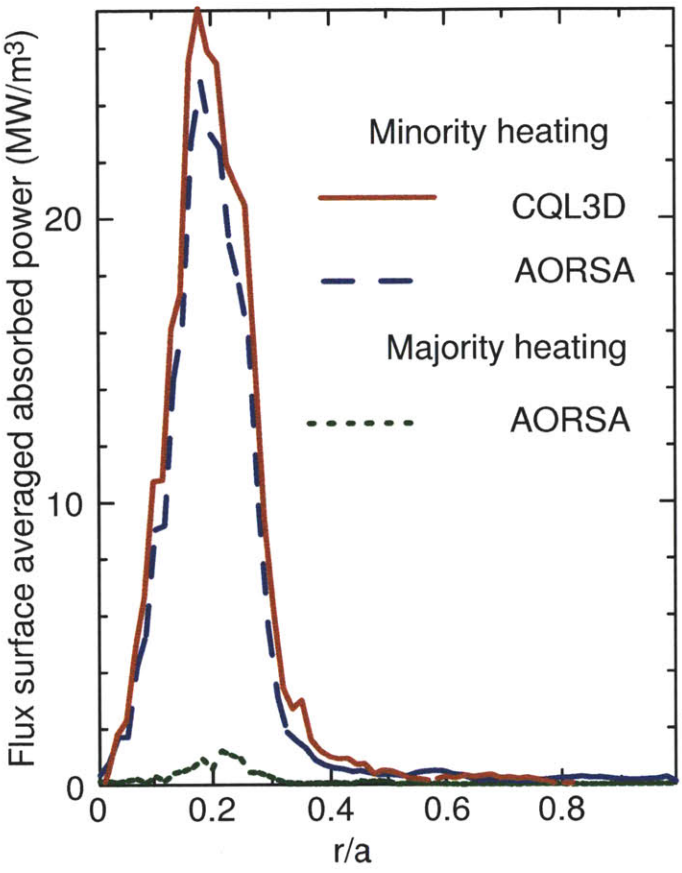

Figure 4-4: Comparison of absorbed power calculated by AORSA and CQL3D

plasma. A neutralized particle will leave the flux surface on a straight line traced onto a surface of a cone, determined by the ratio, $v_{\parallel}/v$. At each flux surface, the synthetic diagnostic determines the local pitch angle, ϑ, where the cone traced out by those particles contains the desired sightline. The local pitch angle, is defined in terms of the local velocity,

$$\cos(\vartheta) = v_{\perp}/v,$$

and thus can be related to the pitch angle at the midplane, ϑ_0, by using the adiabatic invariant,

$$\cos(\vartheta) = \frac{B}{B_0}\cos(\vartheta_0), \tag{4.9}$$

where B_0 is the magnitude of the magnetic field value at the midplane. For the CNPA geometry the sightlines intersect almost perpendicular to the magnetic field, so that particles with $v \approx v_{\perp}$ are selected.

CQL3D solves for the distribution function at the outboard midplane, f_0, in terms of three dimensions: the midplane radial value of the flux surface, the pitch angle at the midplane, and the total velocity, v. The density of particles between ϑ and $\vartheta + \Delta\vartheta$ and between v and $v + \Delta v$ at any point in the plasma is given by,

$$n = 2\pi \int_{\vartheta}^{\vartheta+\Delta\vartheta} \int_{v}^{v+\Delta v} f_0\left(R, v, \vartheta_0\right) v^2 dv \sin(\vartheta) d\vartheta. \tag{4.10}$$

The above equation can be written entirely in terms of the midplane pitch angles by using Eq. 4.9 and obtaining the following substitution,

$$\sin(\vartheta)d\vartheta = \sin(\vartheta_0)d\vartheta_0 \left(\frac{B}{B_0}\right)^{1/2}.$$

The density at any point in space is then described in terms of midplane coordinates only,

$$n = 2\pi \int_{\vartheta}^{\vartheta+\Delta\vartheta} \int_{v}^{v+\Delta v} f_0\left(R, v, \vartheta_0\right) \left(\frac{B}{B_0}\right)^{1/2} v^2 dv \sin(\vartheta_0) d\vartheta_0. \tag{4.11}$$

The factor $(B/B_0)^{1/2}$ is greater than unity away from the midplane and is largest at the banana tips for trapped particles. This factor accounts for the fact that particles have decreased parallel velocity near the banana tips and thus spend more time there.

The NPA synthetic diagnostic is based on a soft x-ray synthetic diagnostic already implemented in CQL3D The x-ray synthetic diagnostic is used in simulations of lower-hybrid driven plasmas which contain a significant number of fast electrons [90]. The sightline tracing and pitch angle calculations are identical. While it is difficult to benchmark the NPA synthetic diagnostic against known plasma parameters, the soft x-ray diagnostic can be compared to visible bremsstrahlung measurements in the absence of lower-hybrid driven fast electrons, and are found to agree.

The sensitivity of the CQL3D synthetic diagnostic was tested by varying several of the plasma parameters within their experimental errors. We aim to discover whether variation of plasma parameters produce uncertainties that are on the same order as the uncertainties in boron concentration or boron cross-section. Figure 4-5 shows the results for varying plasma density, plasma temperature, and hydrogen fraction within experimental errors. The experimental uncertainties used here are for a single data point and are dominated by random errors. The uncertainty over an ensemble of data points, such as those generated during long plasma flattops, are estimated to be significantly smaller.

Results of the sensitivity analysis show that the synthetic diagnostic predicts that the sightline near the resonance is relatively insensitive to changes of the plasma parameters, including the hydrogen fraction. These are shown in the left side of Figure 4-5. It should be noted that a strong dependence on hydrogen fraction appears at high minority concentrations (> 15 %) where the ICRF fast wave undergoes mode conversion to the Ion Cyclotron wave or the Ion Bernstein wave. However, simulations of these plasmas requires careful accounting of the mode conversion wave physics and require higher mode resolution [91]. In this thesis we limit the focus to plasmas in the minority heating regime where hydrogen fractions are < 10 %. Sightlines away

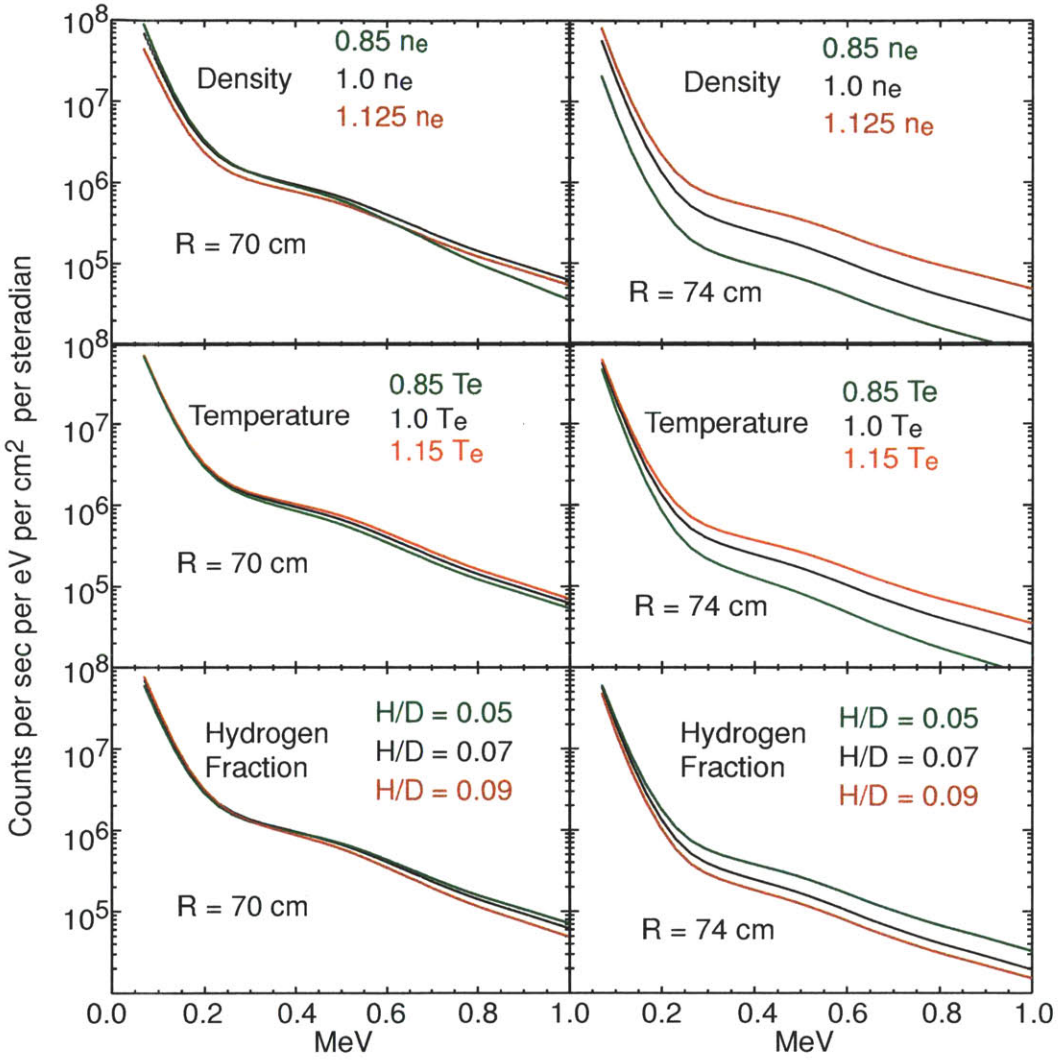

Figure 4-5: Shown are the synthetic diagnostic sensitivity to density (top), electron temperature (middle) and hydrogen fraction (bottom). The sightline near resonance (left) is seen to be very insensitive. However, the sightline away from resonance (right) is very sensitive to electron temperature and density.

from the resonance are considerably more sensitive, especially to electron density and electron temperature, as indicated on the right side of Figure 4-5. However, the uncertainties in plasma parameters only seem to affect the absolute magnitude of the simulated signal and are not seen to affect the dependence of the distribution with respect to energy. These results indicate a simulated sightline near resonance should always agree with experiment in magnitude, and all sightlines should display the correct dependence with respect to energy, even in the presence of significant uncertainties in density and temperature. It should be noted that the results from the CQL3D sensitivity study are in qualitative agreement with the CNPA measured behavior of fast-ion signal seen in Chapter 3, specifically the enhanced effects of density and temperature variation away from the ICRF resonance layer.

It is useful to compare the contributions to the synthetic diagnostic signal to the background D^0 and B^{4+} and that is shown along with the contribution from electron recombination in Figure 4-6. This result is similar to the estimation previously shown in Figure 3-21. The plasma results are linearly sensitive to the boron charge-exchange cross-section and to the estimated B^{4+} density. The results presented in this section will use boron densities that are near the edge estimate of 1% of n_e. We acknowledge the discrepancy between the required boron density for CNPA agreement with simulation and the measured core boron density (see Section 3.3.2), and this discrepancy may warrant future inquiry.

The sensitivity of the simulated results to sightline position is shown in Figure 4-7 which indicates a strong sensitivity to sightline near the ICRF resonance layer. The sightline represented by the blue line in Figure 4-7 is just outboard of the resonance layer and the green line is just inboard. There is a strong difference in the signal between these two synthetic diagnostic sightlines. The estimated error in the position of the sightlines is obtained from the calibration described in Appendix B and is 0.5 cm. Because of the strong sensitivity of the signal to the position of the sightlines, especially near the resonance layer, we must account for the finite width of the CNPA

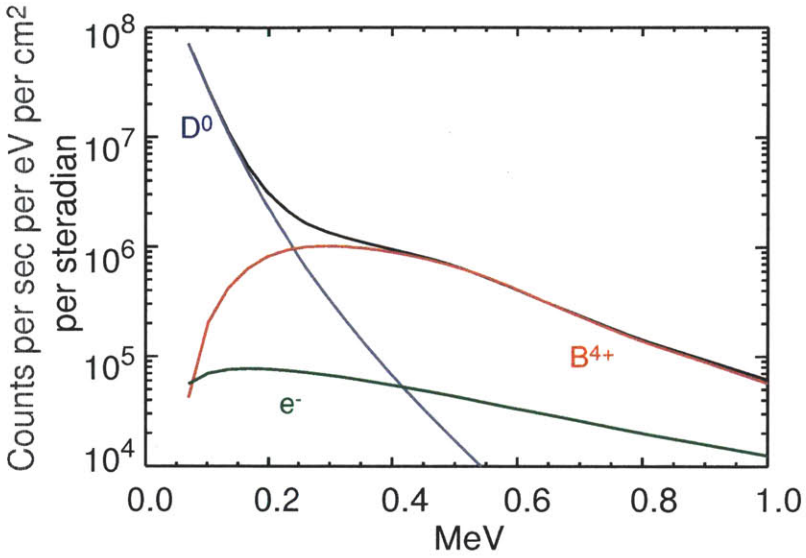

Figure 4-6: The total synthetic diagnostic signal (black) is shown with the individual contributions from CX with B^{4+} (red) and D^0 (blue). Signal from boron tends to dominate above about 300 keV.

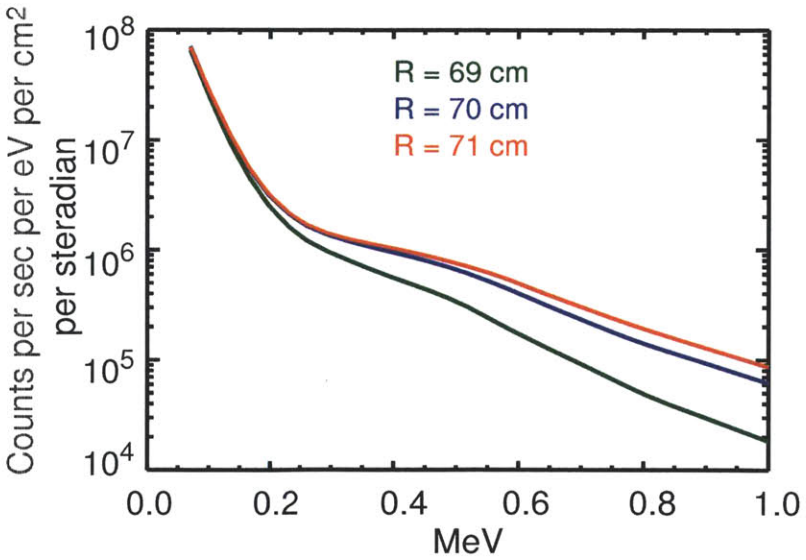

Figure 4-7: Shown is the sensitivity to sightline position. The results highlight the strong sensitivity to the sightline position near the ICRF resonance layer, especially for sightlines that appear on either side of the layer (green vs blue)

viewing line. The synthetic diagnostic assumes a zero-width sightline. To obtain a more realistic finite-width sightline, the synthetic diagnostic signals presented in this thesis are calculated from a weighted average of several zero-width sightlines around the central sightline.

4.5 Steady-state simulations and results

For steady-state simulations, CQL3D begins each iteration with either a Maxwellian distribution or a distribution that is output from a previous iteration. CQL3D then evolves a new minority species distribution function based on the most recently calculated wavefields from AORSA. The CQL3D time is chosen to be large enough that the fast-ion distributions reach steady state. In these simulations the fast-ion distribution is evolved for 440 ms in time steps of 40 ms, and, as shown in Figure 4-8, the synthetic diagnostic signal, and therefore the fast-ion distribution, evolves to a steady state in this time period. Additionally, the CQL3D simulation produces the same result with eighty steps of 1 ms as with two steps of 40 ms. All simulations presented here have orbit-losses turned on although removing orbit losses has a negligible effect on the result (Section 4.5.4).

4.5.1 Simulations of Current Dependence

We discuss results from four plasma discharges with plasma currents constant during a discharge but varying from 0.6 MA to 1.2 MA between discharges. The plasma parameters are shown in Figure 4-9. These plasmas were 5.1 T and only J-Antenna was operated so that the ICRF resonance layer was at a single radial location. Some fast-ion distributions for various flux surfaces are shown for the 600 kA and 1 MA plasmas in Figures 4-10 and 4-11. CNPA results are shown for two sightlines, one near the resonance and one 4 cm outboard of the resonance. (Sightlines farther out do not have sufficient signal for comparison in these discharges). The placement of

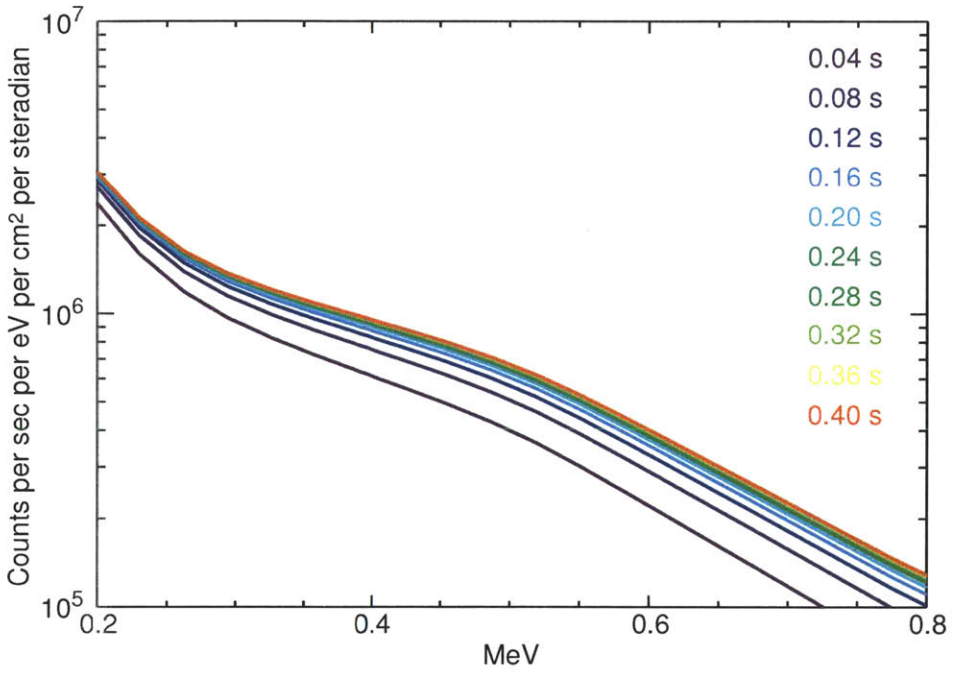

Figure 4-8: CQL3D evolution of a minority ion distribution for a constant quasi-linear diffusion coefficient as calculated by AORSA.

the resonant layer and the CNPA sightlines have been shown previously in Figure 2-14.

Comparisons between CNPA data and AORSA-CQL3D simulations for the four plasma discharges shown in Figure 4-9 are provided in Figures 4-12 to 4-15. For these simulations the boron concentration was chosen to be 2.5% of n_e, which is at the upper range of reasonable values for boron concentration. A boron density that is 2.5% of n_e was found to provide the best agreement across all discharges and sightlines. In this manner, it can be viewed as a CNPA/simulation prediction of the boron density. Changing n_B will linearly shift the simulated neutral flux in the region where charge-exchange with boron is still the dominant neutralization method. Lowering the boron density will make charge-exchange with deuterium the dominant neutralization method for a larger region of the low energies (see Figure 4-6).

The simulation results have the best agreement with experiment for the 0.8 and 1.0 MA plasmas (Figures 4-13 and 4-14). There is some disagreement between the simulation and the experiment for the 0.6 MA (Figure 4-12) and 1.2 MA (Figure 4-15) plasmas. At 0.6 MA, the simulation underestimates the low energy (~300 keV) count rate on both sightlines. At 1.2 MA the simulation overestimates the low energy (~300 keV) signal on the sightline farther from the resonance (R = 74 cm). However, the simulation is accurate for the near-resonance sightline. For all currents the simulation agrees with experiment for higher energy (> 500 keV) count rates, and, most importantly, the simulation reproduces the dependence of the CNPA count rate on fast-ion energy. The energy dependence is important because the major source of uncertainties, boron concentration and boron charge-exchange cross-section are unlikely to affect the shape of the curve above ~350 keV, just the absolute magnitude.

As plasma current is increased, the magnitude of the count rates on the sightline farther from the resonance (R = 74 cm) gets gradually closer to the on-resonance (R = 70 cm) count rate. This is indicative of better fast-ion confinement at higher currents. It was uncertain whether this feature would be reproduced in the simulation

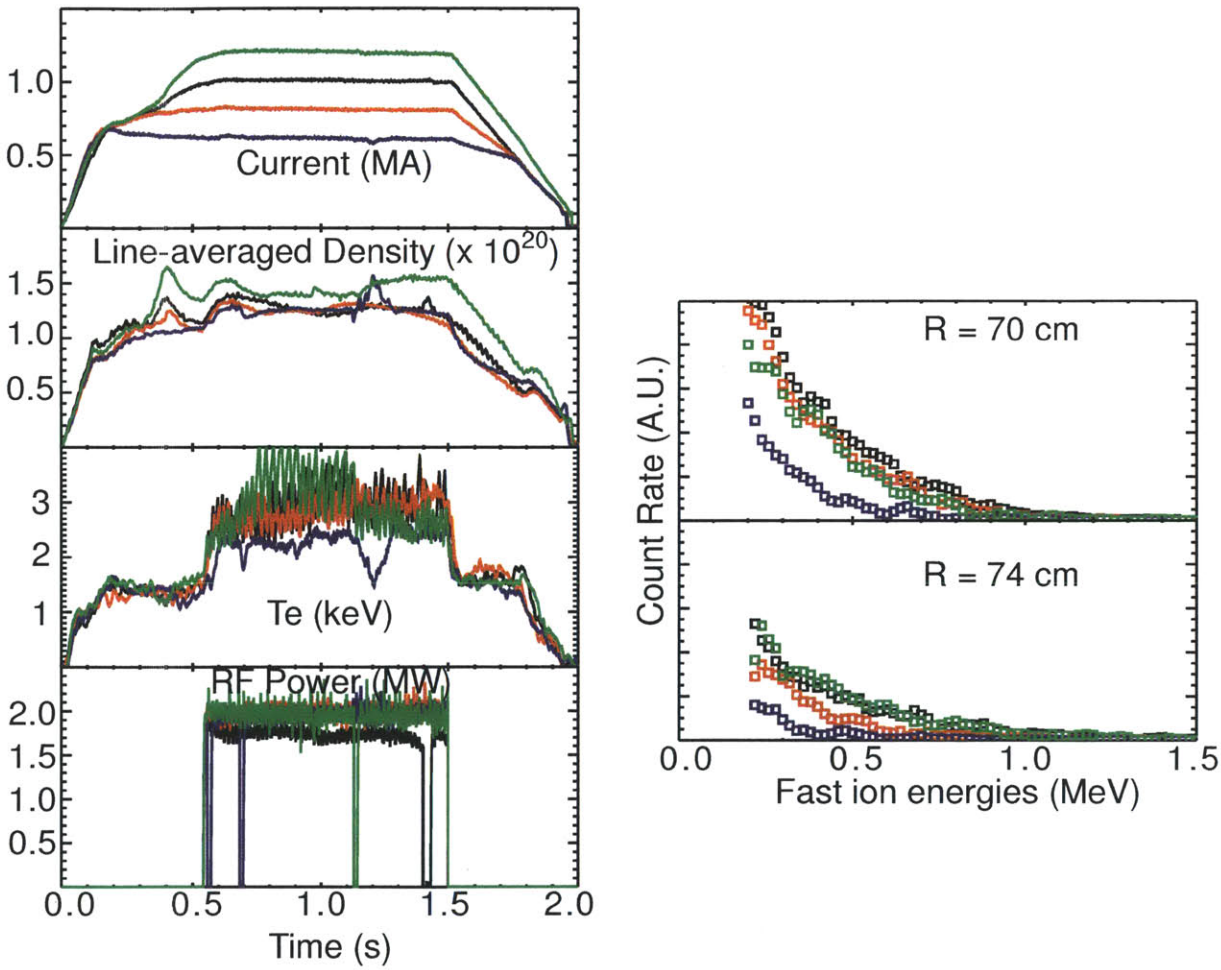

Figure 4-9: Overview of plasma parameters for four plasma shots at different plasma currents: 1.2 MA (green) 1.0 MA (black) 0.8 MA (red) and 0.6 MA (blue)

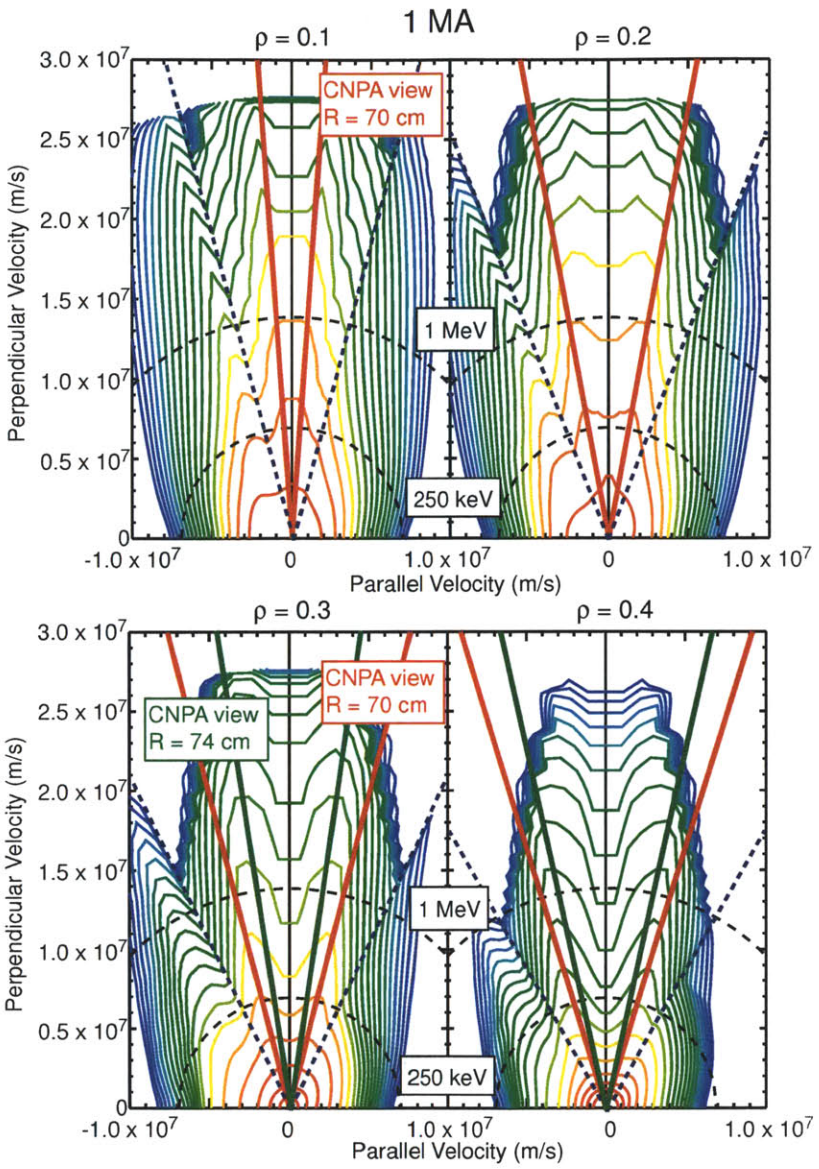

Figure 4-10: Fast-ion midplane distribution functions for a 1MA plasma at 4 flux surfaces ranging from $\rho = 0.1$ to $\rho = 0.4$. On each distribution, two curves of constant energy are shown to indicate CNPA range. Also shown is the trapped-passing boundary (dashed blue) the CNPA sightline at $R = 70$ cm (solid red) and the CNPA sightline at $R = 74$ cm (solid green).

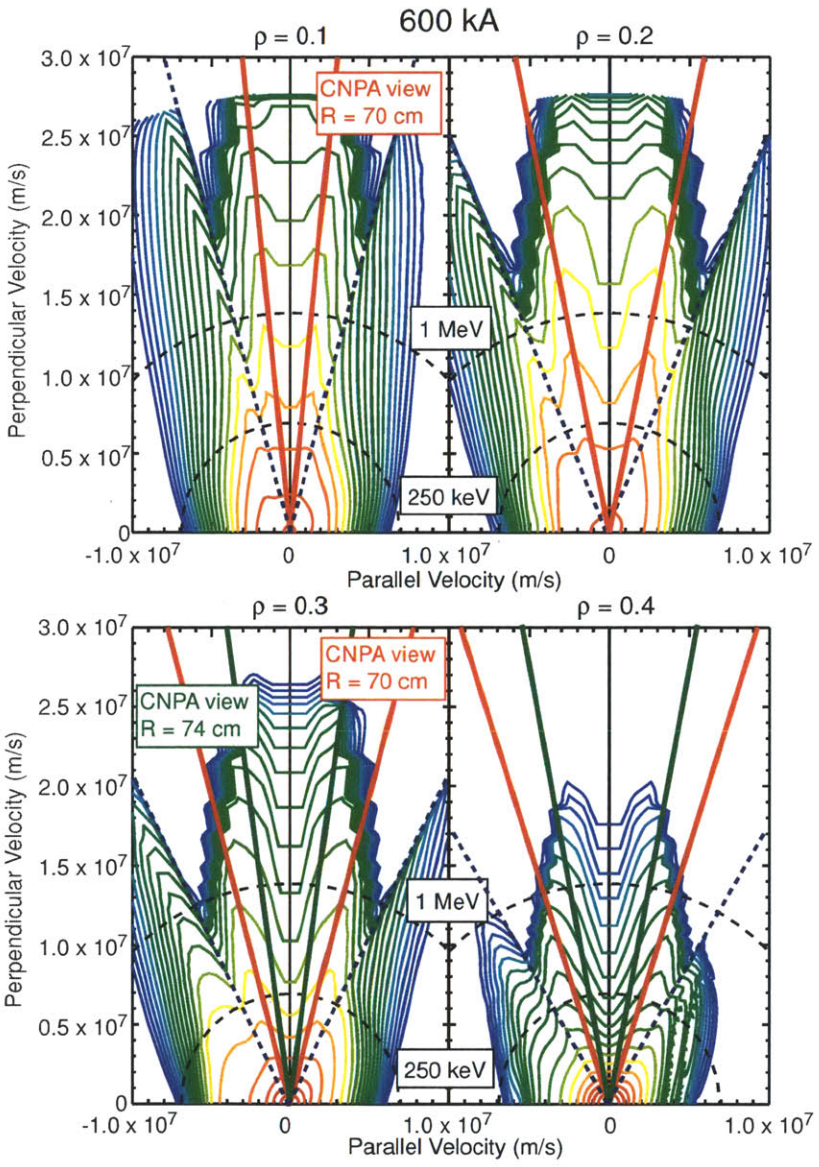

Figure 4-11: Fast-ion midplane distribution functions for a 600 kA plasma at 4 flux surfaces ranging from $\rho = 0.1$ to $\rho = 0.4$. On each distribution two curves of constant energy are shown to indicate CNPA range. Also shown is the trapped-passing boundary (dashed blue) the CNPA sightline at $R = 70$ cm (solid red) and the CNPA sightline at $R = 74$ cm (solid green).

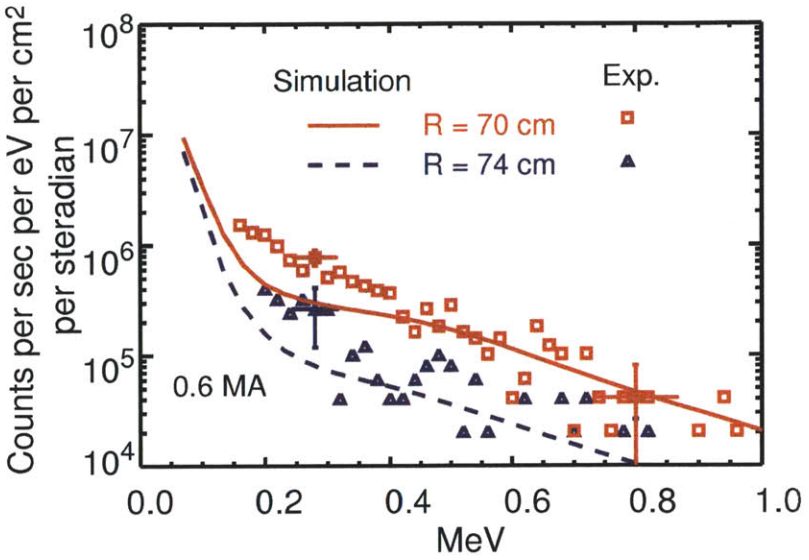

Figure 4-12: The CNPA experimental results (symbols) are compared with AORSA-CQL3D simulations (lines) at plasma current of 0.6 MA. Two sightlines at R = 70 cm (red) and R = 74 cm (blue) are shown.

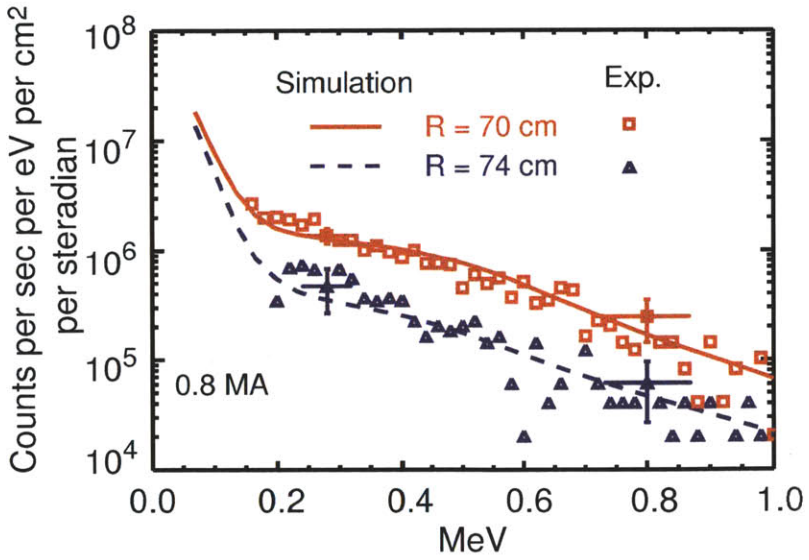

Figure 4-13: The CNPA experimental results (symbols) are compared with AORSA-CQL3D simulations (lines) at plasma current of 0.8 MA. Two sightlines at R = 70 cm (red) and R = 74 cm (blue) are shown.

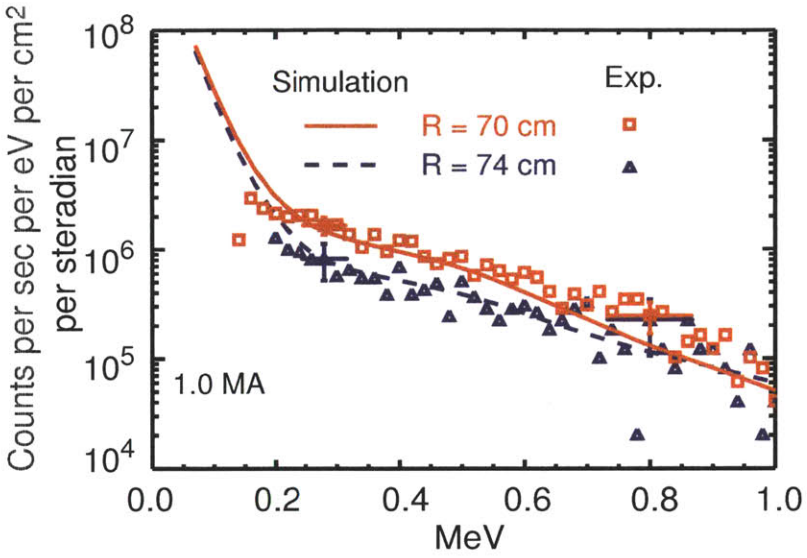

Figure 4-14: The CNPA experimental results (symbols) are compared with AORSA-CQL3D simulations (lines) at plasma current of 1.0 MA. Two sightlines at R = 70 cm (red) and R = 74 cm (blue) are shown.

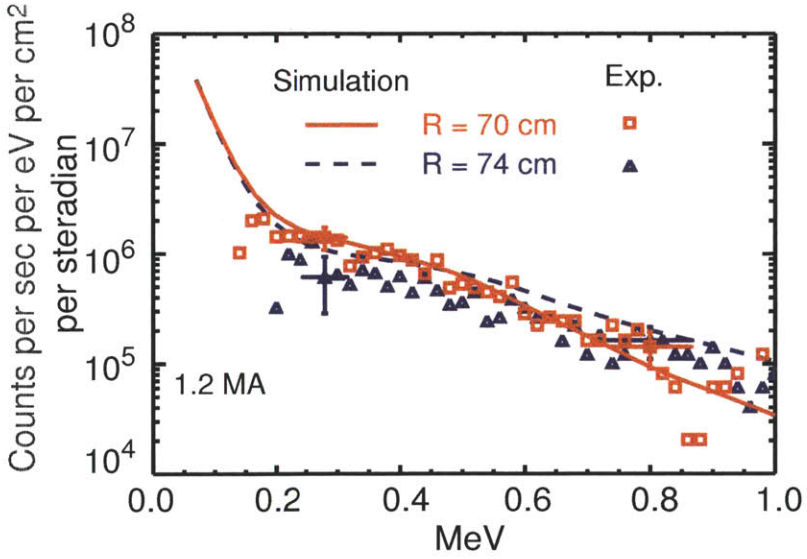

Figure 4-15: The CNPA experimental results (symbols) are compared with AORSA-CQL3D simulations (lines) at plasma current of 1.2 MA. Two sightlines at R = 70 cm (red) and R = 74 cm (blue) are shown.

because of the zero banana-width limitation. The results show that this feature is indeed reproduced by the simulation, indicating that the zero banana-width assumption may be acceptable for simulating a steady-state distribution. Examining the distribution functions, it is clear that there are more energetic distributions at flux surfaces between $\rho = 0.3$ and $\rho = 0.4$. The sightline at $R = 74$ cm does not intersect flux surfaces inside $\rho \approx 0.25$.

Overall the simulation provides agreement with the experimental results within a factor of 2 for the wide range of currents chosen. The simulation is able to correctly estimate the CNPA signal both as a function of fast-ion energy, and as a function of sightline position thus providing some confidence in the capability of the simulation model to correctly predict the fast-ion distribution function for minority ICRF heating.

4.5.2 Role of Plasma Profiles in Current Dependence

As seen in Figure 4-9 there are some unavoidable changes in plasma profiles, specifically in Electron temperature, which changes by a factor of $\sim$1.5 between the 600 kA discharge and the 1 MA discharge. As seen in Eq. 1.9, the ion-electron slowing down time is $\propto T_e^{3/2}$. Therefore, it is conceivable that the electron temperature plays a significant role in the fast-ion distribution. In order to test this effect, a simulation was done using the plasma profiles from the 1 MA discharge and the magnetic equilibrium from the 600 kA discharge. A resulting fast-ion distribution is shown in Figure 4-16 alongside the 600 kA and 1 MA simulations. The distribution is clearly more similar to the 600 kA discharge than the 1 MA discharge, implying that the magnetic equilibrium is playing a larger role in shaping the fast-ion distribution than the plasma profiles.

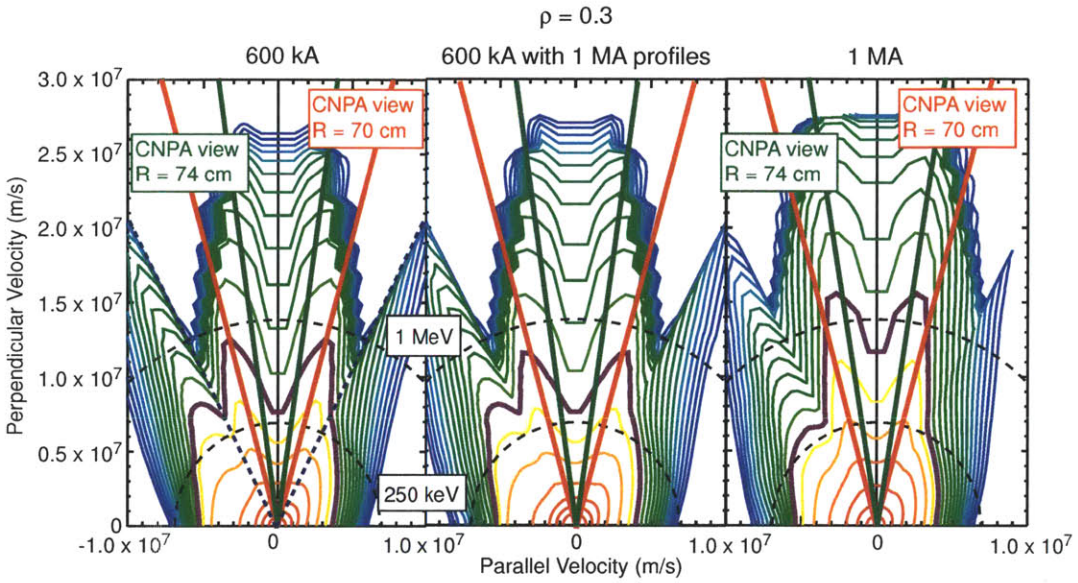

Figure 4-16: Shown are three fast-ion distributions at $\rho = 0.3$ for a 600 kA discharge (left), a 600 kA discharge with plasma profiles from the 1 MA simulation (middle), and a 1 MA discharge. A contour of equivalent phase-space density near the center of the CNPA detection range, is highlighted in magenta on all three plots for comparison.

4.5.3 Simulations of RF Power Dependence

To simulate the dependence of the fast-ion distribution on RF power, we use the 1 MA simulation above and vary the RF power level input into AORSA. We do not have a convenient set of discharges to simulate against, so instead we will look at the qualitative features of the fast-ion distribution in both the simulations. The results of the RF scan are given in Figures 4-17 and 4-18. In Figure 4-17 we show the CQL3D calculation of the effective temperature of the fast-ion distribution plotted against plasma radius for various power levels. The curve representing the 1.0 MA simulation plotted earlier is shown in the thick green curve. The peak effective temperature in CQL3D seems to stagnate around 200-300 keV in the simulations. Additional power tends to create more energetic distributions further out in plasma radius, but does not significantly increase the peak effective temperature. Figure 4-18 shows the simulated CNPA signal from the synthetic diagnostic, both near and away from the resonance layer. Here we see that there is very little noticeable change in the effective temperature seen by the CNPA and only a slight difference in the total count level for power levels above 2 MW. These results are in qualitative agreement with the results found from the amalgamated CNPA signal (see Figures 3-7 and 3-28). In both the simulation and the experiment, additional power does not seem to raise the fast ion tail temperature as seen by the CNPA, although it does increase the overall count rate. It should be noted that these simulations include RF power levels of 0.1 MW and 6.0 MW, neither of which is obtainable in experiment.

4.5.4 Estimates of Orbit Losses

In order to shed light on the role that orbit losses play in the fast-ion distributions in these discharges, we use the simulations to calculate the number of ions that are in lost orbits, and the energy that they carry. CQL3D includes the option to turn on a simple banana loss term. When banana losses are enabled, all particles that satisfy $r + \Delta_b/2 > a$ are removed and replaced with a thermal particle on the same

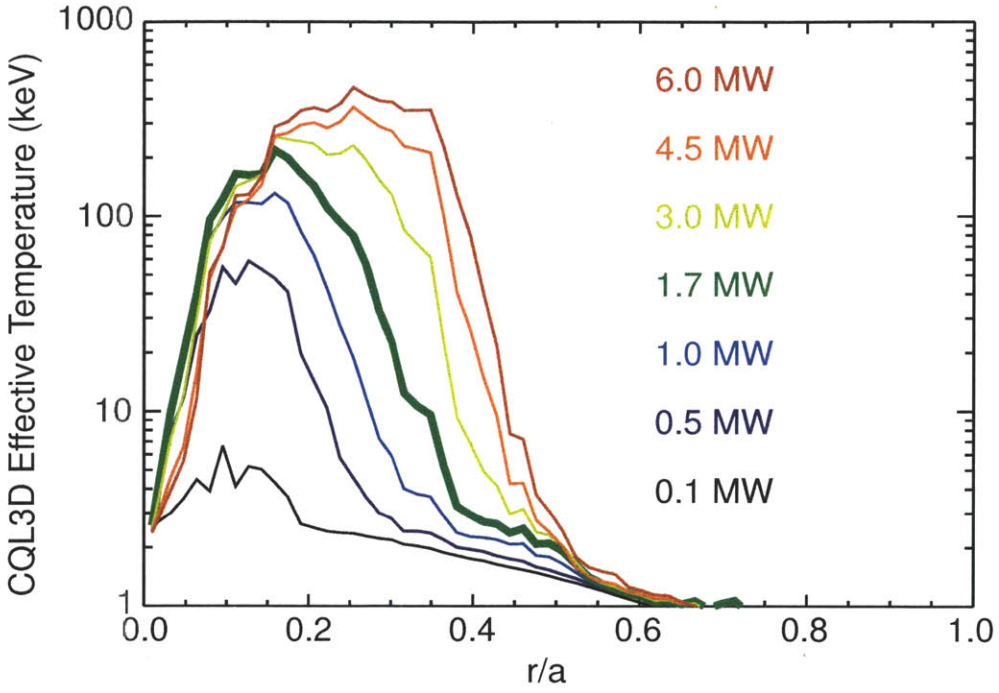

Figure 4-17: Shown are simulated effective temperatures for various RF power levels. The thick green curve represents the 1.0 MA discharge shown in Figure 4-14

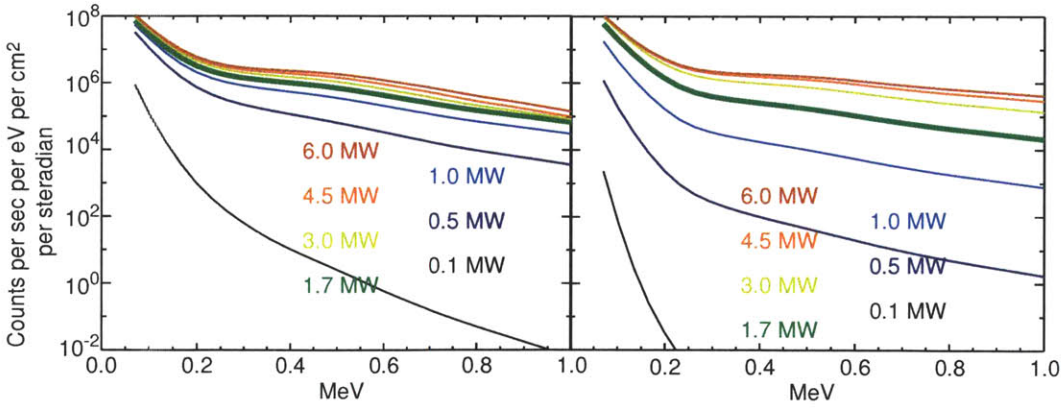

Figure 4-18: Shown are simulated CNPA signals for various RF power levels for the CNPA channel near resonance (left) and away from resonance (right). The thick green curve represents the 1.0 MA discharge shown in Figure 4-14

flux surface. Here, r represents the radial position of the particle guiding center on the outboard midplane, Δ_b is the banana width, and a is the radius of the last closed flux surface on the outboard midplane.

In order to estimate particle losses we simulate the same discharge while toggling the loss term. In Figure 4-21, we show the results from a comparison of the 'loss' and 'no-loss' case for the 0.6 and 1.0 MA plasma discharges analyzed in the previous section. The distribution function for the 'loss' and no-loss' cases are plotted for two flux surfaces in Figures 4-19 and 4-20. Here we see very little effect from the losses in the core of the 1 MA case, but significant losses in the 600 kA case, even deep into the core. As expected most of the losses occur near the trapped-passing boundary. However, it should be noted that there is very little change to the distribution functions on the sightlines viewable by the CNPA at either plasma current.

The top plots in Figure 4-21 shows the number of particles on each flux surface that have been moved into different energy bins due to particle losses. The total is represented as a fraction of the number of particles lost on each flux surface. The middle plots show the total amount of energy that is lost from flux surfaces when losses are turned on (black) and also the amount that is gained (red). Again the result is given as a fraction of the total energy on each flux surface.

The gained energy is likely an artifact of the simulation. The power input to the simulation is the power absorbed by the plasma. In a tokamak, particles on unconfined orbits will deposit their power on the wall. In simulations, the power that would be lost due to unconfined particles is instead shifted onto particles in confined orbits. Nevertheless, the analysis does provide an estimate of the total energy lost. The simulation result shows that at 0.6 MA, at most, 5% of energy is lost from any flux surface. However, the flux surfaces of peak absorption have negligible losses.

The bottom plots in Figure 4-21 show the simulated effective temperature as a function of radius. A very small difference is noticeable on the 0.6 MA simulation, but no change is visible at all on the 1.0 MA case and the two curves completely

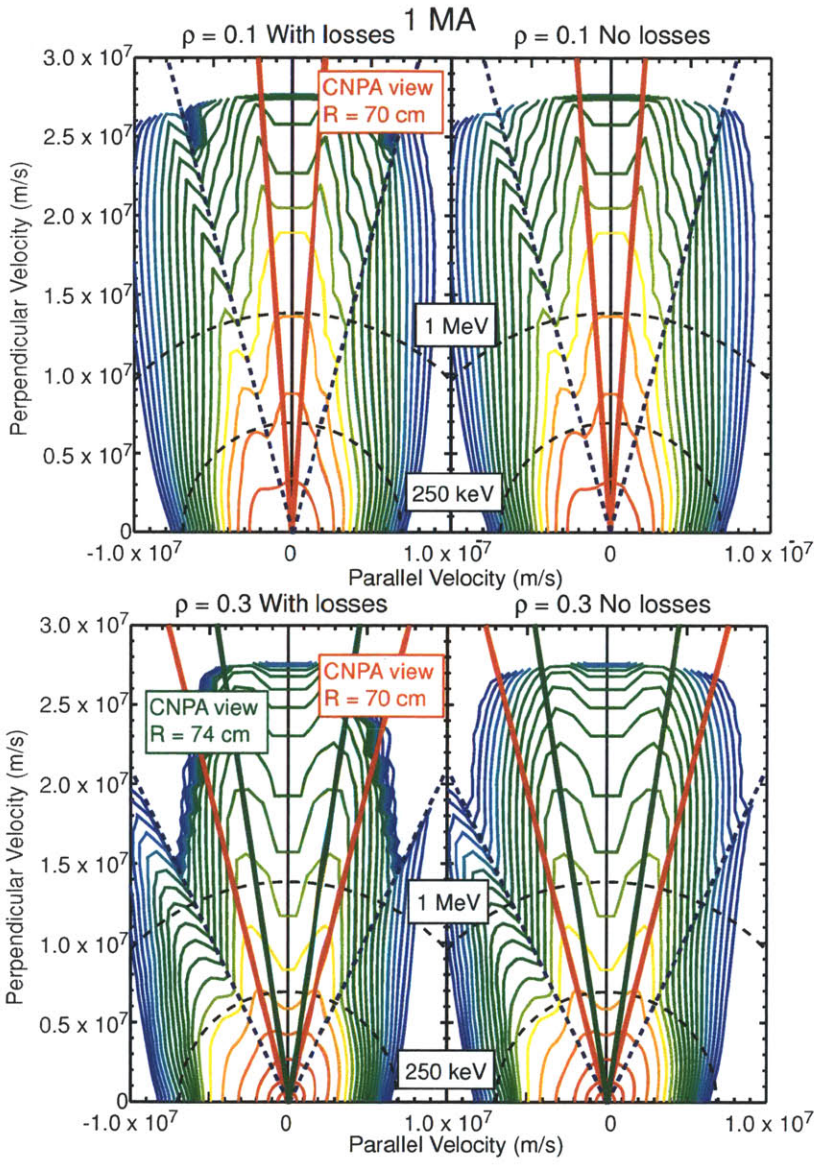

Figure 4-19: Comparisons of distributions with and without orbit losses for a 1 MA plasma for flux surfaces at $\rho = 0.1$ and $\rho = 0.3$. On each distribution, two curves of constant energy are shown to indicate CNPA range. Also shown is the trapped-passing boundary (dashed blue) the CNPA sightline at $R = 70$ cm (solid red) and the CNPA sightline at $R = 74$ cm (solid green).

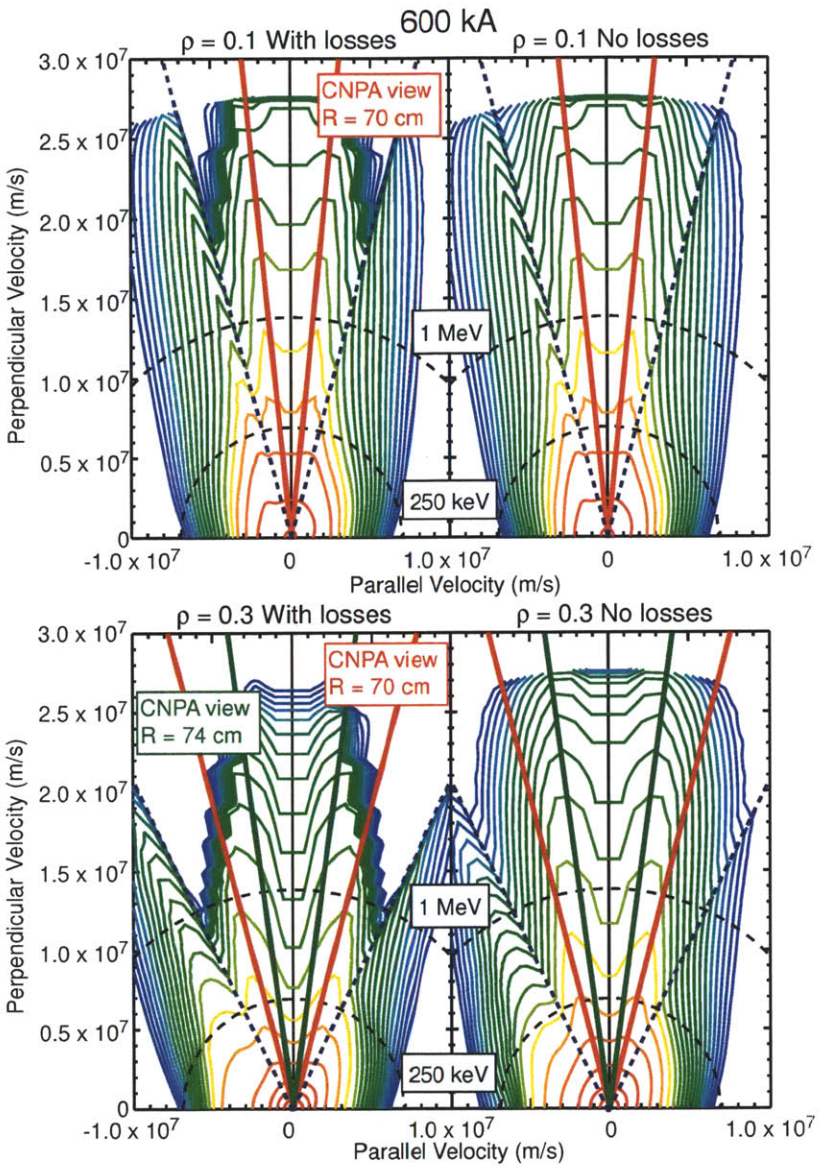

Figure 4-20: Comparisons of distributions with and without orbit losses for a 600 kA plasma for flux surfaces at $\rho = 0.1$ and $\rho = 0.3$. On eadch distribution, two curves of constant energy are shown to indicate CNPA range. Also shown is the trapped-passing boundary (dashed blue) the CNPA sightline at $R = 70$ cm (solid red) and the CNPA sightline at $R = 74$ cm (solid green).

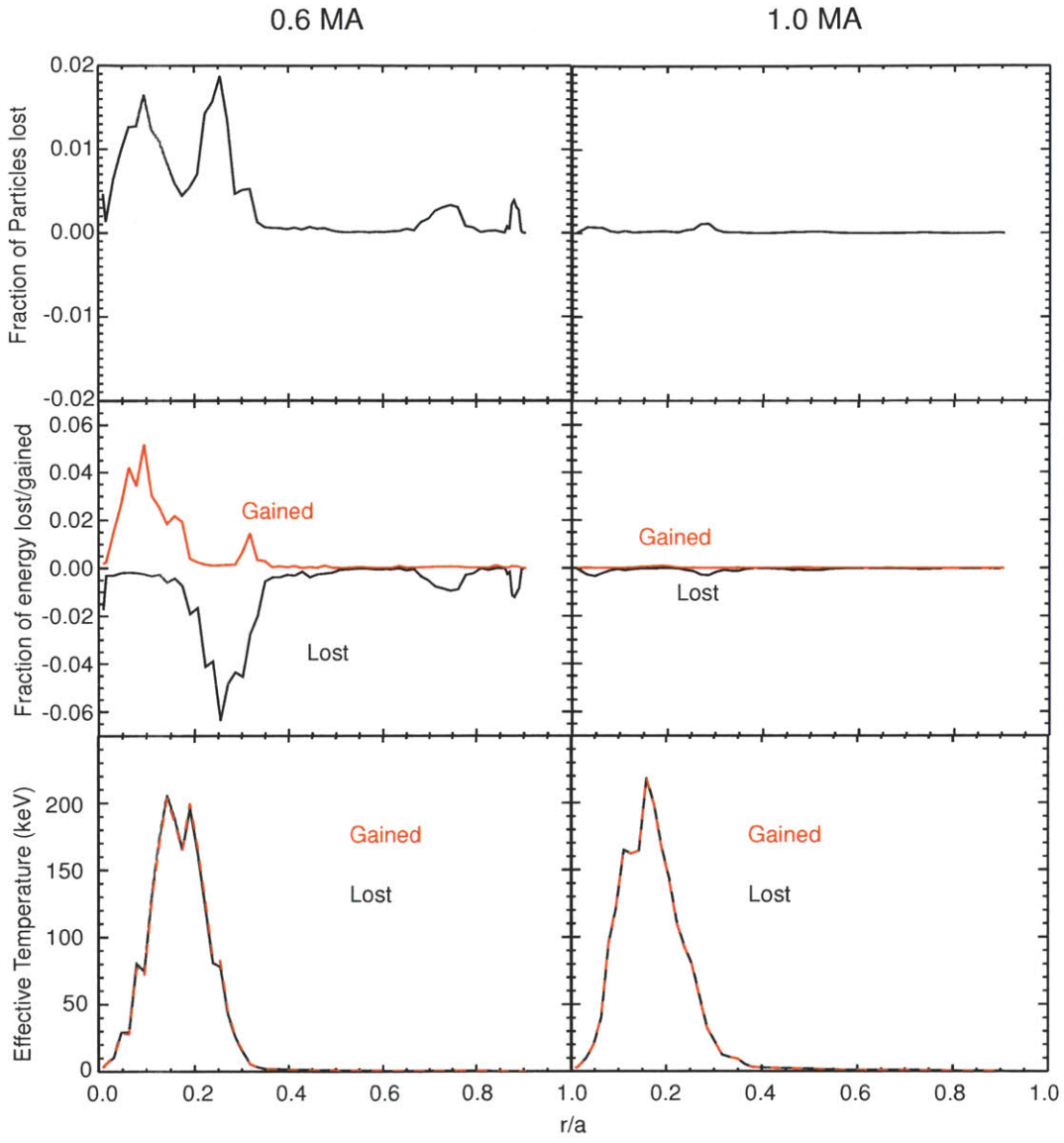

Figure 4-21: Shown are CQL3D results for particle losses (top), energy losses (middle) and effective temperature (bottom). Results are given for a discharge at 0.6 MA (left) and 1.0 MA (right)

overlap. The results are that orbit losses cannot explain the scalings of the fast-ion distributions with respect to plasma current or RF power.

Chapter 5

Time-Dependent Results

In this chapter we turn our attention to fast-ion distributions that are evolving in time, $df/dt \neq 0$. Specifically we examine fast ion distributions in two distinct periods of time immediately after changes in ICRF power. The first is the period of time immediately after ICRF turns on, when the minority ion distribution evolves from a thermal Maxwellian towards the steady-state distributions studied in previous chapters. The second period is after the ICRF turns off, where the energetic tail decays away and the minority ion distribution relaxes to a Maxwellian. In this chapter we discuss results from an experiment designed to provide repeated measurements of the evolving fast-ion distribution through modulated ICRF heating. Then we discuss simulations that attempt to reproduce the distribution. Through a comparison of the simulation and experimental results, we find a significant discrepancy and the possible reasons for this discrepancy are examined.

5.1 Experimental setup

This chapter focuses in detail on a single representative discharge with modulated ICRF heating. Similar plasma discharges with modulated ICRF were seen in Chapter 3 in the discussion of fast-ion dependences on various plasma parameters. The plasma

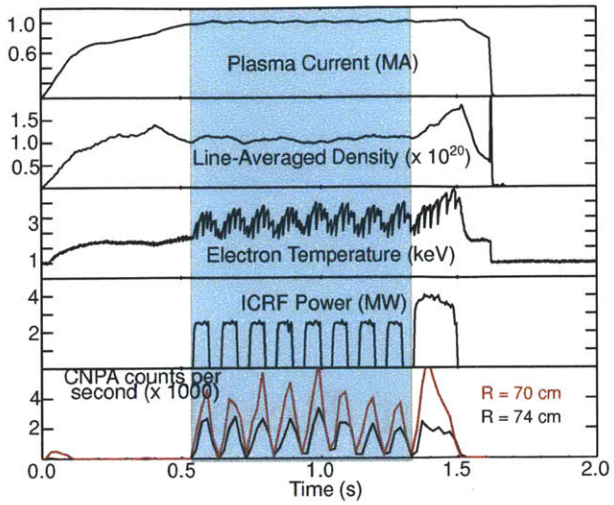

Figure 5-1: Plasma parameters for a discharge with modulated ICRF used for analysis of time-dependent fast-ion distribution.

parameters for the representative discharge are shown in Figure 5-1. As shown in the highlighted region, there are eight full cycles of ICRF. Because there are not enough fast-ion counts during a single ICRF modulated period to perform a proper analysis, to improve statistics we divide each modulated period into 10 ms bins, and sum over the eight on-off cycles. Each period has a 60% duty cycle with on time of 60 ms and an off time of 40 ms. A cartoon of the binning procedure is shown in Figure 5-2. The color of each bin in this figure corresponds to the appropriate time bin color in subsequent plots. Again, because of low count rates, we also lose significant resolution in energy. Therefore, we split the fast-ions into four energy bins of 240 keV width (except for the first bin which goes from 150-240 keV). The time evolution of the fast-ion signal from one CNPA sightline near the resonance is shown in Figures 5-3 (rise) and 5-4 (decay). It is also useful to display how each energy bin evolves in time, and this is shown in Figure 5-5

From Figures 5-3 and 5-4 we see that the fast-ion distribution appears to reach steady state after ~30 ms. The relaxation to a Maxwellian after the ICRF turns off

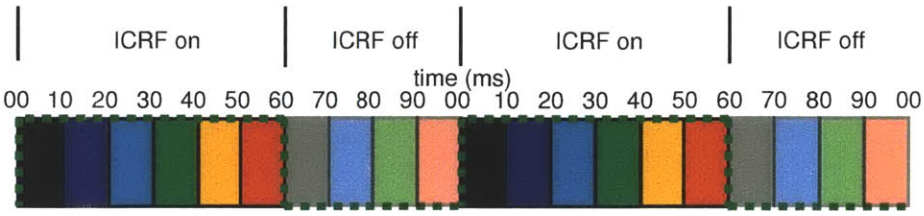

Figure 5-2: Cartoon of binning procedure for time-dependent CNPA measurements. The dashed green line represents the ICRF modulated power.

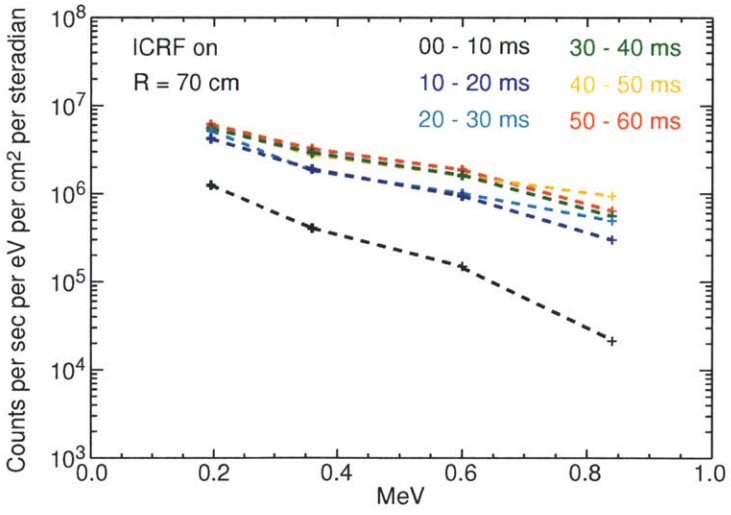

Figure 5-3: Energy profiles of the measured fast-ions showing the rise to steady state after the ICRF is turned on.

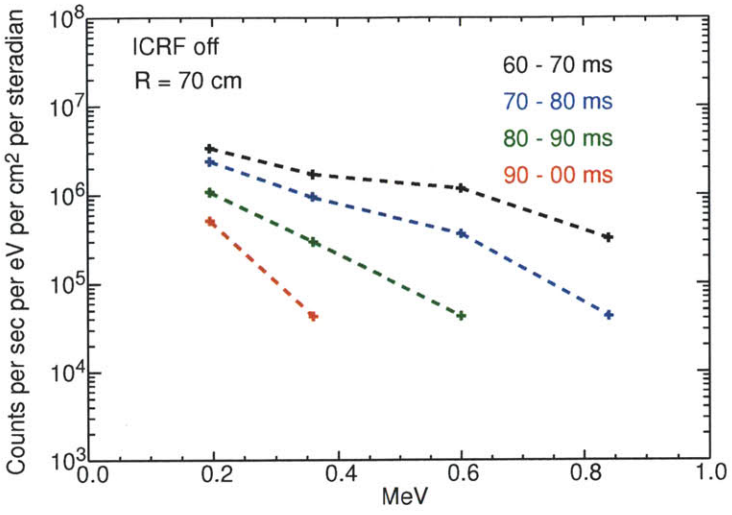

Figure 5-4: Energy profiles of the measured fast-ions showing the relaxation to steady state after the ICRF is turned off.

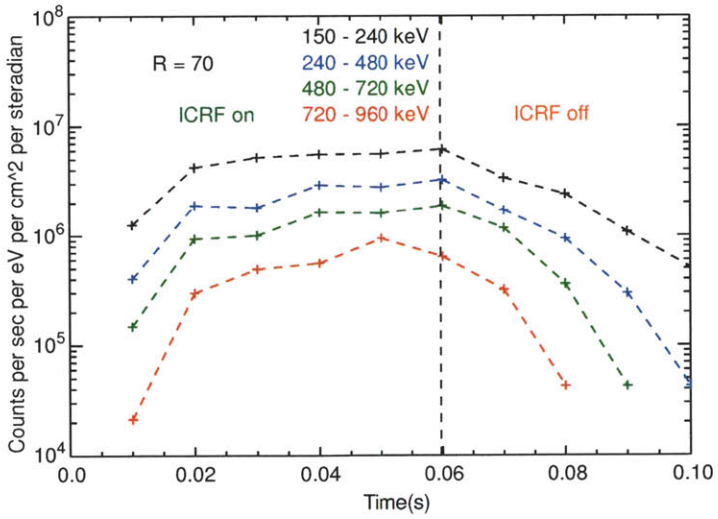

Figure 5-5: Measured fast-ions are plotted vs. time for a full on off cycle for the four energy bins.

occurs on a similar timescale. In both cases, the characteristic time-constants for the rise and relaxation are ~10 ms. In contrast, we have already seen that the time for CQL3D to reach steady state was much slower (Figure 4-8).

5.2 Simulation setup

In order to simulate the time-dependent distribution we need to couple the AORSA and CQL3D simulations in a manner that evolves the distribution function self-consistently in time and accounts for the changing plasma parameters during the simulation. This process is accomplished by making individual input files for each 1 ms iteration. We use CQL3D to evolve a distribution 1 ms at a time, using internal time steps of 0.1 ms. (For comparison, in the steady state-simulations in Chapter 4, we evolved a single 440 ms simulation with internal time steps of 40 ms.) After each ms, we call AORSA and get updated quasi-linear coefficients. After 60 ms, the ICRF turns off and AORSA is no longer needed. Between 60 ms and 100 ms, only CQL3D is called.

The iteration sequence is managed by a Python script. The Python script selects the appropriate input file for the time-step. The script also has the capability of altering different simulation parameters during the run (e.g. ICRF power, radial transport parameters etc.), however using it in this manner to alter plasma profiles is cumbersome.

5.3 Results

A direct comparison between the predicted signal from the synthetic diagnostic and the CNPA measurements is shown in Figures 5-6 to 5-9. Results are shown both near and away from the resonance. It is evident that there are large discrepancies between the experimental and the simulated results. The high energy ions evolve

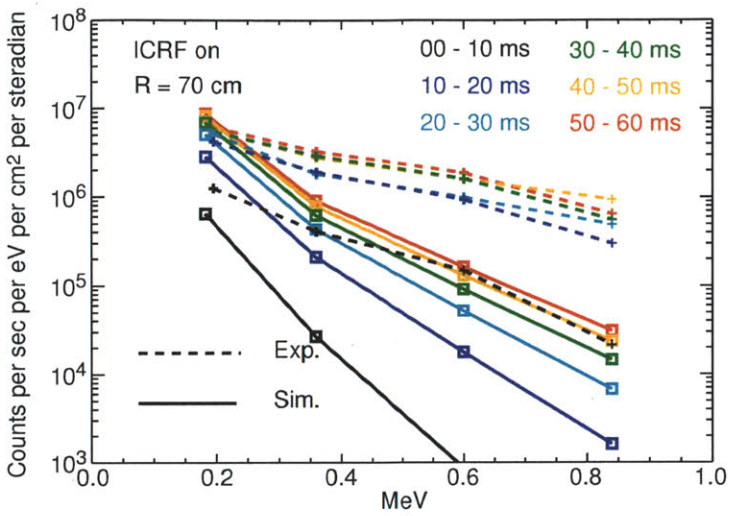

Figure 5-6: Energy spectra of the measured and simulated fast-ions near resonance. The experimental measurement show that the fast-ions rise to steady state after the ICRF is turned on in ~30 ms. The simulated fast-ions do not reach steady state after 60 ms.

much quicker in the experiment than in the simulation. This is clear from comparing the solid black and blue curves to the dashed black and blue curves in Figures 5-6 and 5-7 or the solid blue and red curves to the dashed blue and red curves in Figures 5-11 and 5-10. In the experiment the two highest energy bins reach over half of their final value after 20 ms, while the simulation is under 10% of its final value. It is also useful to compare the shape of the rise and decay of the signal. This can be seen most easily by scaling the simulation signal to the experimental results by a constant multiplicative factor. The scaled results for the summation of all ions between 300 and 800 keV are shown for both sightlines in Figures 5-12 and 5-13. In both cases we can see that the simulation has a much slower time constant than the experiment. In fact, on the channel away from the resonance (Fig. 5-13) the simulated rise looks almost linear.

In Figures 5-12 and 5-13, the simulated results (solid lines) are plotted with time resolution of 1 ms, corresponding to the time in between calls to AORSA. With this

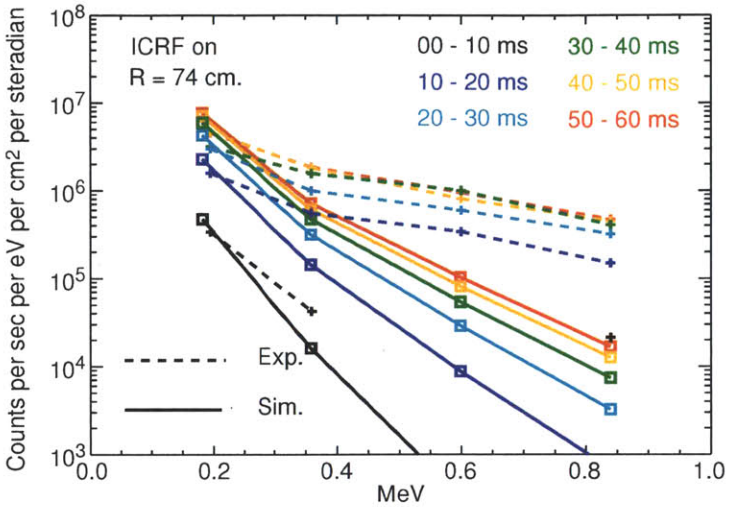

Figure 5-7: Energy profiles of the measured and simulated fast-ions away from resonance showing the rise to steady state after the ICRF is turned on.

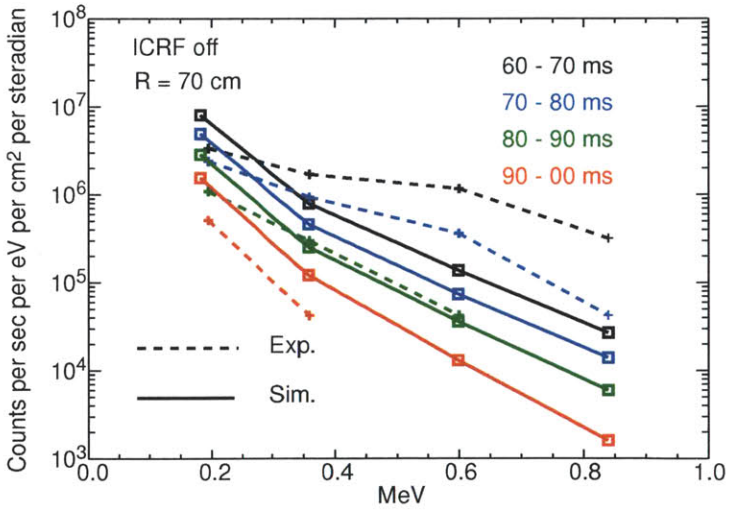

Figure 5-8: Energy profiles of the measured and simulated fast-ions near resonance showing the relaxation to Maxwellian after the ICRF is turned off.

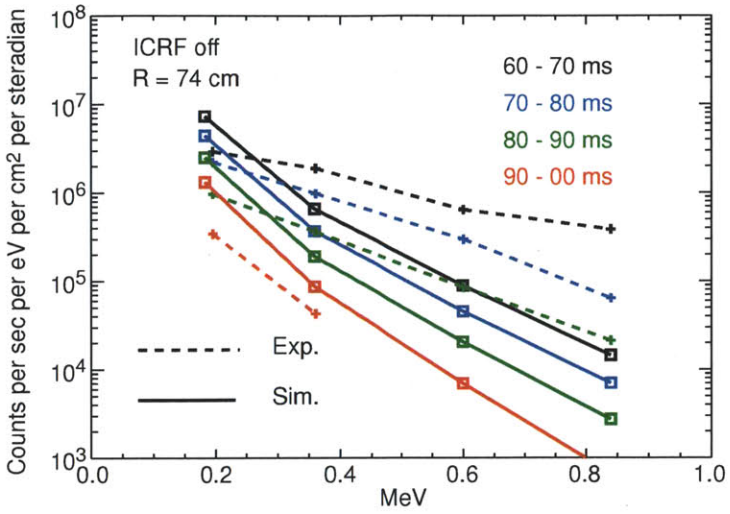

Figure 5-9: Energy profiles of the measured and simulated fast-ions away from resonance showing the relaxation to Maxwellian after the ICRF is turned off.

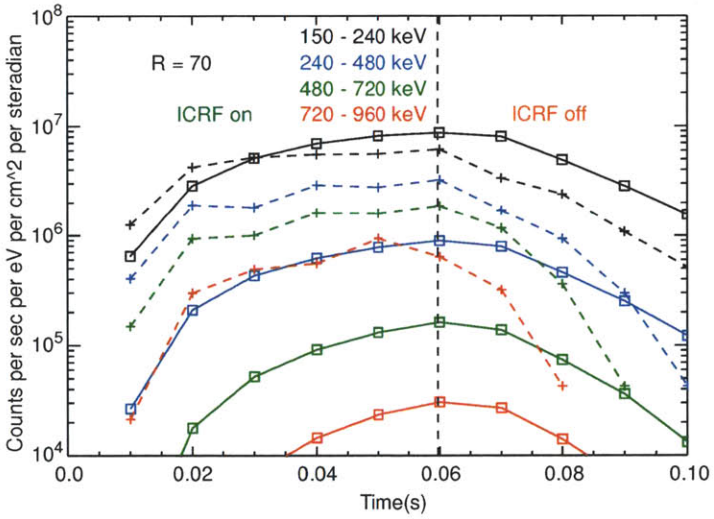

Figure 5-10: Simulated (solid) and measured (dashed) fast-ion signals over a full on-off cycle for a sightline near the ICRF resonance layer.

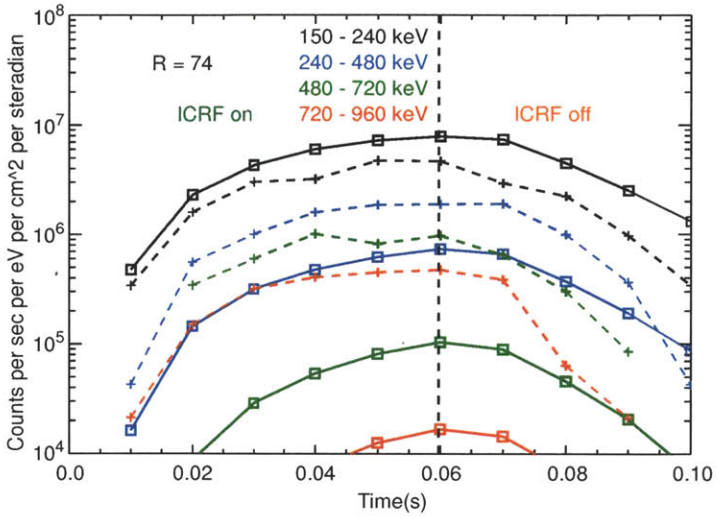

Figure 5-11: Simulated (solid) and measured (dashed) fast-ion signals over a full on-off cycle for a sightline away from the ICRF resonance layer.

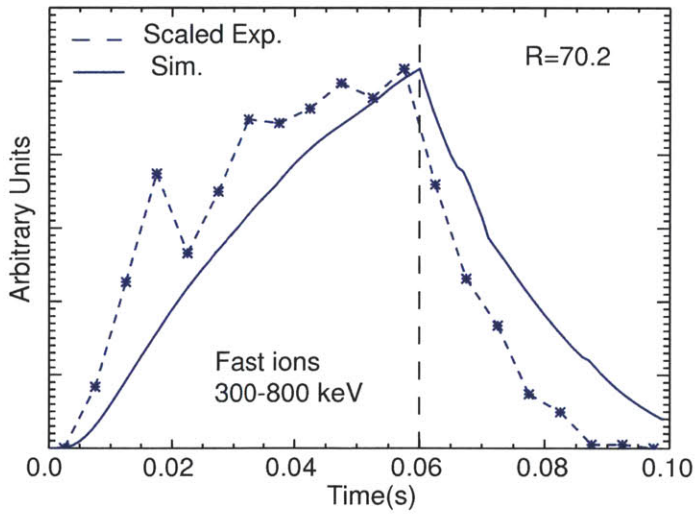

Figure 5-12: The measured CNPA distributions (dashed lines) are normalized and plotted against the simulated signal (solid blue) as a function of time for the channel near the resonance.

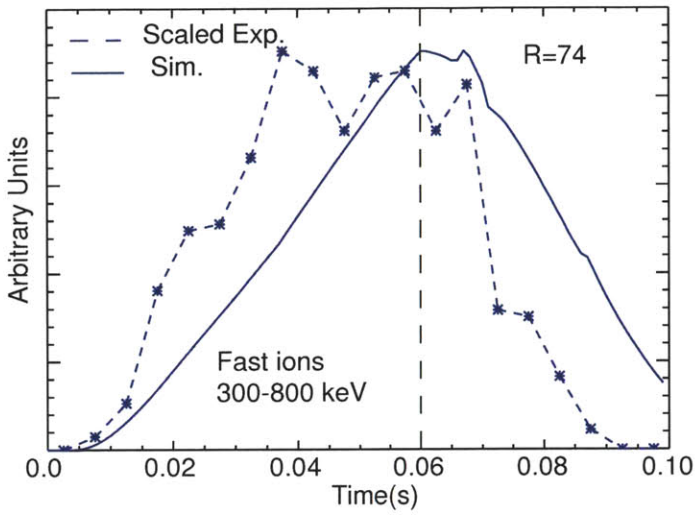

Figure 5-13: The measured CNPA distributions (dashed lines) are normalized and plotted against the simulated signal (solid blue) as a function of time for the channel away from the resonance.

resolution, an interesting feature is apparent. For the channel near the resonance (Figure 5-12) we see that the simulated signal begins decaying immediately after the ICRF is turned off. However, on the channel farther away (Figure 5-13)the fast-ion signal persists for about 10 ms after the ICRF turns off. Unfortunately, the experimental measurement does not have sufficient time resolution to determine whether there is a persistent signal on the off-resonance channel after the ICRF turns off.

As is evident from Figures 5-6 and 5-7, the simulated distributions do not evolve to the same distribution as is measured by the CNPA. It is clear from Figure 4-8 that a simulation with fully evolved wave-fields does not reach steady state after 60 ms. However it is also possible that the fast-ion distribution is also not yet in steady state either. To address this question, we compare the CNPA distribution during the last 30 ms of the ICRF on time with a steady state simulation. These results are shown in Figure 5-14. By extrapolating to steady state, we find that the simulation underpredicts the magnitude of the signal for both channels. This disagreement is partly caused by the difficulty of obtaining the proper steady-state density and temperature. However, the shape of the synthetic diagnostic signal with respect to energy is greatly improved for both sightlines.

We can also examine the relaxation of the extrapolated steady-state distribution. This is shown for the on and off resonance sightlines in Figures 5-15 and 5-16 respectively. Here, the relaxation from the steady-state distribution is plotted in red, normalized, and overlaid on the fully time-dependent results. We see no improvement of the agreement during relaxation when the distribution begins in steady-state. This is indicative of a further discrepancy between CQL3D and the experimental data.

5.3.1 Discussion of Discrepancies

This section examines several possible reasons for the discrepancies between the AORSA-CQL3D simulation and the CNPA experimental data for time-dependent,

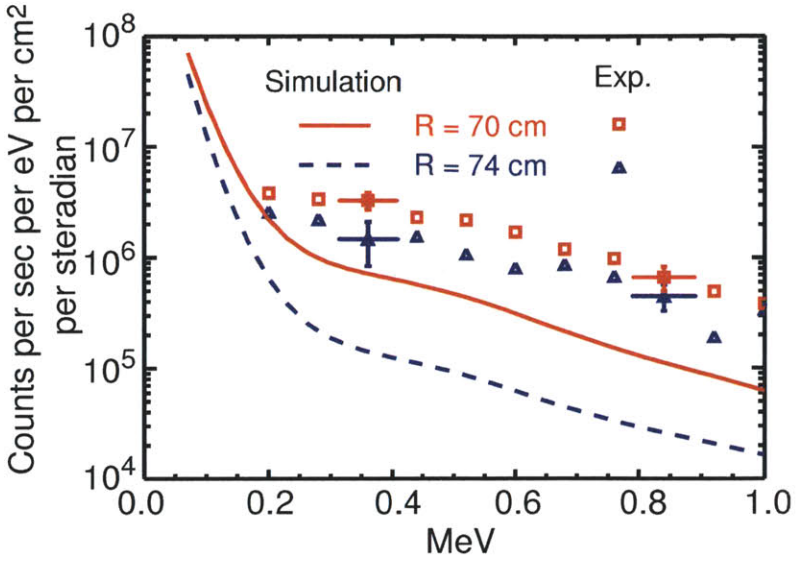

Figure 5-14: The AORSA-CQL3D time-dependent simulation is extrapolated to steady state and the results are compared to the CNPA signal summed over the latter halves of the ICRF on-times.

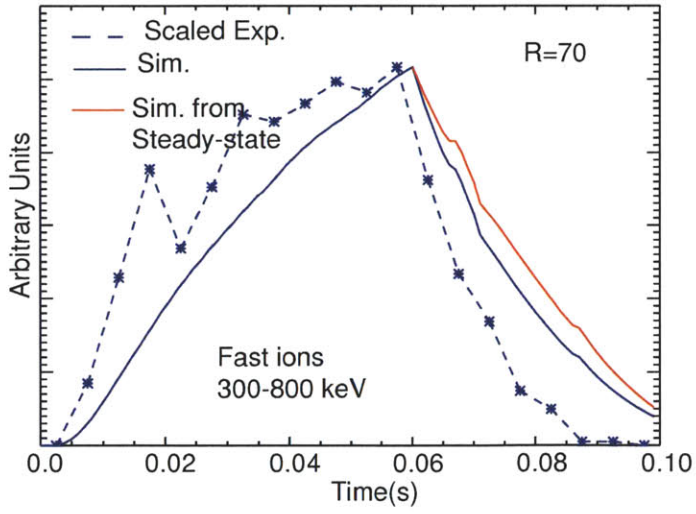

Figure 5-15: The relaxation of the steady-state distribution near resonance is normalized and shown along with the fully time dependent results.

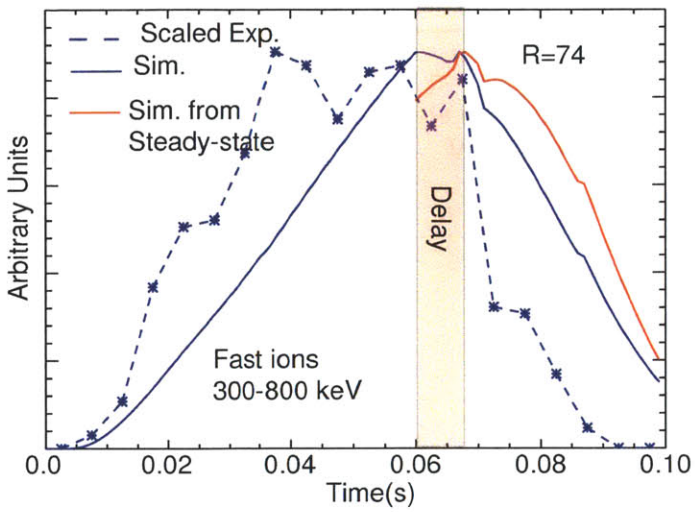

Figure 5-16: The relaxation of the steady-state distribution away from resonance is normalized and shown along with the fully time dependent results.

or evolving, fast-ion distribution functions.

Time steps

It is possible that the temporal resolution of the simulations has a significant effect on the evolution of the high energy fast-ions, and we examine this question by performing a simulation with finer time steps. We simulate the first 16 ms after the ICRF turns on with a much finer grid, starting with calls to AORSA every 0.1 ms for the first two ms and getting gradually larger. The simulation of the first 16 ms in this manner includes as much computational time as the full 60 ms simulation with calls to AORSA every 1 ms. The results of this fine time-stepping simulation are shown in Figure 5-17 where we see virtually no difference when we reduce the time step size. Increasing the internal time-steps in CQL3D has also been shown to make no discernable difference.

It is also possible that improved time-stepping algorithms may provide some better agreement between simulation and measurements [92]. The main purpose of these more advanced algorithms would be to tighten the self-consistent evolution between

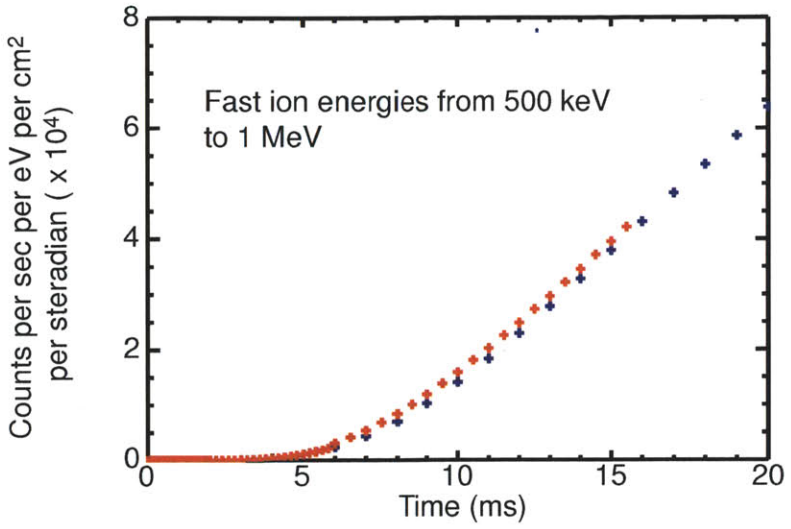

Figure 5-17: Shown are two simulations with the standard 1 ms time steps (blue) and a simulation with finer time stepping (red). Using finer time steps causes negligible change to the predicted distribution.

AORSA and CQL3D. However, our simple algorithm shows that the codes produce consistent predictions of absorbed power after a few iterations, so it is not expected that these advanced algorithms would produce better agreement. Indeed, initial attempts at self-consistent algorithms have not improved agreement with experiment.

Variable boron concentration

The ICRF antennas have been known to be a source for boron. This is seen by an increase in spectroscopic signal from boron when the ICRF turns on. We attempt to determine whether the discrepancy in the fast-ion distributions is caused by an improper input into the simulation of the B^{4+} concentration as a function of ICRF power.

To address this, we compare the signal from CXRS signal for two nearby boron lines in Figure 5-18. The line near 494.467 nm is the $n = 7 \rightarrow 6$ transition of B^{4+}. The line near 494.037 nm is the $n = 1, 2s3d \rightarrow 2s4f$ transition of B^{1+}. Because the

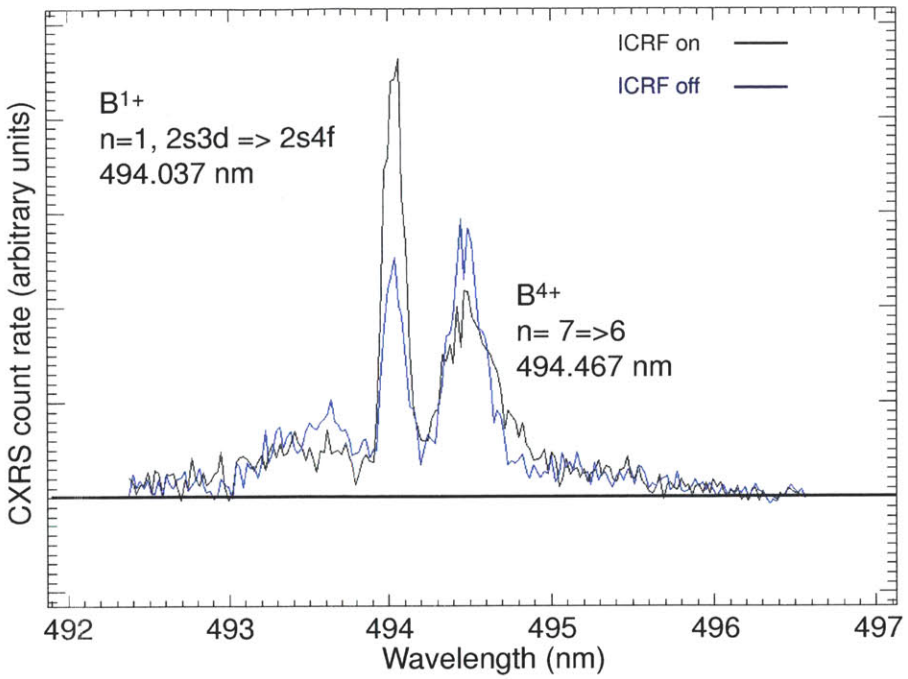

Figure 5-18: Boron concentrations for B^{4+} and B^{1+} lines are shown for ICRF on (black) and off (blue). Plot courtesy of K. Liao and the FRC-CXRS system.

high electron temperature in the plasma quickly strips off electrons, the B^{1+} line is only found at the plasma edge. The intensity of the boron is calculated by summing the area under the line emission curves, and thus, a relative comparison between the two curves is possible. Here we see that while the edge boron increases as a function of ICRF power by a factor of almost 2, the core boron shows a much more modest increase of ~10%. This suggests that it is unlikely that changes in the boron concentration in the core of the plasma are a candidate to explain the discrepancy.

Radial diffusion

CQL3D allows for a user specified anomalous radial diffusion as a function of both r/a and velocity. We examine whether the discrepancy is caused by anomalous radial diffusion that is not accounted in CQL3D's neoclassical treatment. Many attempts

were made to match the simulation and experiments through parametric scans of radial diffusion profiles. While it was possible to generate improved behavior with respect to time evolution for each energy bin, the simulated distributions never showed improvements with respect to energy. In fact, most of the simulations showed even worse agreement. Furthermore, theoretical gyro-kinetic estimates of radial diffusion for highly energetic ions were shown by Angioni and Peeters to be small [93].

Finite orbit effects

Previous experiments have found that including particle orbits is necessary for HHFW (High harmonic fast wave) or beam heated fast-ion distributions [82]. However, the discrepancies we see are ambiguous on whether finite orbit effects are playing an important role. The CNPA only detects ions at their banana tips. This is the precise location where the particle guiding center is on the CQL3D flux surface. Therefore, the zeroth order effect from finite banana widths does not affect the simulation. However, finite orbit effects can alter the absorption of energy of a fast-ion that does not have its banana tips at the resonance layer and could have significant effects on the collisional operator.

Quasi-linear violation

It is possible that the fast-ions are evolving in a way that cannot be simulated with the quasi-linear bounce-averaged RF operator used in CQL3D. Violation of quasi-linear theory arises when particles receive energy kicks that are comparable to their energy, $\Delta W \approx W$, on the timescale of a bounce period. This violates the assumption in quasi-linear theory that particle orbits are unperturbed by the ICRF. Moreover, there is another assumption in quasi-linear theory that successive kicks are decorrelated. An analytic calculation of an expected energy kick is given in Appendix A [94]. This calculation shows that a thermal particle with banana tips at the ICRF resonance receives a kick that is on order or greater than its pre-kick energy. Furthermore, even

a passing particle will receive a kick that is a significant fraction of its pre-kick energy. It is possible that these effects are not being handled properly in the simulation and could be a reason for some of the discrepancy.

Errors in other parameters

The electron temperatures used for the time-dependent simulations are the average values across all the simulation time bins. All departures due to sawteeth were smoothed over. Thus there is a difference between the actual temperature and the input one. Previous results indicate that the effects of sawteeth, and the errors in temperature should not play a large role (See Figures 4-5 and 3-12). Nevertheless, it is possible that there are some errors introduced from this simplification, and that the effects are amplified in the time-dependent analysis.

The simulations assumed that the value of $Z_{\text{eff}} = 1$ throughout the entire plasma and does not change as a function of time. The actual value of Z_{eff} is larger than 1 and this could account for some of the discrepancies, specifically in the turn-off.

Non-Maxwellian distributions at start

The simulation assumes that all distributions are Maxwellian at the time where the ICRF power turns on. Indeed, fast-ion counts do not appear on the CNPA after the ICRF power has been off for 40 ms. However, it is possible that the distribution has not fully relaxed to a Maxwellian in this time, and has a non-thermal tail at energies too low to be detected by the CNPA, or at pitch angles that the CNPA is unable to see. This could have an effect on the fast-ion rise time, and could be another source of the discrepancy. This effect can be investigated by repeating the experiment with longer on and off-times to ensure that the ion distribution has fully relaxed to a Maxwellian. However, multiple discharges will be required in order to obtain enough counts to measure the rise and relaxation of the fast-ion distribution.

CQL3D-DC

The CQL3D-DC (diffusion coefficient) code is currently in development [95]. This code follows particle orbits and calculates a diffusion coefficient directly from integrating the Lorentz force given equation for a particle using the AORSA wave-fields. Thus, the CQL3D-DC bypasses the quasi-linear diffusion coefficient. Initial results from CQL3D-DC have been presented, however due to limitations the simulation was only able to model the first few ms of the plasma. Nevertheless, the CQL3D-DC result shows that there is a considerable increase in pitch-angle scattering, resulting in a much faster rise to equilibrium of fast-ions along various sightlines. A simulation comparing the quasi-linear calculation and the diffusion coefficient calculation is shown in Figure 5-19. From this comparison, we see that the simulation using CQL3D-DC produces a more energetic fast-ion distribution along the CNPA sightline after 4 ms. These results provide a promising path forward to resolving the discrepancy in the time-dependence.

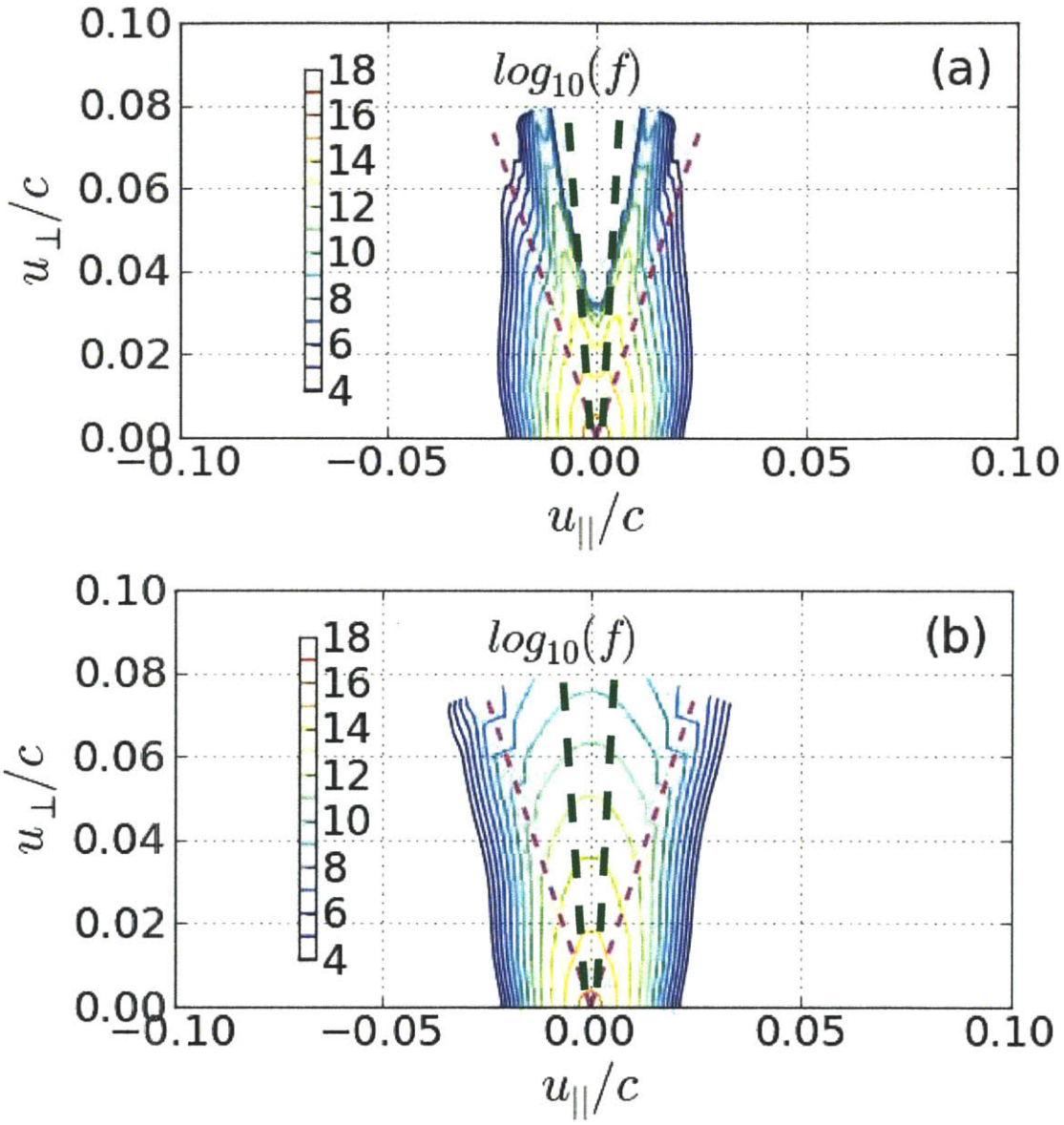

Figure 5-19: Distribution functions are shown for a simulation using quasi-linear theory (top) and the diffusion coefficient approach (bottom) [95]. The results at the $\rho \approx 0.15$ flux-surface are shown for a plasma distribution 4 ms after the ICRF power has been turned on. Dashed magenta lines indicate the trapped-passing boundary. The dashed green lines represent the pitch angle viewed by the $R = 70$ cm CNPA.

Chapter 6

Conclusions and Future Work

6.1 Concluding remarks

This thesis presented results from a new Compact Neutral Particle Analyzer that was installed on Alcator C-Mod, and analyzed the behavior of the fast-ion distribution as a function of plasma parameters. We discovered a strong dependence of the fast-ion distribution on plasma current. Higher current plasmas supported more energetic fast ion distributions, and it was thought that this dependence was related to the banana width, a parameter that scales inversely with current. We also found that the fast-ion tail energy did not increase with additional ICRF after a certain threshold.

In addition to the experimental development, a new synthetic diagnostic to simulate the fast-ion distribution at the CNPA was built into CQL3D, allowing for direct comparison between experiments and fast-ion distributions generated with the coupled AORSA-CQL3D codes. CQL3D is a zero orbit-width code, and simulations of plasmas at different currents were performed in order to ascertain whether the zero orbit-width assumption was sufficient to explain the strong current dependence of the fast-ion distribution. Surprisingly, the simulation and the experiment had good agreement for plasma currents ranging from 0.6 MA to 1.2 MA, and appeared to reproduce the current dependence of the fast-ion distribution seen in experiment.

The simulations also showed that at higher power levels, the damping profile broadens, but the effective temperature seems to saturate. The synthetic diagnostic agrees qualitatively with the results seen in the experimental measurement.

A second test of the AORSA-CQL3D simulation was performed by modulating the ICRF power and examining the periods immediately after turn-on and turn-off. These results showed large discrepancies between the experimental results and the simulations. Various possibilities for the discrepancies are given, although it is not clear at this time which of them are responsible.

6.2 Future work

This work describes the currently feasible measurements of fast-ion behavior in C-Mod and other tokamaks, but with new diagnostic and simulative capabilities, new areas of study are accessible. We outline possible areas where more research could produce interesting results starting with diagnostic upgrades and concluding with some advanced simulation capabilities.

6.2.1 Improvements to diagnostic capability

The CNPA is currently a very reliable diagnostic, operating on nearly every ICRF plasma. However, there are improvements that can increase the quality of the data.

The diagnostic aperture is currently hand-controlled and requires a cell access in order to adjust it. Often the aperture needs to be changed various times during the day for optimum fast-ion measurements. A remotely controlled aperture would greatly improve the CNPA's performance between discharges.

The F-Top CNPA functions well, but because of the shallow active-region of the detectors, it is limited to viewing fast-ions that are < 500 keV in energy. However, the shallow active region also ensures that the F-Top CNPA is immune from spurious photon counts. In this thesis, the F-Top CNPA played a supporting role to verify that

counts seen on J-Top were real and not photon induced. However, there is significant room to expand the role of the F-Top CNPA.

Currently the J-Top apertures are constant across all channels. However, the aperture was designed with removable sliding plates so that the apertures could differ across channels. Machining new plates could allow for sufficient statistics across a greater number of channels than was currently available in this thesis. For example, a channel at $R = 78$ cm did not have high enough particle counts to be used in the comparisons in Chapters 4 and 5. A larger aperture on this channel could have improved the count rates on that channel.

The detectors could be improved as well. Thicker foils might allow operation at larger aperture settings, improving count rates at the expense of the lower energy counts. Also, semi-conductor technology is always improving, and it is possible that a new detector substrate may become available in the next few years that would improve performance.

On the digitization side, automatic pulse-height counting systems have improved greatly over the past decades. A pulse-height counting system could remove the need for elaborate post-processing routines and reduce data storage demands. Benchmarking a pulse-height counting system against the current digitization system could show that the current pulse-height counting technologies are sufficient for the CNPA.

It should be noted that the CNPA was fortuitously able to calibrate the detectors with the Tandem Accelerator. It is not clear that this capability will be available in the future. Detector calibration once every few campaigns is desirable to monitor detector degradation. If the Tandem Accelerator is not available, an appropriate collaborating party will need to be found.

Moving away from the CNPA, new diagnostic capabilities will be available on C-Mod in the coming years. A FICX diagnostic to measure fast-ions has already been demonstrated for ^{3}He minority plasmas and there are plans to measure H minority plasmas as well. This diagnostic will provide a check on CNPA measurements, and

the results from H-minority operation are greatly anticipated [32].

A first generation lost-ion detector is currently planned to be installed in the 2011 vessel opening. Lost-ion detectors that can resolve energy and pitch-angle have made significant contributions to fast-ion research in other tokamaks such as NSTX, DIII-D, JET and ASDEX-U. Specifically lost-ion detectors are capable of measuring ejection of fast-ions due to MHD activity, either Alfvén Eigenmodes or sawteeth crashes. The CNPA does not monitor the correct pitch angles to provide measurements of these ejected ions.

This thesis finds some interesting dependencies of minority heated fast-ions on C-Mod. It may be interesting to design similar experiments on other tokamaks with minority heating, such as ASDEX or JET.

6.2.2 Improvements to simulation

Next generation simulations are currently becoming available with the rapid increase in computer capability. Full-orbit Monte-Carlo codes such as SMC or ORBIT-RF may provide improvements over CQL3D [81, 82]. While CQL3D is computationally faster, it is likely that the quasi-linear assumption that particles do not have large energy changes in a bounce time is violated in C-Mod. The full orbit codes could test this hypothesis directly.

CQL3D is currently being extended to calculate the diffusion coefficient directly from the wave-fields. Initial results from CQL3D show that the new diffusion coefficient provides a much faster fast-ion response than the quasi-linear calculation [95]. Also, in a parallel effort, CQL3D is being improved to include finite-orbit effects [96]. It is unclear whether this will have significant impact on the codes' agreement with experiment. However, this improvement will remove the assumption of zero-orbit widths that is clearly not valid, and thus should provide a better approximation to the real physics.

Lastly, with recent increases in computing capability and the use of computation

frameworks to manage large time-dependent massively-parallel simulations [97] it is now possible to run AORSA in a fully 3-D environment to better account for possible toroidal effects. These 3-D simulations would include the effects of multiple toroidal modes in the reconstruction of the quasi-linear diffusion coefficient and could provide a more realistic prediction of the energy kick received by ICRF heated ions.

Appendix A

ICRF Heating in Tokamak Plasmas

This appendix discusses the physics behind ion cyclotron resonance heating (ICRH). It begins with the derivation of the Cold Plasma Dispersion Relation (Section A.1) and focuses on the fast magnetosonic wave that is used for ICRH. Then it discusses a quasi-linear calculation to derive the energy imparted to a fast-ion at the resonance (Section A.2). Then this energy kick is evaluated for C-Mod parameters (Section A.3). Lastly, a brief discussion of mode conversion is presented (Section A.5)

A.1 Conductivity tensor - cold plasma dispersion relation

We begin by deriving a relationship between the plasma current and the electric field. Specifically we wish to solve for the conductivity tensor in the generalized Ohm's Law,

$$\vec{J} = \overleftrightarrow{\sigma} \cdot \vec{E}. \tag{A.1}$$

In isotropic media, the conductivity tensor $\overleftrightarrow{\sigma}$ is a constant and we recover the Ideal Ohm's Law,

$$\vec{E} = \eta \vec{J}, \tag{A.2}$$

where η is the resistivity of the material. However, in a strongly magnetized plasma, we cannot simplify the conductivity tensor to a constant, and we must solve for it completely.

$$\overleftrightarrow{\sigma} = \begin{bmatrix} \sigma_{xx} & \sigma_{xy} & \sigma_{xz} \\ \sigma_{yx} & \sigma_{yy} & \sigma_{yz} \\ \sigma_{zx} & \sigma_{zy} & \sigma_{zz}. \end{bmatrix} \tag{A.3}$$

To solve for the conductivity tensor, we consider a fluid model. Each species j of our fluid obeys conservation of momentum,

$$m_j n_j \left(\frac{\partial \vec{v_j}}{\partial t} + \vec{v_j} \cdot \nabla \vec{v_j} \right) = q_j n_j \left(\vec{E} + \vec{v_j} \times \vec{B} \right) - \nabla p_j - \sum_{j' \neq j} m_j n_j \nu_{jj'} \left(\vec{v_j} - \vec{v_j'} \right). \tag{A.4}$$

In the above equation, m is mass, n is density, $\vec{v}$ is velocity, q is charge, p is pressure, and $\nu_{jj'}$ is the collision frequency between species j and species j'.

First, we proceed with assumptions that lead us to the cold plasma dispersion relation. We assume that we ignore temperature effects,

$$\frac{\omega}{k_{||}} \gg v_{Th}, \tag{A.5}$$

where v_{Th} is the thermal velocity. The second assumption is that the wave phenomenon occurs much faster than collisional phenomena,

$$\omega \gg \nu_{jj'}. \tag{A.6}$$

These assumptions are fairly well satisfied at all points in the plasma with one notable exception. At the point of resonance, the parallel wave number, $k_{||}$ becomes very large and temperature effects are important in determining how the wave behaves at resonances.

Using these simplifications, we eliminate the pressure and collision term from Eq.

A.4, simplifying it to

$$m_j \left(\frac{\partial \vec{v_j}}{\partial t} + \vec{v_j} \cdot \nabla \vec{v_j} \right) = q_j \left(\vec{E} + \vec{v_j} \times \vec{B} \right). \tag{A.7}$$

We also note that this simplification has uncoupled the equations between the different plasma species, since the coupling was introduced only in the collision term.

To proceed further we write all quantities in the following Fourier series form,

$$Q = \sum_i Q_i \exp\left(-i\omega_i t + i\vec{k_i} \cdot \vec{x} \right).$$

More specifically, we assume that each quantity consists of an equilibrium quantity, and a perturbation quantity at the frequency of interest,

$$Q \approx Q_0 + Q_1 \exp\left(-i\omega t + i\vec{k} \cdot \vec{x} \right). \tag{A.8}$$

We ignore any higher order terms. We also assume that the plasma has no net flow and no equilibrium electric field: $\vec{v} = \vec{E} = \vec{0}$.

The fluid equations can be simplified with a convenient choice of coordinate system without any loss of generality. We assume that the equilibrium magnetic field is entirely in the z direction,

$$\vec{B} = B_0 \vec{z} + \vec{B_1}. \tag{A.9}$$

For now we want to consider a wave moving in any arbitrary angle relative to $\vec{B}$. However, without loss of generality, we can rotate our coordinate system so that the $\vec{k}$ is entirely in the x-z plane. Namely,

$$\vec{k} = k_z \vec{z} + k_x \vec{x}.$$

We now write down the three separate equations for Eq. A.4 ignoring all terms that are the product of two first-order terms. For now we consider only one species

and drop the j subscript.

$$-i\omega m v_{1x} = q\left(E_{1x} + v_{1y}B_0\right), \tag{A.10}$$

$$-i\omega m v_{1y} = q\left(E_{1y} - v_{1x}B_0\right), \tag{A.11}$$

$$-i\omega m v_{1z} = qE_{1z}. \tag{A.12}$$

Solving for $\vec{v}$, and using the definition for the cyclotron frequency, $\omega_c = \frac{qB}{m}$, gives,

$$\begin{aligned} v_{1x} &= \frac{\frac{q}{m}\left(i\omega E_{1x} - \omega_c E_{1y}\right)}{\omega^2 - \omega_c^2}, \\ v_{1y} &= \frac{\frac{q}{m}\left(i\omega E_{1y} + \omega_c E_{1x}\right)}{\omega^2 - \omega_c^2}, \\ v_{1z} &= \frac{q}{m}\frac{iE_{1x}}{\omega}. \end{aligned}$$

We note that ω_c is positive for ions and negative for electrons. Before we can calculate $\overleftrightarrow{\sigma}$ we need to define the plasma species of interest. For this calculation we assume that the plasma consists of a singly ionized ion species and electrons. Even though we are predominantly interested in the wave interaction with a minority species in this thesis, provided the plasma is predominantly one species, the governing wave physics away from the resonance are determined by the dominant species.

For equilibrium we demand that the plasma obeys the quasi-neutrality principle, namely that in any closed volume, the total charge is 0. Since all our ions are only singly ionized, this is satisfied if

$$n_{e0} = n_{i0} = n_0.$$

Then $\vec{J}$ becomes

$$\vec{J} = eZn_i\vec{v_i} - en_e\vec{v_e} = en_0\left(\vec{v_i} - \vec{v_e}\right),$$

where e is used for the unsigned elementary charge.

Finally we write out the conductivity tensor terms (see Eq. A.3).

$$\sigma_{xx} = \sigma_{yy} = ie^2 n_0 \left(\frac{1}{m_i} \frac{\omega}{\omega^2 - \omega_{ci}^2} + \frac{1}{m_e} \frac{\omega}{\omega^2 - \omega_{ce}^2} \right)$$
$$\sigma_{xy} = -\sigma_{yx} = -e^2 n_0 \left(\frac{1}{m_i} \frac{\omega_{ci}}{\omega^2 - \omega_{ci}^2} + \frac{1}{m_e} \frac{\omega_{ce}}{\omega^2 - \omega_{ce}^2} \right)$$
$$\sigma_{zz} = \frac{ie^2 n_0}{\omega} \left(\frac{1}{m_i} + \frac{1}{m_e} \right)$$
$$\sigma_{xz} = \sigma_{yz} = \sigma_{zx} = \sigma_{zy} = 0.$$

We next obtain a relationship between $\vec{J}$ and $\vec{E}$ from electromagnetic wave properties.

Beginning with Maxwell's Equations:

$$\nabla \times \vec{E} = -\frac{\partial \vec{B}}{\partial t}, \tag{A.13}$$
$$\nabla \times \vec{B} = \mu_0 \vec{J} + \frac{1}{c^2} \frac{\partial \vec{E}}{\partial t}, \tag{A.14}$$
$$\nabla \cdot \vec{E} = \frac{\rho}{\epsilon_0}, \tag{A.15}$$
$$\nabla \cdot \vec{B} = 0. \tag{A.16}$$

We assume all quantities are expressed as we did in Eq. A.8 and that leads to the linearized Maxwell's equations:

$$i\vec{k} \times \vec{E}_1 = i\omega \vec{B}_1, \tag{A.17}$$
$$i\vec{k} \times \vec{B}_1 = \mu_0 \vec{J}_1 - \frac{i\omega}{c^2} \vec{E}_1, \tag{A.18}$$
$$i\vec{k} \cdot \vec{E} = \frac{\rho}{\epsilon_0}, \tag{A.19}$$
$$i\vec{k} \cdot \vec{B}_1 = 0. \tag{A.20}$$

We eliminate $\vec{B}_1$ by taking the curl of Eq. A.17, giving the linearized homogeneous wave equation,

$$i\vec{k} \times i\vec{k} \times \vec{E}_1 = i\omega \left(i\vec{k} \times \vec{B}_1 \right) = i\omega \left(\mu_0 \vec{J}_1 - \frac{i\omega}{c^2} \vec{E}_1 \right). \tag{A.21}$$

This equation is simplified, using the substitution $J_1 = \overleftrightarrow{\sigma} \cdot \vec{E}_1$ giving,

$$\vec{k} \times \vec{k} \times \vec{E}_1 = -\frac{\omega^2}{c^2} \vec{E}_1 - i\omega\mu_0 \overleftrightarrow{\sigma} \cdot \vec{E}_1.$$

We rearrange the above equation into the standard form by substituting for the index of refraction,

$$\vec{N} = \frac{\vec{k}c}{\omega},$$

where we use the capital $\vec{N}$ to distinguish the anisotropic refraction index from the plasma density. This substitution leads to the standard form of the dispersion relation,

$$\vec{N} \times \vec{N} \times \vec{E}_1 = -\left(\vec{E}_1 + \frac{i\mu_0}{c^2\omega} \overleftrightarrow{\sigma} \cdot \vec{E}_1 \right) = -\overleftrightarrow{K} \cdot \vec{E}_1, \tag{A.22}$$

where we have defined the dielectric tensor, $\overleftrightarrow{K}$, as:

$$\overleftrightarrow{K} = \overleftrightarrow{I} + \frac{i}{\epsilon_0\omega} \overleftrightarrow{\sigma}. \tag{A.23}$$

In Eq. A.23, $\overleftrightarrow{I}$ is the unit tensor and we have made use of the identity $c^2 = \frac{1}{\epsilon_0\mu_0}$.

Equation A.22 can also be written out in component form, and making no assumptions on the direction of the wave, this gives,

$$\left(N_y^2 + N_z^2 - K_{xx}\right) E_x - \left(N_x N_y + K_{xy}\right) E_y - \left(N_x N_z - K_{xz}\right) E_z = 0$$
$$-\left(N_x N_y + K_{yx}\right) E_x + \left(N_x^2 + N_z^2 - K_{yy}\right) E_y - \left(N_y N_z + K_{yz}\right) E_z = 0$$
$$-\left(N_x N_z + K_{zx}\right) E_x - \left(N_y N_z + K_{zy}\right) E_y + \left(N_x^2 + N_y^2 - K_{zz}\right) E_z = 0.$$

We wish to find all possible conditions that allow this system of equations to have a non-trivial solution. To get a solution, the determinant of the component matrix must be 0,

$$\begin{vmatrix} N_y^2 + N_z^2 - K_{xx} & -N_x N_y - K_{xy} & -N_x N_z - K_{xz} \\ -N_x N_y - K_{yx} & N_x^2 + N_z^2 - K_{yy} & -N_y N_z - K_{yz} \\ -N_x N_z - K_{zx} & -N_y N_z - K_{zy} & N_x^2 + N_y^2 - K_{zz}. \end{vmatrix} = 0 \tag{A.24}$$

Writing out the actual determinant is overly cumbersome, and we make use of our simplifications before proceeding further. We use our geometrical assumptions (see Eq. A.9) to reduce the dielectric tensor. Furthermore, for simplification, we write the dielectric tensor in the Stix notation:

$$\overleftrightarrow{K} = \begin{bmatrix} S & -iD & 0 \\ iD & S & 0 \\ 0 & 0 & P. \end{bmatrix} \tag{A.25}$$

where,

$$
\begin{aligned}
S &= \tfrac{1}{2}\left(R+L\right), \\
D &= \tfrac{1}{2}\left(R-L\right), \\
P &= 1-\frac{\omega_{pe}^2+\omega_{pi}^2}{\omega^2}, \\
R &= 1-\frac{\omega_{pe}^2}{\omega\left(\omega+\omega_{ce}\right)}-\frac{\omega_{pi}^2}{\omega\left(\omega+\omega_{ci}\right)}, \\
L &= 1-\frac{\omega_{pe}^2}{\omega\left(\omega-\omega_{ce}\right)}-\frac{\omega_{pi}^2}{\omega\left(\omega-\omega_{ci}\right)}.
\end{aligned}
$$

In the above equations, we use the definition of the plasma frequency,

$$\omega_{pj}^2 = \frac{q_j^2 n_j}{m_j \epsilon_0}$$

We rewrite Eq. A.24 using the Stix notation and also using our geometry assumptions,

$$N_x = N_\perp, N_y = 0, N_z = N_\parallel,$$

giving,

$$\begin{vmatrix} N_\parallel^2 - S & iD & -N_\perp N_\parallel \\ -iD & N_\parallel^2 + N_\perp - S & 0 \\ -N_\perp N_\parallel & 0 & N_\perp^2 - P \end{vmatrix} = 0. \tag{A.26}$$

We are interested in plasma waves near the cyclotron frequency of the minority ions. The waves we launch are fast magnetosonic waves from RF antennas, and assumed to have a fixed value of $N_\parallel$ that is determined by the antenna geometry. Therefore, we write out the determinate as a biquadratic in $N_\perp$,

$$SN_\perp^4 + \left[\left(N_\parallel^2 - S\right)\left(S + P - N_\parallel^2\right) + D^2\right] N_\perp^2 + P\left[\left(N_\parallel^2 - S\right)^2 - D^2\right] = 0. \tag{A.27}$$

Since we are interested in ion cyclotron heating we consider launched waves with

the following orderings,

$$\omega \sim \omega_{ci} \ll \omega_{pi} \ll \omega_{pe} \sim \omega_{ce},$$
$$\frac{\omega_{pe}^2}{\omega_{ci}\omega_{ce}} \approx \sqrt{\frac{m_i}{m_e}} \ll \frac{m_i}{m_e} \approx \frac{\omega_{pi}^2}{\omega_{ci}^2}.$$

Using these we can simplify the equations for S, P, and D as follows:

$$S \approx \frac{-\omega_{pi}^2}{\omega^2 - \omega_{ci}^2},$$
$$D \approx \frac{\omega_{ci}}{\omega}\frac{\omega_{pi}^2}{\omega^2 - \omega_{ci}^2} + \frac{\omega_{pe}^2}{\omega\omega_{ce}} = \frac{\omega}{\omega_{ci}}\frac{\omega_{pi}^2}{\omega^2 - \omega_{ci}^2},$$
$$P = -\frac{\omega_{pe}^2}{\omega^2}.$$

We simplify further by noting that,

$$\frac{S}{P} \sim \frac{m_e}{m_i} \ll 1,$$

and assuming,

$$N_\parallel \sim S \ll P.$$

With a little effort, Eq. A.27 can be separated into two roots giving,

$$N_\perp^2 \approx \frac{P\left(S - N_\parallel^2\right)}{S} \tag{A.29}$$
$$N_\perp^2 \approx \frac{\left(N_\parallel^2 - S\right)^2 - D^2}{S - N_\parallel^2} = \frac{\left(R - N_\parallel^2\right)\left(L - N_\parallel^2\right)}{S - N_\parallel^2}. \tag{A.30}$$

It is the second root that is interesting for ICRH minority heating. This wave has two cutoffs and one resonance. The cutoffs occur when the numerator in Eq. A.30 is zero, and the resonances occur when the denominator is zero. The cutoffs occur on the edges of the plasma requiring the wave to tunnel through a small evanescent region to reach the plasma center. However, we are more interested in the wave's

behavior at the cyclotron resonance $\omega = \omega_{ci}$.

More detail of the wave behavior at the resonance is handled in the next sections. However, it is relatively simple to determine the wave polarization at resonance. We o this by comparing E_y to E_x. There are many ways to do this, but the easiest is to consider the middle line in Eq. A.26. Comparing the two electric field components gives,

$$E_y = \frac{iD}{N_\perp^2 + N_\parallel^2 - S} E_x,$$

At the cyclotron resonance $D, S \to \pm\infty$ and $\frac{D}{S} = -1$. However from Eq. A.30 we can show that at $\omega = \omega_{ci}$,

$$N_\perp^2 \approx \omega_{pi}^2/\omega_{ci}^2 \tag{A.31}$$

is finite.

Therefore,

$$E_y = iE_x. \tag{A.32}$$

This corresponds to a circularly polarized wave in the clockwise, or electron diamagnetic direction. Unfortunately, ions gyrate around the field lines counterclockwise, or ion diamagnetic direction. The result is that there is almost no absorption of the fast wave at the cyclotron resonance for the main ion species.

There are two solutions to this problem. One solution is to heat at a harmonic of the cyclotron frequency. A second solution is to introduce a minority species with $n_m \ll n_b$, the density of the minority species is much less than the density of the bulk species. In this limit, the wave acquires a left circularly polarized component that can interact with the minority ions at their fundamental cyclotron frequency [98]. In Alcator C-Mod this is accomplished by using naturally occurring hydrogen in bulk deuterium (or sometimes helium) plasma. For most heating scenarios, including the bulk of plasmas that appear in this thesis,

$$\frac{n_H}{n_D} < 0.1.$$

A.2 Absorption from quasi-linear theory

Calculation of the plasma absorption is a complicated process. The assumptions that we used to derive the cold plasma dispersion relation are not valid near the absorption layer. This section and the following discuss the quasi-linear theory approximation that is typically used to calculate absorbed power. We present an overview of quasi-linear theory leading to a calculation of the Stix power absorption in C-Mod. In the next section, we use the same quasi-linear theory to calculate the kick given to a single particle passing through the resonance layer in C-Mod [94]. The derivation here begins with Stix [55] and follows the excellent overview given by Hammett [67].

We start with the unlinearized forms of Eqs. A.10 and A.11 in the presence of a wave with frequency ω,

$$\frac{dv_x}{dt} = \frac{q}{m} E_x \cos(\omega t) + \omega_c v_y,$$
$$\frac{dv_y}{dt} = \frac{q}{m} E_y \cos(\omega t) - \omega_c v_x.$$

Here, q is the signed electric charge. Writing these equations in terms of the circularly polarized electric field,

$$E_\pm = \frac{1}{2}\left(E_x \pm E_y\right),$$

and the velocity,

$$u = v_x + i v_y,$$

gives,

$$\frac{du}{dt} + i\omega_c u = \frac{q}{m}\left(E_+ e^{-i\omega t} + E_- e^{+i\omega t}\right). \tag{A.34}$$

We are interested in a particle as it is moving along a field line. In this case, ω_c, a function of the magnetic field strength, changes, and we can parametrize it as a function of time, $\omega_c = \omega_c(t)$. Furthermore, we are only interested in the E_+ component, because it is resonant with the ions. Solving the differential equation in

Eq. A.34 gives,

$$u(t_1) = \exp\left(-i\int_{t_0}^{t_1}\omega_c dt\right)\left[u(t_0) + \frac{q}{m}E_+\int_{t_0}^{t_1}\exp\left(-i\int_{t_0}^{t}(\omega-\omega_c)dt'\right)dt\right], \quad \text{(A.35)}$$

where the first term is the homogeneous solution and the second term is the particular solution that arises from the electric field driving term. In the above equation we have used the simplified resonance condition of $\omega = \omega_c$. However, the actual resonance condition should be written as $\omega = \omega_c + v_\parallel k_\parallel$, where the resonance is Doppler-broadened due to finite $k_\parallel$. However, we neglect the Doppler-broadening term as it does not have a large effect on the calculation of the energy imparted to a single particle passing through the resonance layer (see Hammett 2.4.8 [67]).

In general the particle phase and the wave phase are random with respect to each other. Therefore, the change in energy is due entirely to the electric field term and is,

$$\delta W_\perp = \frac{q^2}{2m}\left|E_+\int_{t_0}^{t_1}\exp\left(-i\int_{t_0}^{t}(\omega-\omega_c)dt'\right)dt\right|^2. \quad \text{(A.36)}$$

We evaluate both integrals by expanding ω_c about the cyclotron frequency ω_c,

$$\omega_c \approx \omega\left(1 + \frac{v_\parallel}{L_\parallel}t\right) \quad \text{(A.37)}$$

$L_\parallel$ is the parallel scale length given by $1/L_\parallel = 1/B \cdot dB/ds$ where s is taken along the magnetic field line. The integral then is,

$$\begin{aligned}\int_{t_0}^{t_1}\exp\left(-i\int_{t_0}^{t}(\omega-\omega_c)dt'\right)dt &= \int_{t_0}^{t_1}\exp\left(\frac{1}{2}\left[-i\omega\frac{v_\parallel}{L_\parallel}(t^2-t_0^2)\right]\right)dt = \\ &= \left(\frac{2\pi i L_\parallel}{\omega v_\parallel}\right)^{\frac{1}{2}}. \quad \text{(A.38)}\end{aligned}$$

An analytic solution to the second integral is obtained by setting $t_0 = 0$ and $t_1 \to \infty$. The goal is to get an estimate of how much energy is absorbed on average by a particle passing near the resonance layer between time t_0 and time t_1. This average energy

gain per transit through the resonance surface is given by,

$$\delta W_\perp = \frac{1}{2}m\left[|u(t_1)|^2 - |u(t_0)|^2\right] = \frac{m}{2}\left|\frac{q}{m}E_+\right|^2 \cdot \frac{2\pi L_\parallel}{\omega v_\parallel}. \tag{A.39}$$

We make a brief detour to calculate the power deposited to a particle by multiplying $\delta W_\perp$ with the rate that a particle executes a transit, ν_b. Stix's result for the power density is given here (in mks) without derivation,

$$P_{\text{Stix}} = \frac{n_H q}{B}\frac{R}{r|\sin(\theta)|}|E_+|^2, \tag{A.40}$$

where n_H represents the density of the resonant minority hydrogen ions and q is the plasma safety factor.

Stix's derivation is invalid on the midplane ($\theta = 0$) and on axis ($r = 0$). The $\theta = 0$ singularity arises from the linear approximation of parallel scale length, $L_\parallel$. The $r = 0$ singularity arises from neglecting the Doppler broadening $\vec{k}\cdot\vec{v}$ in the resonance. For now, we consider the Stix power away from these singularities. First, we need estimates of the magnitude of the electric field. We calculate the electric field magnitude by evaluating the Poynting flux,

$$\vec{S} = \frac{1}{2}\vec{E}\times\vec{H}. \tag{A.41}$$

From the linearized Maxwell's Equations we get $\vec{H} = \vec{k}\times\vec{E}/2\mu_0\omega$. Then the Poynting flux can be written as,

$$\vec{S} = \frac{1}{2\mu_0\omega}\vec{E}\times(\vec{k}\times\vec{E}) = \frac{1}{2\mu_0\omega}\left[|E|^2\vec{k} - (\vec{k}\cdot\vec{E})\vec{E}\right]. \tag{A.42}$$

The $\vec{k}\cdot\vec{E}$ term is small and is neglected by Stix and Hammett. Using the definition for $N = ck/\omega$ gives

$$|\vec{S}| = \frac{1}{2}\epsilon_0 cN|\vec{E}|^2 = 1.33\times10^{-3}NE^2(\text{W/m}^2) \tag{A.43}$$

From Eq. A.31 we use typical C-Mod parameters of $n_i = 10^{20}$ m^{-3} and B = 5.4 T and get $N \approx 36$. The Poynting flux is the flux of electromagnetic power through an area. For C-Mod, we have 2 MW of ICRF power that passes through a region of the plasma that we model as being a cylinder with height, $h = 20$ cm located at the ICRF resonance layer of $R_0 = 68$ cm. Then the magnitude of the Poynting flux is,

$$S = \frac{P_{\mathrm{RF}}}{2\pi R_0 H} = 2.34(\mathrm{W/m^2}). \tag{A.44}$$

Finally, we estimate the electric field from Eq. A.43 and get that $|E|$. Assuming that the minority contribution is dilute enough to not affect the wave physics, it can be shown that $|E_+| = \frac{2}{3}|E|$ [98], giving a result that is similar to the prediction by AORSA of 3-4 kV/m.

Using 4 kv/m for the magnitude of the component of the electric field that is resonant with the minority ions, we now calculate the absorbed power from Stix (Eq. A.40). We use r =0.1 m and standard C-Mod minority density of $n_H = 0.07 \times 10^{20}$ and get an absorbed power density of ~23 MV/m^3. This is reasonably close to the results from AORSA-CQL3D, which calculates a peak flux-surface average power density of ~25 MV/m^3 (Figure 4-4).

A.3 Energy to a single resonant ion

We return to the calculation of the energy imparted to a single thermal resonant ion. This is accomplished by considering Eq. A.39. However, before we can evaluate that equation we need to know $L_\parallel$, the parallel scale length. We start with the definition of $L_\parallel$ and invoke the chain rule several times,

$$\frac{1}{L_\parallel} = \frac{1}{B}\frac{dB}{ds} = \frac{1}{B}\frac{dB}{dR}\frac{dR}{d\theta}\frac{d\theta}{d\phi}\frac{d\phi}{ds},$$

and use the following geometrical identities,

$$\frac{1}{B} = \frac{R}{B_0 R_0}; \frac{dB}{dR} = -\frac{B_0 R_0}{R^2}; \frac{dR}{d\theta} = -r\sin(\theta); \frac{d\theta}{d\phi} = \frac{1}{q}; \frac{d\phi}{ds} \approx \frac{2\pi}{2\pi R}.$$

Combining all the above definitions gives a final equation of,

$$L_{\|} = \frac{R^2 q}{r\sin(\theta)}. \tag{A.45}$$

Here, q is the plasma safety factor and θ is the angle with respect to the plasma midplane (not the magnetic field). The above derivation is only valid away from the magnetic axis and the plasma midplane. For typical C-Mod parameters at ICRF resonance of $q = 1.1$, $R = 0.68$, $a = 0.22$, $r = 0.1$, and $\sin(\theta) = 1$, we get that $L_{\|} \approx$ 5 m.

To calculate the maximum energy imparted to a thermal ion, we consider an ion with banana tips at the resonance layer. However, before we consider this case, we examine the simpler case of energy imparted to a passing ion. This case is simpler because we can take $v_{\|}$ to be constant. A thermal ion with $W_{\|} = 1$ keV has parallel velocity, $v_{\|} \approx 4.4 \times 10^5$. Then using the previous calculated values for $|E_+| = 7$ keV/m and $L_{\|} = 5$ m we can calculate that the change in energy for a single transit, $\delta W_{\perp} = 330$ eV.

For the particle that has a banana tip at the resonance, we cannot use the approximation given in Eq. A.37. Instead we have to use the more general form,

$$\omega_c{}' = \omega\left(1 + \frac{s(t)}{L_{\|}}\right).$$

In order to calculate the particle position, $s(t)$ we write the force equation for the particle in a changing magnetic field.

$$F_{\|} = \mu\frac{dB}{ds} = \mu\frac{B}{L_{\|}} = -ma_{\|}$$

Where μ is the first adiabatic invariant and $a_{\|}$ is the particle acceleration in the parallel direction. Then we have the following equations for particle velocity and position,

$$v_{\|}(t) = -\frac{\mu B}{mL_{\|}}t \; ; \; s(t) = -\frac{\mu B}{2m{L_{\|}}^2}t^2,$$

where we have set the particle position at $t = 0$ to be at the banana tips. So at $t = 0$, we set $s = 0$, and we have $v_{\|} = 0$ because the particle is at its turning point. Our new expression for the particle cyclotron frequency is

$$\omega_c{}' = \omega\left(1 - \frac{\mu B}{2mL_{\|}^2}t^2\right).$$

We now use the above expression in Eq. A.36. The solution to the inner integral can be immediately evaluated,

$$\int_{t_0}^{t}(\omega - \omega_c)dt = \frac{\omega\mu B}{2mL_{\|}^2}\frac{t^3 - t_0^3}{3} = \frac{t^3 - t_0^3}{\tau^3}. \tag{A.46}$$

In Eq. A.46 we have defined a time constant τ as,

$$\tau = \left(\frac{6mL_{\|}^2}{\omega\mu B}\right)^{1/3}$$

The outer integral then takes the form,

$$\exp\left(\frac{-it_0^3}{\tau^3}\right)\int_{t_0}^{t_1}\exp\left(\frac{it^3}{\tau^3}\right)dt = \exp\left(\frac{-it_0^3}{\tau^3}\right)\tau\int_{t_0/\tau}^{t/\tau}\exp\left(\frac{it^3}{\tau^3}\right)d(t/\tau) \tag{A.47}$$

In order to evaluate the integral analytically, we need to take the limits to be $-\infty$ and $+\infty$. Then we can use the identity,

$$\int_{-\infty}^{\infty}e^{ix^3}dx = \frac{\Gamma(1/3)}{\sqrt{(3)}} \approx 1.55,$$

Finally, we can take the solution and put it into Eq. A.36. The exponential terms

vanish when taking the magnitude, leaving the solution,

$$\delta W_\perp = \frac{q^2|E_+|^2}{2m}\tau^2(1.55)^2. \tag{A.48}$$

All that remains is to calculate the magnitude of $\delta W_\perp$ using C-Mod parameters.

$$\tau^3 = \frac{6mL_\parallel^2}{\omega\mu B} = \frac{6mL_\parallel^2}{\omega W_\perp} = 3\times 10^{-18}\ \mathrm{s}^3, \tag{A.49}$$

where we have used $W_\perp = 2$ keV, $L_\parallel = 5$, and $\omega = \omega_c$. Using, the electric field calculated above of $|E_+| = 4$ kV/m, we get a value of $\delta W_\perp \approx 2.4$ keV. This result is problematic, because the quasi-linear assumption requires that $\delta W_\perp$ is small compared to $W_\perp$. For the passing particle, we calculate $\delta W_\perp \approx 0.15\ \times W_\perp$. However, for a particle with banana tips at the resonance we have $\delta W_\perp > W_\perp$. This implies that quasi-linear theory is invalid for a large population of resonant ions on C-Mod. These ions experience kicks that are much larger than predictable by quasi-linear theory.

As ions become more energetic, $W_\perp$ will be larger and the resultant kick will be small in comparison to the particle energy. Quasi-linear theory will become valid again for these energetic particles. Nevertheless, there could be a discrepancy in the initial evolution of the distribution function, when the ICRF waves are damping on thermal ions.

A.4 Full Quasi-Linear Expression

This section will write the equations used in AORSA to calculate the RF quasi-linear operator, $Q(f)$. The quasi-linear diffusion equation is given by,

$$Q(f) = \frac{\partial}{\partial\vec{v}}\overleftrightarrow{D}\frac{\partial f}{\partial\vec{v}} \tag{A.50}$$

which is a standard diffusion equation. The quasi-linear approach involves computing the change in the velocity vector, $\delta\vec{v}\delta\vec{v}$, that arises from the electric fields averaged over a particle orbit. A simplistic approach for this calculation was given in the previous two sections where we only considered fields that existed at the resonance layer and computed the increase of one component of velocity space for a passing particle and a particle with its banana tips at the resonance. This section will provide the general solution for the quasi-linear equation.

Expanding the derivatives in components yields the following form of the diffusion operator,

$$Q(f) = \frac{1}{u^2}\frac{\partial}{\partial u}\left(B\frac{\partial f}{\partial u} + C\frac{\partial f}{\partial \theta}\right) + \frac{1}{u^2 \sin\theta}\frac{\partial}{\partial \theta}\left(E\frac{\partial f}{\partial u} + F\frac{\partial f}{\partial \theta}\right). \tag{A.51}$$

In the above equation, u represents normalized speed. It is normalized by the user input variable E_{norm} which represents the maximum allowable energy. θ represents the pitch angle at the midplane. The third component of velocity space represents the phase. Quasi-linear theory requires that the phases be decorrelated, which sets these derivatives to 0.

The diffusion tensor $\overleftrightarrow{D}$ is broken up into four scalar coefficients, $A, B, C,$ and$D$. These represent the contributions to $v_u v_u$, $v_u v_\theta$, $v_\theta v_u$ and $v_\theta v_\theta$ respectively. Calculating the coefficients is a difficult task, the result computed by E.F. Jaeger is given

below [89].

$$B = \alpha \mathrm{Re}\left[\sum_{l=-\infty}^{\infty} \frac{\pi\sqrt{\mu}}{|N_{\|}|}\left(\sum_{\vec{k}_2} \epsilon_{\vec{k}_2}^{*T} \cdot \vec{a}_l^{(2)T}\right)\left(\sum_{\vec{k}_1} \vec{a}_l^{(1)} \cdot \epsilon_{\vec{k}_1}\right)_{u_{\|},\mathrm{res}}\right],$$

$$C = \alpha \mathrm{Re}\left[\sum_{l=-\infty}^{\infty} \frac{\pi\sqrt{\mu}}{|N_{\|}|}\frac{1}{u_{\|,\mathrm{res}}\sin\theta}\left(\frac{l\omega_c}{\omega} - \sin^2\theta\right)\left(\sum_{\vec{k}_1} \vec{a}_l^{(1)} \cdot \epsilon_{\vec{k}_1}\right)_{u_{\|},\mathrm{res}}\right],$$

$$E = \alpha \mathrm{Re}\left[\sum_{l=-\infty}^{\infty} \frac{\pi\sqrt{\mu}}{|N_{\|}|}\frac{1}{u_{\|,\mathrm{res}}}\left(\frac{l\omega_c}{\omega} - \sin^2\theta\right)\left(\sum_{\vec{k}_2} \epsilon_{\vec{k}_2}^{*T} \cdot \vec{a}_l^{(2)T}\right)\left(\sum_{\vec{k}_1} \vec{a}_l^{(1)} \cdot \epsilon_{\vec{k}_1}\right)_{u_{\|},\mathrm{res}}\right],$$

$$F = \alpha \mathrm{Re}\left[\sum_{l=-\infty}^{\infty} \frac{\pi\sqrt{\mu}}{|N_{\|}|}\frac{1}{u_{\|,\mathrm{res}}\sin\theta}\left(\frac{l\omega_c}{\omega} - \sin^2\theta\right)^2\left(\sum_{\vec{k}_1} \vec{a}_l^{(1)} \cdot \epsilon_{\vec{k}_1}\right)_{u_{\|},\mathrm{res}}\right],$$

where,

$$\alpha = \frac{\epsilon_0\omega_p^2}{8\omega e E_{\mathrm{norm}}\Delta u_{\|}}.$$

In the above equations, μ is the magnetic moment normalized to E_{norm}, and l represents the harmonic number. The vector $\vec{a}_l$ is given by,

$$\vec{a}_l = \left[u_{\perp}J_{l+1}\left(\frac{k_{\perp}v_{\perp}}{\omega_c}\right),\ u_{\perp}J_{l-1}\left(\frac{k_{\perp}v_{\perp}}{\omega_c}\right),\ \sqrt{2}u_{\|}J_l\left(\frac{k_{\perp}v_{\perp}}{\omega_c}\right)\right],$$

where v is the velocity without normalization, and J represents the Bessel Function. The rotated field vector, ϵ is given by,

$$\epsilon = \frac{1}{\sqrt{2}}(E_{\alpha} - iE_{\beta})\exp\left(i\vec{k}\cdot\vec{r} + (l+1)\beta\right),$$
$$\frac{1}{\sqrt{2}}(E_{\alpha} + iE_{\beta})\exp\left(i\vec{k}\cdot\vec{r} + (l-1)\beta\right),$$
$$E_{\|}\exp\left(i\vec{k}\cdot\vec{r} + l\beta\right).$$

The electric field component E_{α} is given by $E \cdot \hat{e}_{\alpha}$ where $\hat{e}_{\alpha}$ is the part of the

$\hat{e}_x$ vector perpendicular to $\vec{B}$. $\hat{e}_\beta$ is in the direction of $\vec{B} \times \hat{e}_\alpha$. To evaluate the coefficients, it is necessary to sum over various wave harmonics. The exact number of wave harmonics included in the calculation is input by the user. The simulations in this thesis generally use a 128 by 128 grid of modes.

A.5 Mode conversion

Mode conversion is a plasma wave phenomenon that occurs when the conditions in the plasma are such that more than one wave can propagate. When this occurs, there is a possibility for the original plasma wave to convert to the second wave. For the waves we are interested in, there are possible mode conversions to two other plasma waves. These are the Ion Cyclotron wave and the Ion Bernstein Wave, a hot plasma wave. In the minority ICRF heating scheme, these waves cannot be launched directly into the plasma, and are only accessed through mode conversion of the fast magnetosonic wave.

The fraction of the wave power that is mode converted to either of these waves is directly related to the minority concentration. At high minority concentrations a large percentage of this wave power is mode converted and only a small percentage is absorbed by the minority ions. Alcator C-Mod uses mode conversion for alternate heating and current drive schemes [99], but these areas are not a focus of this thesis. Instead, we desire minority fractions where $\frac{n_H}{n_D} < 0.1$. At these minority concentrations mode conversion is small and there is strong damping of the fast magnetosonic wave on the minority ions.

Appendix B

Energy and Spatial Calibrations

B.1 Energy calibration

The CNPA detectors were calibrated against a source of protons of known energy. The calibration process not only provided the voltage-energy curves for our detector, but also verified that the detectors did not degrade in performance over the campaign. The energy calibration was performed using a proton beam generated by the CLASS Tandetron accelerator. The beam was backscattered off a thick molybdenum target at a 90° angle. The detector was connected to the standard analyzing electronics described in Chapter 2. However, it was not possible to move the CPCI digitizer near the accelerator, and therefore, a multi-channel pulse-height analyzer (MCA) was used. A cartoon of the calibration setup is shown in Figure B-1. The detectors were calibrated twice, once during January 2009 and again in June 2010.

B.1.1 The CLASS Tandetron accelerator

The CLASS (Cambridge Laboratory for Accelerator Studies of Surfaces) Tandetron Accelerator is a tandem accelerator used primarily to study deposits on C-Mod surface materials [100]. An ion source produces negative ions that are accelerated in the first stage. These ions pass through a nitrogen gas stripping chamber in which positive

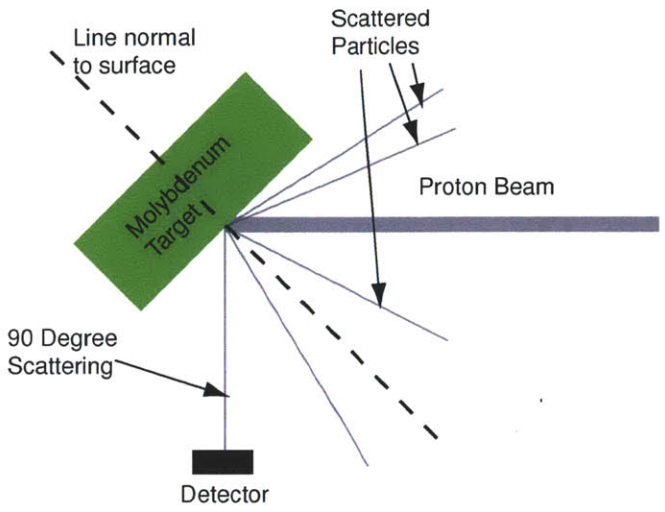

Figure B-1: Cartoon of the backscatter calibration

ions are produced. The positive ions are then accelerated through the second stage. By converting the negative ions to positive ions the accelerator can produce a beam with energy twice as high as it could with just accelerating ions of a single charge state. The experimental setup for the calibration is shown in Figure B-2.

B.1.2 Scattering from a heavy target

In a collision between a proton and a heavy nucleus in energies 2 MeV or below, the dominant force is the electro-magnetic force. Therefore, we can ignore any effects from nuclear excitation and use a simple classical approach to calculate the rebound energy of an incident ion off a stationary nucleus. Using conservation of energy and momentum we get the following three equations.

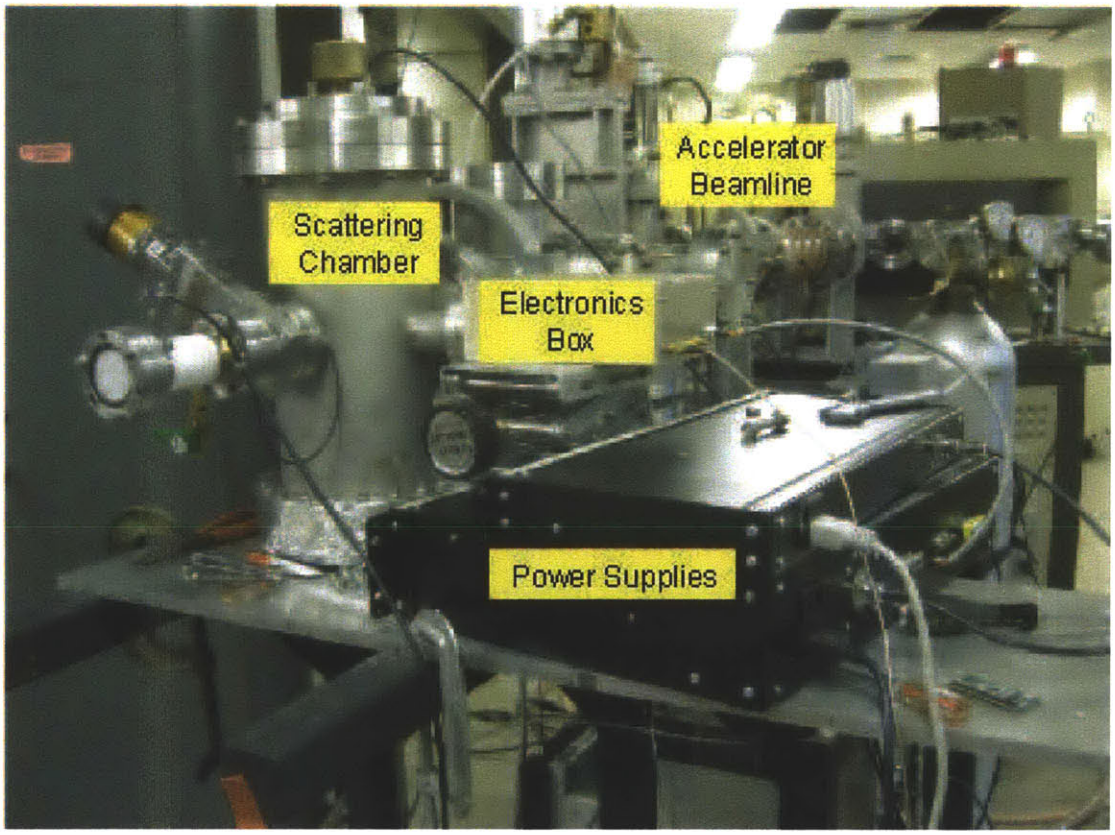

Figure B-2: A picture of the CLASS Tandetron accelerator and the CNPA diagnostic in the January 2009 calibration setup. This setup was recreated as closely as possible for the June 2010 calibration

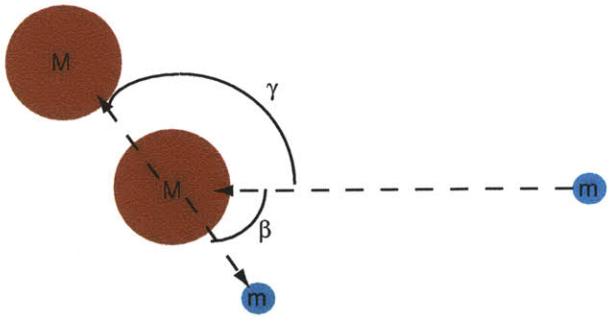

Figure B-3: Cartoon of the scattering process off of a heavy ion

$$\frac{1}{2}mv_i^2 = \frac{1}{2}mv_s^2 + \frac{1}{2}Mv_M^2 \tag{B.1}$$

$$mv_i = mv_s cos(\beta) + Mv_M cos(\gamma) \tag{B.2}$$

$$0 = mv_s sin(\beta) + Mv_M sin(\gamma) \tag{B.3}$$

where m denotes the mass of the incident ion, M denotes the mass of the target ion, v_i is the incident velocity, v_s is the scattering velocity, and v_M is the recoil velocity of the target nucleus. The angles β and γ represent the scattering angles for m and M respectively. A diagram of the process is shown in Figure B-3.

After some algebra we produce the following equation for the scattering velocity as a function of the incident velocity.

$$v_s = \frac{v_i}{\alpha + 1}\left(\alpha cos(\beta) \pm \sqrt{1 - \alpha^2 sin^2(\beta)}\right) \tag{B.4}$$

where:

$$\alpha = \frac{m}{M}$$

If we consider the case, as in the calibration setup, where the scattering angle β is 90 degrees, we can reduce Eq. B.4 to the following:

$$v_s = v_i \frac{\sqrt{1-\alpha^2}}{1+\alpha} \tag{B.5}$$

or using $W = \frac{1}{2}mv^2$ we get the following:

$$W_s = W_b \frac{1-\alpha}{1+\alpha} \tag{B.6}$$

Using Molybdenum as the target we see that:

$$v_s \approx 0.98 v_b \tag{B.7}$$

In a thick foil target, Eq. B.7 is satisfied for protons that scatter off of nuclei on the surface of the target. Protons that penetrate some distance into the target before scattering have a lower energy corresponding to how deep they penetrate. The resulting curve is one where a relatively constant fluence is seen at the detector until W_s is reached, at which point there is a sharp edge (see Figure B-4a).Counts that are observed above W_s can be attributed to double counting events, where two scattered protons arrive at the detector at the same time. When fluence is high, these double count rates are more common.

B.1.3 Energy spectra

Three spectra from different calibration runs along with a simulated spectra are shown in Figure B-4. All the actual spectra show clear edge features at W_s, similar to the simulation. However, the calibration spectra also show some double events that produce counts more energetic than W_s. These counts occur when two protons arrive at the detector at the same time. Raising beam fluence increases these double-counting events. In all cases, the double counting events were significantly lower than the single counts and are not expected to affect the calculation of where the edge is located.

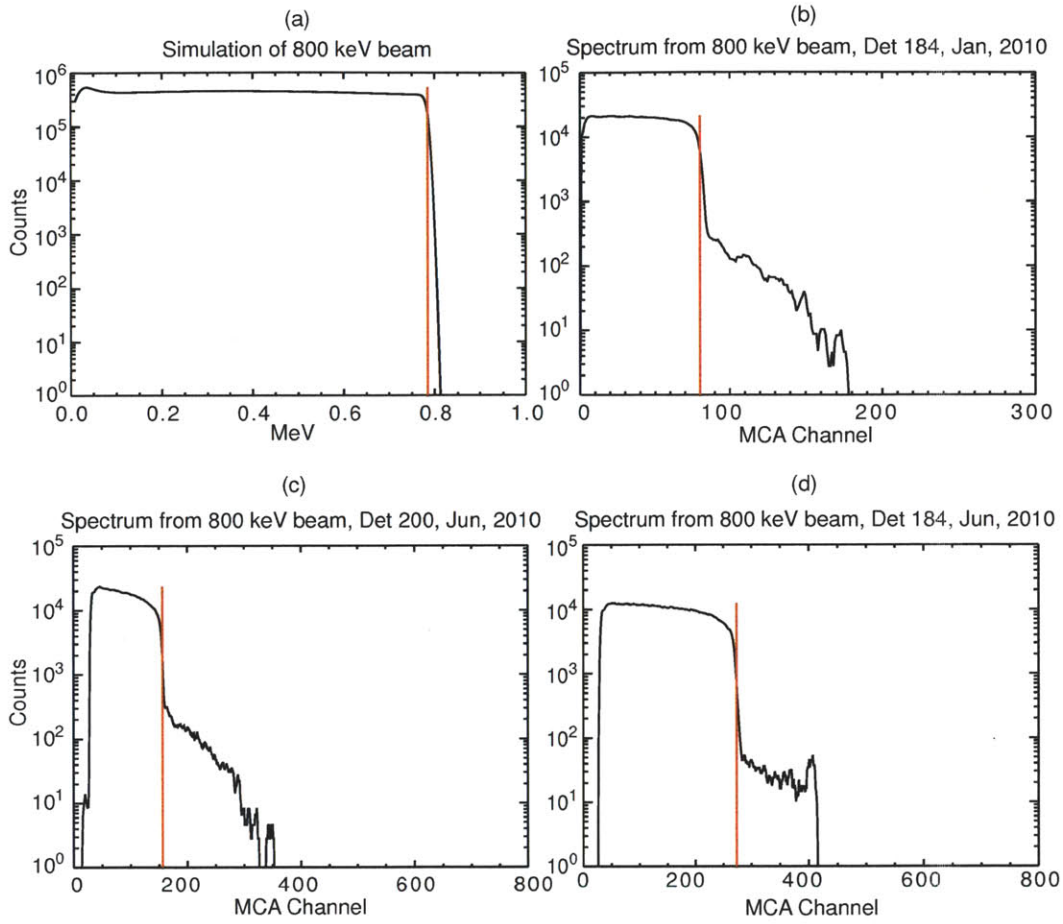

Figure B-4: This plot shows various energy spectra from backscattering calibrations. Plot (a) shows a simulation made by the SIMNRA program of 800 keV protons scattering off a thick molybdenum target at 90 degrees. The sharp edge is clearly seen. The red line shows the calculated value of W_s. Plot (b) shows the spectra for 800 keV protons for Detector 184 (unused during the campaign) The red line is where the W_s is taken from. Plots (c) and (d) show spectra of 800 keV ions for detectors 200 and 184, respectively.

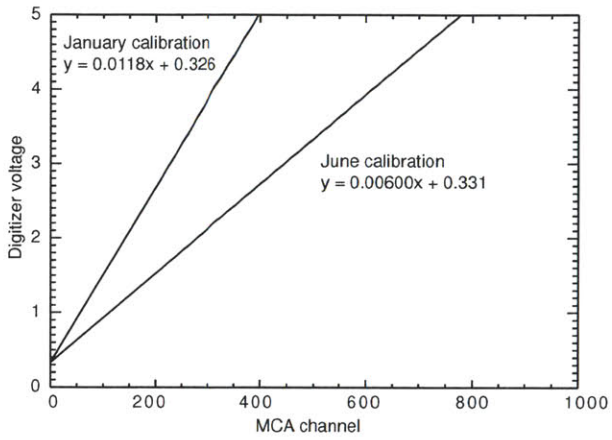

Figure B-5: Conversion between MCA Channel and digitizer voltage for both the January and June calibrations. The different curves occur because of a different resolution setting on the MCA.

Converting MCA channel to digitizer voltage

A second calibration was performed to determine the curve between the MCA channel and the digitizer in the C-Mod cell. A function generator was connected to the input of the shaper, and leading edges with heights of 2-40 mV were used as inputs to the shaper. The output of the shaper was connected to both the accelerator MCA and the CPCI digitizer. Using this, a relation was obtained between a channel on the MCA and the CPCI digitizer. The conversions used are shown below in Figure B-5. There are two curves shown in Figure B-5 because the MCA had a different resolution for each calibration.

B.1.4 Calibration results

The calibration results with fits are shown for 3 J-Top detectors in Figures B-7 and B-6. Figure B-7 shows a close up view of the calibration curves to highlight the discrepancy between the two calibrations. Figure B-6 shows the extrapolation of the curve to low and high energies. The results show a difference between the calibration

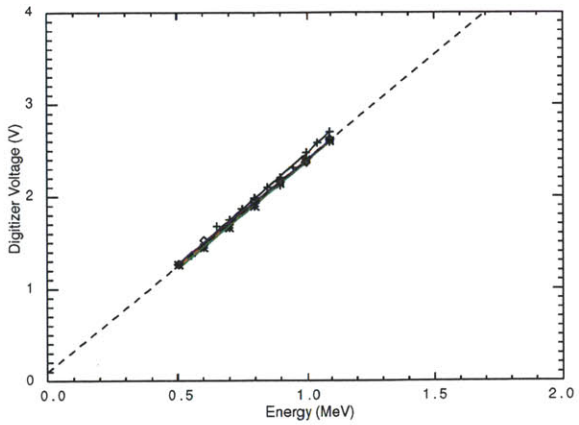

Figure B-6: Calibration curve for the J-Top CNPA detectors showing the linear curves for digitizer voltage as a function of incoming fast particle energy for 4 different calibrations and an extrapolation to high and low energies. The black curve is a fit to the January calibration of detector 184 (pluses). The red, blue and green curves are fits to detectors 184 (pluses) 197 (diamonds) and 200 (asterisks) respectively

results for the same detector over a 6 month range. This detector was not used in the tokamak, so the differences are not attributable to degradation due to particle fluence in C-Mod. Using the difference as an error estimate shows that we can determine the energy of the fast-ions to around 10% accuracy. However, the data show that the three detectors calibrated simultaneously on one day are in excellent agreement, indicating that there was no degradation of the detectors due to exposure to the plasma.

The difference between the January and June calibrations give the estimate for the calibration error. In the calculations in this thesis, the June calibration is used and the uncertainty is estimated based on the January error.

B.2 Spatial Calibration

In addition to an Energy calibration, a spatial calibration was performed to verify the geometrical views of the CNPAs.

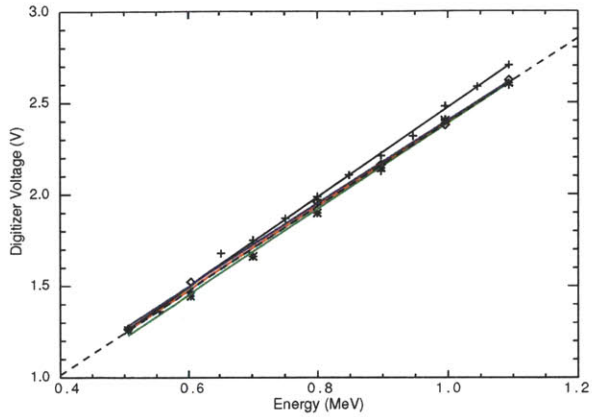

Figure B-7: Calibration curve for the J-Top CNPA detectors showing the linear curves for digitizer voltage as a function of incoming fast particle energy for 4 different calibrations zoomed in to show the divergence of the January calibration to the June calibrations. The black curve is a fit to the January calibration of detector 184 (pluses). The red, blue and green curves are fits to detectors 184 (pluses) 197 (diamonds) and 200 (asterisks) respectively

B.2.1 F-Top spatial calibration

The spatial calibration of F-Top was performed on two separate occasions. The first calibration was performed during spring of 2009, and the second calibration was performed during the summer of 2010. The calibrations were accomplished by replacing the detector with a visible camera with an appropriate sized mask, and viewing through the aperture. An LED was placed at known spatial locations in the tokamak and the results of these spatial calibrations were shown in Figure 2-8.

B.2.2 J-Top spatial calibration

The J-Top detectors were calibrated in a different manner than the F-Top detectors. Because of the physical layout of the detectors it was infeasible to replace them with a camera. However, we were able to replace them with a detector, not covered with a foil, and thus sensitive to visible light.

A small laser was mounted in the vessel at known spatial locations and projected

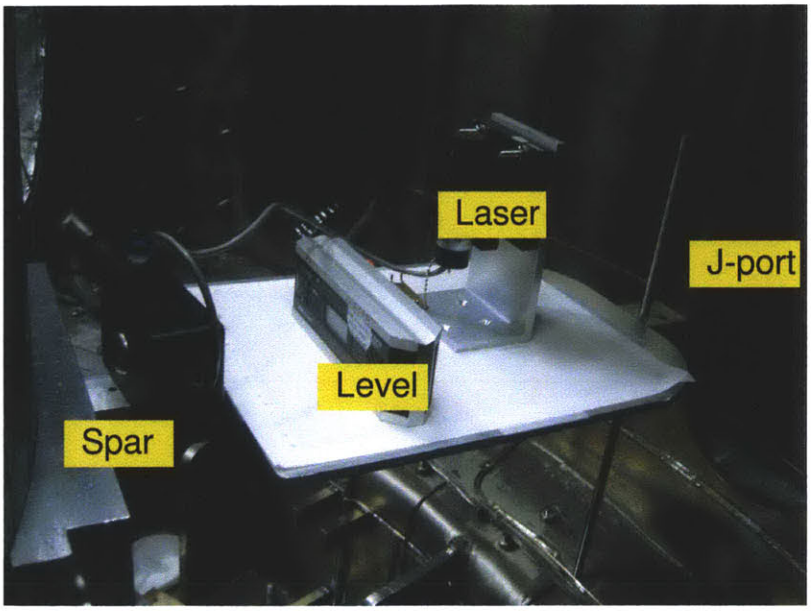

Figure B-8: Setup for the in-vessel spatial calibration for the J-Top CNPA.

vertically upwards through the apertures onto the detectors. A laser was chosen because diffuse light sources such as LEDs were found to be too weak to be seen by the detectors. The laser position was adjusted my translating it radially and toroidally, but not adjusting the tilt. The point of maximum signal on the detector indicates the location of the aperture relative to the vacuum vessel. A picture of the in-vessel calibration is shown in Figure B-8. Also, see the schematic diagram in Figure 2-3.

Mounting the laser required several in vessel components. A spar was secured to the inner wall by a metal strap that goes around the inner column. We secured a flat plate on top of the spar with a measured grid on top of it. Therefore, we were able to locate where in the vessel our laser was mounted. The difficulty in the calibration rested in ensuring that the spar was perfectly level and that the laser was pointed directly upwards. We were able to verify each of these within 0.05 degrees, which was the estimated sensitivity of our level. This corresponds to an error of approximately

3-4 mm for the aperture location. The position of the detector relative to the aperture is tightly constrained by the diagnostic design, and is known within 1-2 mm.

Appendix C

Charge-Exchange Cross-Sections for Proton-B^{4+} and Proton-C^{5+} Interactions

This appendix deals with the estimation of the cross-section for the following interaction,

$$H^{+} + B^{4+} \rightarrow H^{0} + B^{5+}. \tag{C.1}$$

Charge-exchange cross-sections for the interaction of fast protons and hydrogen-like boron interactions require theoretical calculations because of the difficulty of producing experimental data. The difficulty arises because an experimental measurement would require the near impossible task of injecting an energetic proton beam into a near-fully stripped boron population. For this thesis, the energy range of interest is between 100 keV and 2 MeV. The peak cross-section occurs when the proton energy is at a comparable speed to the bound electron Bohr velocity. For boron, the proton velocity is equal to the electron velocity at $\sim$ 600 keV, although it is found that the peak cross-section occurs at a slightly lower energy ($\sim$ 400 keV)

A 1982 paper by Macek and Alston [101] calculates the cross-section for interaction of light ions and hydrogen-like heavy ions by expanding in Z_p/Z_T and $Z_p e^2/(4\pi\epsilon_0\hbar v_p)$. The first expansion parameter is the ratio between the atomic number of the projectile nucleus and the target nucleus. In our case, the value is 1/5. The second parameter is the ratio between the particle velocity and the Bohr velocity of the projectile nucleus. For protons, the bound state energy is 13.6 eV, so the expansion is valid for energies above $13.6 m_p/m_e \approx 25$ keV.

Macek and Alston calculated the cross-sections using the strong potential Born (SPB) approximation. Their results for charge-exchange into the n^{th} orbital for a target with atomic number Z_T are reproduced below in SI units.

$$\begin{aligned}\sigma^n_{SPB} = &\left(\frac{4\pi\epsilon_0\hbar^2}{m_e e^2}\right)^2 \frac{Z_p^5}{Z_T^7} |M_n(v)|^2 \frac{1}{n^3} \times \\ &\times 2^8 \pi v^{12} |N(v)|^2 \int_{x_m}^{\infty} dx \left[\frac{1+v^2}{x^6} + \frac{1}{(x-x_0)^2+4v^2}\left(\frac{1+v^2}{x^4} + \frac{2x_0(x-x_0)-8v^2}{x^5}\right)\right] \times \\ &\times \exp\left[-2v\tan^{-1}\left|\frac{2v}{x-x_0}\right|\right] \end{aligned} \tag{C.2}$$

Where Z_p is the atomic number of the fast moving, electron-receiving ion. Z_T is the atomic number of the slow-moving electron-donor ion, n is the final quantum state of the donor ion. The following definitions are also used:

$$\begin{aligned} v &= \frac{Z_T e^2}{(4\pi\epsilon_0\hbar v_p)}) \\ x_0 &= 1 - v^2 \\ x_m &= \tfrac{1}{4}(1+v^2)^2 \\ |N(v)|^2 &= e^{\pi v} |\Gamma(1+iv)|^2 \\ |M_n(v)|^2 &= \frac{2n^2}{(1+\exp(-2\pi v))(n^2+v^2)} \end{aligned}$$

Here v represents the proton velocity normalized to the ground state Bohr velocity of the target nucleus. The equation is valid in both the low v and high v limits, provided that the proton energy remains above 25 keV.

There are two errata in Eq C.2 as it appears in Macek and Alston. The absolute value term in the arctangent needs to be included. Without taking the absolute value, the argument of the exponential switches sign at $x = x_0$. This causes an unphysical rapid increase in the cross-section at a specific energy value. Furthermore the $(1+v^2)/x^4$ term is mistakenly written as $(1+v^3)/x^4$. This error was found when comparing to a previous calculation done by Briggs [102].

The plots of Eq. C.2 (solid line) against the tabulated values (black pluses) given by Macek and Alston is shown in Figure C-1. Unfortunately, there are appear to be some small discrepancies between the tabulated values and the values derived from Eq. C.2.

In 1987 T.G. Winter improved the calculation for the p, B^{4+} electron transfer cross-section by employing a coupled-Sturmian-pseudostate basis [103, 104]. Winter's results along with the SPB results are shown in Figure C-1. Winter's results produced lower cross-sections than the SPB approach. He attributed the discrepancy partly to his more accurate treatment of transfer into excited states.

Unfortunately, Winter did not produce any calculations for electron transfer for proton energies above 600 keV, leaving only the SPB model as the best theoretical calculation at these energy levels [105]. It is unclear from these data alone whether the results from Winter's calculation asymptote to the SPB curve or remain lower than it. However, in 2004, Winter produced a calculation for electron transfer with hydrogen-like carbon at high energies [62],

$$H^+ + C^{5+} \rightarrow H^0 + C^{6+} \tag{C.3}$$

These results, coupled with the results from the 1987 paper produce a consistent picture of the charge-exchange cross-section with carbon up to 3 MeV. These results

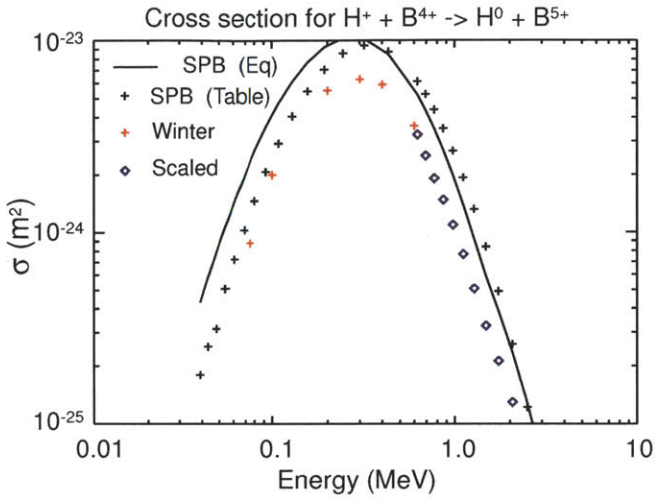

Figure C-1: Cross-sections for $H^+ + B^{4+} \rightarrow H^0 + B^{5+}$ interactions. Solid black line is from Eq C.2. Black pluses are from tabulated values in Macek and Alston [101]. Red pluses are from Winter [103]. Blue diamonds are scaled values of Eq C.2. Red pluses combined with blue diamonds are the recommended cross-section.

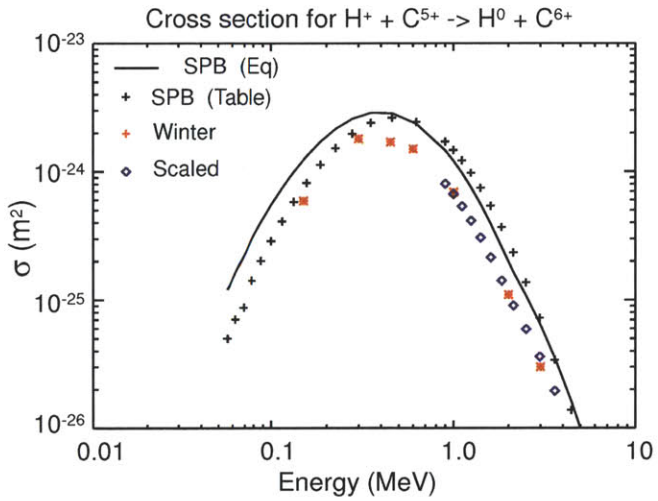

Figure C-2: Cross-sections for $H^+ + B^{4+} \rightarrow H^0 + B^{5+}$ interactions. Solid black line is from Eq C.2. Black pluses are from tabulated values in Macek and Alston [101]. Red pluses are from Winter [103, 62]. Blue diamonds are scaled values of Eq C.2. Red pluses combined with blue diamonds are the recommended cross-section.

are shown in Figure C-2 where it is seen that the constant factor discrepancy between Winter and the SPB approach persists into the high energy range. Therefore, to estimate the cross-section for the desired charge-exchange interaction with boron, we use Winter's results for energies less than 600 keV and scale the SPB approach by a constant factor (here 0.55) for energies greater than 600 keV. These scaled values are shown in blue diamonds in Figures C-1 and C-2. However, the first two energy points in the boron plot are scaled by 0.62 and 0.58 respectively for a smoother transition between Winter's calculations and the scaled SPB approach. It should be noted that these results represent the cross-section for charge-exchange into all possible n quantum states. The result for charge-exchange into the $n = 1$ quantum state is $\sim$0.8 of the total result.

The cross-sections are also given in tabulated form in Table C.1 for boron and carbon. The carbon results are not used in this thesis but may be important for other tokamak experiments where carbon is the dominant impurity. cross-sections have been included up to 10 MeV. Above this value, relativistic effects need to be included.

Table C.1: Cross-sections for charge-exchange with B^{4+} and C^{5+} cross-section results are in units of 10^{-26} (m^2) Starred entries are from Winter [103].

Energy (keV)	p-B^{4+}	p-C^{5+}
75	88*	–
100	200*	–
150	–	59*
200	550*	–
300	630*	180*
400	590*	–
450	–	170*
600	360*	150*
625	325	–
692	253	117
771	192	102
864	148	86.0
976	110	69.5
1110	76.9	53.7
1270	50.8	39.5
1480	32.5	26.7
1735	21.3	16.9
2060	13.0	9.9
2500	7.0	5.9
3080	3.2	3.3
3900	1.2	1.5
5100	0.35	0.51
6940	0.075	0.13
9990	0.010	0.02

Appendix D

List of Symbols used in this Thesis

Symbols	Units	Explanation
α	unitless	Reduced mass
β	radians	Scattering angle
γ	radians	Scattering angle
Δ_b	m	Banana width
ϵ_0	Farads/m	Permittivity of free space
θ	radians	Poloidal coordinate
ϑ	radians	Pitch angle
Λ	unitless	Coulomb logarithm
μ	Joule/Tesla	Adiabatic invariant
μ	unitless	Reduced mass
μ_0	Tesla m/Ampere	Permeability of free space
ν	s^{-1}	Collision frequency
ρ	unitless	Normalized tokamak radius (r/a)
ρ_L	m	Gyroradius
σ	m^2	Cross section
$\overleftrightarrow{\sigma}$	$ohms^{-1}$	conductivity tensor
τ_s	s^-	Classical slowing down time constant
ϕ	radians	Toroidal coordinate
χ_n	eV	Ionization energy from nth orbital
ψ	Tesla/m^2	Toroidal flux
ω	radians/s	Frequency (usu. of ICRF)
ω_c	radians/s	Cyclotron frequency
ω_p	radians/s	Plasma frequency

Symbols	Units	Explanation
a	m	Minor radius of a torus
$\vec{B}$	Tesla	Magnetic field
c	m/s	Speed of light
D	m^2/s	Diffusion
e	Coulomb	Elementary electric charge
$\vec{E}$	Volt/m	Electric field
f	m^{-3} $(m/s)^{-3}$	6D distribution function
f	Hz	Frequency (usu. of ICRF)
f_c	Hz	Cyclotron frequency
$\bar{g}_n$	unitless	Average gaunt factor
$\vec{F}$	Newtons	Force
I	Ampere	Current (electric or beam)
I_p	Ampere	Plasma current
$\vec{J}$	Ampere/m^2	Current density
k	m^{-1}	Wave number
$\overleftrightarrow{K}$	unitless	Dielectric tensor
L	m	Scale length
m	kg	Particle mass
M	kg	Heavy ion mass
n	m^{-3}	Density
n	unitless	Principal quantum orbital
N	unitless	Index of refraction
q	Coulombs	Signed atomic charge
q	unitless	Tokamak safety factor
r	m	Minor radius coordinate
R	m	Major radius coordinate
R_0	m	Major radius of a torus
t	s	Time
T	eV, keV, J	Temperature
T_e	keV	Electron temperature
T_{eff}	eV or keV	Effective temperature
u	m/s	Velocity
$\vec{v}$	m/s	Velocity
$v_\perp$	m/s	Velocity perpendicular to mag. field
$v_\parallel$	m/s	Velocity parallel to mag. field
$\vec{V}$	m/s	Convective diffusion
W	J, eV	Energy
z	m	Vertical distance from tokamak midplane
Z	unitless	Atomic charge
Z_{eff}	unitless	Effective charge of plasma

Bibliography

[1] G. McCraken, P. S. *Fusion: the Energy of the Universe.* Elsevier (2005).

[2] Tang, V. *Experimental and numerical characterization of ion-cyclotron heated protons on the Alcator C-Mod tokamak.* Ph.D. thesis, MIT, Department of Nuclear Science and Engineering (2006).

[3] Ono, M., Kaye, S., et al. *Exploration of spherical torus physics in the NSTX device. Nuclear Fusion*, 40(3Y):557 (2000).

[4] Luxon, J. *A design retrospective of the DIII-D tokamak. Nuclear Fusion*, 42(5):614 (2002).

[5] Wesson, J. *Tokamaks.* Oxford University Press (2004).

[6] F. Najmabadi, L. B., A. Abdou. *The ARIES-AT advanced tokamak, advanced technology fusion power plant. Fusion Engineering and Design*, 80(1):3–23 (2006).

[7] Thommassen, K. I. *Progress and directions in magnetic fusion energy. Ann. Rev. Energy*, 9:281–319 (1984).

[8] Maisonnier, C. and Toschi, R. *Overview of the European fusion programme. Fusion Engineering and Design*, 8:3 – 7 (1989).

[9] Kishimoto, H., Ishida, S., et al. *Advanced tokamak research on JT-60. Nuclear Fusion*, 45(8):986 (2005).

[10] Gates, D., Ahn, J., et al. *Overview of results from the National Spherical Torus Experiment (NSTX). Nuclear Fusion*, 49(10) (2009).

[11] Zohm, H., Angioni, C., et al. *Overview of ASDEX Upgrade results. Nuclear Fusion*, 43(12):1570 (2003).

[12] Freidberg, J. *Ideal Magnetohydrodynamics.* Plenum Press (1987).

[13] Lao, L., John, H. S., et al. *Reconstruction of current profile parameters and plasma shapes in tokamaks. Nuclear Fusion*, 25(11):1611 (1985).

[14] Hutchinson, I., Boivin, R., et al. *First results from Alcator C-MOD. Phys. of Plasmas*, 1(5):1511 (1994).

[15] Bonoli, P., Parker, R., et al. *Wave-particle studies in the ion cyclotron and lower hybrid range of frequencies in Alcator C-Mod. Fus. Sci. and Tech.*, 51(3):401–436 (2007).

[16] Huba, J. *NRL plasma formulary* (2007).

[17] Trubnikov, B. A. *Particle interactions in a fully ionized plasma. Rev. of Plas. Phys.*, 1:105 (1965).

[18] Eriksson, L.-G., Hellsten, T., et al. *Comparison of time dependent simulations with experiments in ion cyclotron heated plasmas. Nuclear Fusion*, 33(7):1037 (1993).

[19] Kislyakov, A. and Petrov, M. P. *Neutral atom analyzers for diagnosing hot plasmas: A review of research at the Ioffe physicotechnical institute. Plasma Physics Reports*, 35:535–551 (2009).

[20] Roquemore, A. L. *Application of an $E\|B$ spectrometer to PLT charge-exchange diagnostics. Review of Scientific Instruments*, 56(5):1120–1122 (1985).

[21] Roquemore, A. L. and Medley, S. S. *Design concepts for compact mass/energy charge exchange analyzers. Review of Scientific Instruments*, 57(8):1797–1799 (1986).

[22] Kislyakov, A. I., Khudoleev, A. V., et al. *High energy neutral particle analyzer. Fusion Engineering and Design*, 34-35:107 – 113 (1997). Fusion Plasma Diagnostics.

[23] Wong, K. L., Schmidt, G. L., et al. *First evidence of collective alpha particle effect on toroidal Alfvén eigenmodes in the TFTR D-T experiment. Phys. Rev. Lett.*, 76(13):2286–2289 (1996).

[24] Darrow, D., Zweben, S., et al. *Observations of neutral beam and ICRF tail ion losses due to Alfvén modes in TFTR. Journal of Nuclear Fusion*, 37(7) (1997).

[25] Sears, J. *Measurement and interpretation of stable and unstable alfvén eigenmodes in the presence of fast ions in alcator c-mod.* PhD dissertation, MIT, Department of Electrical Engineering (2010).

[26] Lee, W., Boivin, R. L., et al. *Neutral particle analysis of ICRF heated discharges on Alcator C-Mod. Plasma Phys. and Controlled Fusion*, 45(7):1465–1475 (2003).

[27] Rost, J. C. *Fast ion tails during radio frequency heating on the Alcator C-Mod tokamak.* PhD dissertation, MIT, Department of Physics (1998).

[28] Krasilnikov, A. V., Medley, S. S., et al. *Tokamak fusion test reactor charge exchange atom spectrometry using a natural diamond detector. Review of Scientific Instruments*, 70(1):1107–1110 (1999).

[29] Murakami, S., Fukuyama, A., et al. *A global simulation study of icrf heating in the lhd. Nuclear Fusion*, 46(7):S425 (2006).

[30] Tang, V., Liptac, J., et al. *Compact multichannel neutral particle analyzer for measurement of energetic charge-exchanged neutrals in Alcator C-Mod. Rev. of Sci. Inst*, 77(8) (2006).

[31] Luo, Y., Heidbrink, W., et al. *Measurement of the D_α spectrum produced by fast ions in DIII-D. Review of Scientific Instruments*, 78(3) (2007).

[32] K.T. Liao, I. O. B., W. L. Rowan. *Minority ion measurements during icrf experiments in alcator c-mod.* Number 19 in RF Power in Plasmas. Newport, RI (2011).

[33] Heidbrink, W. and Strachan, J. *Tokamak ion temperature and poloidal field diagnostics using 3-MeV protons. Review of Scientific Instruments*, 56(4):501–518 (1985).

[34] Garcia-Muñoz, M., Fahrbach, H., et al. *Scintillator based detector for fast-ion losses induced by magnetohydrodynamic instabilities in the ASDEX upgrade tokamak. Review of Scientific Instruments*, 80(5) (2009).

[35] Darrow, D. S. *Scintillator based energetic ion loss diagnostic for the National Spherical Torus Experiment. Review of Scientific Instruments*, 79(2):023502 (2008).

[36] Darrow, D., Baeumel, S., et al. *Initial results from the lost alpha diagnostics on Joint European Torus. Review of Scientific Instruments*, 77(10):10E701 (2006).

[37] Cecil, F. E., Aakhus-Witt, A., et al. *Thin foil Faraday collectors as a radiation hard fast lost-ion diagnostic. Review of Scientific Instruments*, 74(3):1747–1749 (2003).

[38] Kiptily, V., Adams, J., et al. *Gamma-ray imaging of d and 4 he ions accelerated by ion-cyclotron-resonance heating in jet plasmas. Nuclear Fusion*, 45(5):L21 (2005).

[39] Gates, D. A., Gorelenkov, N. N., et al. *Ion heating by fast-particle-induced Alfvén turbulence. Phys. Rev. Lett.*, 87(20):205003 (2001).

[40] Medley, S. and Roquemore, A. *Neutral particle analyzer diagnostic on the National Spherical Torus Experiment. Review of Scientific Instruments*, 75(10):3625–3627 (2004).

[41] Medley, S. and Roquemore, A. *Construction and operation of parallel electric and magnetic field spectrometers for mass/energy resolved multi-ion charge exchange diagnostics on the Tokamak Fusion Test Reactor. Review of Scientific Instruments*, 69(7):2651–2662 (1998).

[42] Shinohara, K., Darrow, D., et al. *Solid state neutral particle analyzer array on National Spherical Torus Experiment. Review of Scientific Instruments*, 75(10):3640–3642 (2004).

[43] Carolipio, E. M. and Heidbrink, W. W. *Array of neutral particle analyzers at diii-d. Review of Scientific Instruments*, 68(1):304 –307 (1997).

[44] Korotkov, A., Gondhalekar, A., et al. *Impurity induced neutralization of mega-electronvolt energy protons in jet plasmas. Nuclear Fusion*, 37(1):35–51 (1997).

[45] Hellsten, T. Personal communication. (2011).

[46] Liptac, J. *Lower hybrid modeling and experiments on Alcator C-Mod.* Ph.D. thesis, MIT, Department of Nuclear Science and Engineering (2006).

[47] Basse, N., Dominguez, A., et al. *Diagnostic systems on Alcator C-Mod. Fusion Science and Technology*, 51(3):476–507 (2007).

[48] Irby, J., Marmar, E., et al. *Two-color interferometer system for Alcator C-Mod. Review of Scientific Instruments*, 59(8):1568–1570 (1988).

[49] Irby, J., Murray, R., et al. *A two-color interferometer using a frequency doubled diode pumped laser for electron density measurements. Review of Scientific Instruments*, 70(1):699–702 (1999).

[50] Hughes, J., Mossessian, D., et al. *High resolution edge Thomson scattering measurements on the Alcator C-Mod tokamak. Review of Scientific Instruments*, 72(1):1107–1110 (2001).

[51] Nelson-Melby, E., Porkolab, M., et al. *Experimental observations of mode-converted ion cyclotron waves in a tokamak plasma by phase contrast imaging. Phys. Rev. Lett.*, 90(15):155004 (2003).

[52] R. M. Mcdermott, J. H., B. Lipschultz. *Edge radial electric field structure nad its connections to H-mode confinement in Alcator C-Mod plasmas. Phys. of Plas.*, 16(056103) (2009).

[53] Rowan, W. L., Bespamyatnov, I. O., et al. *Light impurity transport at an internal transport barrier in alcator c-mod. Nuclear Fusion*, 48(10):105005 (2008).

[54] Granetz, R. S., Hutchinson, I., et al. *Magnetic diagnostics in Alcator C-MOD. Rev. Sci. Instrum.*, 61:2967–2969 (1990).

[55] Stix, T. *Fast-wave heating of a two-component plasma. Nuclear Fusion*, 15:737–754 (1975).

[56] Kiptily, V., von Thun, C. P., et al. *Recent progress in fast ion studies on jet. Nuclear Fusion*, 49(6):065030 (2009).

[57] Wagner, F. *A quarter-century of H-mode studies. Plasma Physics and Controlled Fusion*, 49:1–+ (2007).

[58] Whyte, D., Hubbard, A., et al. *I-mode: an h-mode energy confinement regime with l-mode particle transport in alcator c-mod. Nuclear Fusion*, 50(10):105005 (2010).

[59] Fite, W. L., Brackmann, R. T., et al. *Charge exchange in proton-hydrogen-atom collisions. Phys. Rev.*, 112(4):1161–1169 (1958).

[60] R.K Janev, J. S. *Atomic and plasma-material interaction data for fusion. Suppl. to Nuc. Fus.*, 4(1) (1993).

[61] Hutchinson, I. *Principles of Plasma Diagnostics, 2nd ed.* Cambridge Univ. Press (2002).

[62] Winter, T. G. *Ionization, excitation, and electron transfer in MeV-energy collisions between light nuclei and* $C^{5+}(1s)$ *ions studied with a Sturmian basis. Phys. Rev. A*, 69(4):042711 (2004).

[63] ADAS. online database (2010).

[64] Tamor, S. *Antic: A code for calculation of neutral transport in cylindrical plasmas. Journal of Computational Physics*, 40(1):104 – 119 (1981).

[65] Hughes, J. W., LaBombard, B., et al. *Advances in measurement and modeling of the high-confinement-mode pedestal on the alcator c-mod tokamak.* 13(5):056103 (2006).

[66] R.K Janev, D. P., C.D. Boley. *Penetration of energetic neutral beams into fusion plasmas. Nuc. Fus.*, 29(12) (1989).

[67] Hammett, G. *Fast ion studies of ion cyclotron heating in the PLT tokamak.* PhD dissertation, Princeton, Department of Astrophysical Science (1986).

[68] Kurz, C. and Fiore, C. L. *Neutral particle diagnostics for alcator C-Mod. Review of Scientific Instruments*, 61(10):3119 –3121 (1990).

[69] Snipes, J. A., Basse, N., et al. *Active and fast particle driven alfvén eigenmodes in alcator c-mod. Physics of Plasmas*, 12(5):056102 (2005).

[70] Brambilla, M. *Electron landau damping of ion bernstein waves in tokamak plasmas. Nuclear Fusion*, 38(12):1805 (1998).

[71] Lin, Y., Rice, J. E., et al. *Observation of ion-cyclotron-frequency mode-conversion flow drive in tokamak plasmas. Phys. Rev. Lett.*, 101:235002 (2008).

[72] Bonoli, P. T., Brambilla, M., et al. *Mode conversion electron heating in Alcator C-Mod: Theory and experiment. Physics of Plasmas*, 7(5):1886–1893 (2000).

[73] P.T. Bonoli, C. F., M. Brambilla. *Numerical modelling of icrf physics experiments in the alcator c-mod tokamak.* Number 18 in IAEA Fusion Energy Conference. Sorrento, Italy (2000).

[74] Villard, L., Appert, K., et al. *Global waves in cold plasmas. Computer Physics reports*, 4(3-4):95 – 135 (1986).

[75] Eriksson, L.-G., Hellsten, T., et al. *Calculations of power deposition and velocity distributions during icrh: Comparison with experimental results. Nuclear Fusion*, 29(1):87 (1989).

[76] J. Carlsson, T. H., L.-G. Eriksson. *Numerical modelling of icrf physics experiments in the alcator c-mod tokamak.* Number 18 in IAEA Fusion Energy Conference. Sorrento, Italy (2000).

[77] Hedin, J., Hellsten, T., et al. *Self-consistent calculations of parasitic ion absorption during fast wave electron current drive.*

[78] E.F. Jaeger, S. A., L.A. Berry. *Self-consistent full-wave and Fokker-Planck calculations for ion cyclotron heating in non-Maxwellian plasmas. Phys of Plas.*, 13(056101) (2006).

[79] Murakami, T. Personal Communication (2011).

[80] Choi, M., Chan, V. S., et al. *Monte carlo orbit/full wave simulation of ion cyclotron resonance frequency wave damping on resonant ions in tokamaks. Physics of Plasmas*, 12(7):072505 (2005).

[81] D.L. Green, L. B., E.F. Jaeger. *Reconstruction in 3d of the fast wave fields in iter, diii-d, c-mod and nstx, including the coupling of full-wave and particle codes to resolve finite orbit effects.* Number 18 in RF Power in Plasmas. Gent, Belgium (2009).

[82] Choi, M., Green, D., et al. *Iterated finite-orbit monte carlo simulations with full-wave fields for modeling tokamak ion cyclotron resonance frequency wave heating experiments. Physics of Plasmas*, 17(5):056102 (2010).

[83] Geisel, T. *One Fish Two Fish Red Fish Blue Fish.* Random House (1960).

[84] Kerbel, G. D. and McCoy, M. G. *Kinetic theory and simulation of multispecies plasmas in tokamaks excited with electromagnetic waves in the ion-cyclotron range of frequencies. Phys. of Fluids*, 28(12):3629–3653 (1985).

[85] R.W. Harvey, M. M. *The CQL3D Fokker-Planck code* (1992). Paper presented at IAEA Tech. Comm. Mtg. on Advances in Simulation and Modeling of Thermonuclear Plasmas, Montreal.

[86] C.F. Kennel, F. E. *Velocity space diffusion from weak plasma turbulence in a magnetic field. Phys. of Fluids*, 9(12) (1966).

[87] Lerche, I. *Quasilinear theory of resonant diffusion in a magneto-active, relativistic plasma. Phys. of Fluids*, 11(8) (1968).

[88] E.F. Jaeger, E. D., L.A. Berry. *Advances in full-wave modeling of radio frequency heated, multidimensional plasmas. Phys. of Plas.*, 9(1873) (2002).

[89] Jaeger, E., Harvey, R., et al. *Global-wave solutions with self-consistent velocity distributions in ion cyclotron heated plasmas. Nuclear Fusion*, 46(7):S397 (2006).

[90] Schmidt, A. *Measurements and modeling of lower-hybrid driven fast electrons on alcator C-Mod.* PhD dissertation, MIT, Department of Physics (2011).

[91] Tsujii, N., Porkolab, M., et al. *ICRF mode conversion studies with phase contrast imaging and comparisons to full-wave simulations.* Number 19 in RF Power in Plasmas. Newport, RI, USA (2011).

[92] Wright, J., Bader, A., et al. *Time dependent evolution of RF-generated non-thermal particle distributions in fusion plasmas. to appear in Journal of Physics Conference Series* (2011).

[93] Angioni, C. and Peeters, A. G. *Gyrokinetic calculations of diffusive and convective transport of alpha particles with a slowing-down distribution function. Physics of Plasmas*, 15(5):052307 (2008).

[94] Batchelor, D. Personal communication. (2006).

[95] Harvey, R., Petrov, Y., et al. *Validation studies of quasilinear theory or resonant diffusion in the ion cyclotron range of frequencies by comparison with exact integration results.* Number 19 in RF Power in Plasmas. Newport, RI (2011).

[96] Harvey, R., Petrov, Y., et al. *First order finie-orbit-width corrections in CQL3D ion Fokker-Planck modeling of the NSTX HHFW experiment.* Number 38 in European Physical Conference. Strasbourg, France (2011).

[97] Elwasif, W. R., Bernholdt, D. E., et al. *Component framework for coupled integrated fusion plasma simulation.* In *Proceedings of the 2007 symposium on Component and framework technology in high-performance and scientific computing*, CompFrame '07, pages 93–100. ACM, New York, NY, USA (2007).

[98] Perkins, F. W. *Icrf heating theory. Plasma Science, IEEE Transactions on*, 12(2):53 –63 (1984).

[99] Parisot, A. *Mode conversion current drive experiments on Alcator C-Mod.* PhD dissertation, MIT, Department of Electrical Engineering (2007).

[100] Barnard, H. *External proton beam analysis of plasma facing materials for magnetic confinement fusion applications.* Master's project, Massachusetts Institute of Technology, Department of Nuclear Science and Engineering (2009).

[101] Macek, J. and Alston, S. *Theory of electron capture from a hydrogenlike ion by a bare ion. Phys. Rev. A*, 26(1):250–270 (1982).

[102] Briggs, J. S. *Impact-parameter formulation of the impulse approximation for charge exchange. Journal of Physics B: Atomic and Molecular Physics*, 10(15):3075 (1977).

[103] Winter, T. G. *Electron transfer and ionization in collisions between protons and the ions He+, Li2+, Be3+, B4+, and C5+ studied with the use of a Sturmian basis. Phys. Rev. A*, 35(9):3799–3809 (1987).

[104] Winter, T. G. *Electron transfer and ionization in collisions between protons and the ions Li^{2+} and He^{+} studied with the use of a Sturmian basis. Phys. Rev. A*, 33(6):3842–3852 (1986).

[105] Winter, T. G. Personal Communication (2010).